Engineered Biological Construction Material: Self-healing Concrete and Self-healing Carbon Negative Enzymatic Construction Materials (ECM)

by

Shuai Wang

A Dissertation
Submitted to the Faculty
of the
WORCESTER POLYTECHNIC INSTITUTE
in partial fulfillment of the requirements for the
Degree of Doctor of Philosophy
in
Civil and Environmental Engineering

_____

April 2023

APPROVED:

_____

Prof. Nima Rahbar, Major Advisor, CE Department, WPI

_____

Prof. Suzanne Frances Scarlata, Committee Member, CBC Department, WPI

_____

Prof. Carrick McAfee Eggleston, Committee Member, CE Department Head, WPI

_____

Prof. Winston Oluwole Soboyejo, Committee Member, Interim President, WPI

Engineered Biological Construction Material: Self-healing Concrete and Self-healing Carbon Negative Enzymatic Construction Materials (ECM)

Shuai Wang

A Dissertation
Submitted to the Faculty
of the
WORCESTER POLYTECHNIC INSTITUTE
in partial fulfillment of the requirements for the
Degree of Doctor of Philosophy
in
Civil and Environmental Engineering

April 2023

APPROVED:

_____
Professor Nima Rahbar
Major Advisor
Worcester Polytechnic Institute

_____
Professor Suzanne Frances Scarlata
Committee Member
Worcester Polytechnic Institute

_____
Professor Carrick Eggleston
Committee Member
Worcester Polytechnic Institute

_____
Professor Winston Oluwole Soboyejo
Committee Member
Worcester Polytechnic Institute

Vita

Shuai Wang was born in Zhuhai, China. He attended the University of Nebraska Lincoln, where he obtained a B.Sc. in Construction Engineering in 2018. He then moved to Worcester in 2019 to attend the Ph.D. program in Civil, Environmental, & Architectural Engineering at Worcester Polytechnic Institute. He joined the Bioinspired Material Design Lab (BMDL) under the supervision of Prof. Nima Rahbar in 2019. Since then, he has been doing multi-disciplinary research at the boundary of mechanics, materials, and simulation. This dissertation contains his research during these five years at Worcester Polytechnic Institute. While at Worcester Polytechnic Institute, he was also a teaching assistant for several courses (architectural design, design of reinforced concrete structures, fundamental of civil engineering AutoCAD, Introduction to analysis and design, materials of construction, principles of HVAC design for buildings, structural engineering, environmental impacts of engineering decisions) and was a research assistant. He also holds two patents on construction materials during his Ph.D. study.

Acknowledgements

Recalling my PhD at WPI for the past five years have been the most rewarding and intellectually challenging experience in my life. This dissertation would not be possible without the support of advisors, colleagues, collaborators, friends and family. Hence, I would love to use the next few pages to acknowledge those who have directly or indirectly helped make my journey at WPI smoother and more enjoyable.

First, I would like to express my deep gratitude to my advisors, Prof. Nima Rahbar who has been incredibly helpful, supportive and encouraging throughout my PhD. He disciplines himself with high standards and show me all the excellent qualities a researcher should have. He will be a role model I am following in my careers. I can't never be thankful enough to Nima for the academic freedom, flexibility and trust he has given me over the years in pursuing my thesis research. He also being patient and tolerant with my mistakes. Working with Nima in the past five years has helped me grow and improve tremendously in many different aspects as a researcher, an educator, a colleague and a person. Thank you, Nima, I feel so fortunate to have you as my advisor, and you are the role model that I want to become in my future academic career.

Second, I would like to thank Prof. Suzanne Scarlata for co-advising me on our project regarding enzyme catalysis. She always very kind and generous in providing advice, resources and support whenever I faced problems. I am also deeply grateful to my Ph.D. committee members Prof Winston Soboyejo and Prof Carrick Eggleston for their advice, support and encouragement throughout the process. Prof Wole always broaden my horizons and enhance my

sensitivity to research direction. Prof Carrick always always inspires me to think about deeper and more detailed.

And I would also thank Prof. Rajib Mallick for co-advising me on our project regarding asphalt material. I also benefitted from the aid of a number of former and current graduate/undergraduate students: Dr. Jessica Anne Rosewitz, Dr Habibeh Ashouri Choshali, Dr Ram Kumar Veeraragavan, Noah, Pins, Clara Dublin...

I would also love to thank my lab manager Mr. Russell G. Lang, Dr. Wenwen Yao, Mr. Donald Pellegrino for their help and support in and out of the workspace during my PhD.

I would also love to thank my undergraduate mentors/friends (Prof Jiashi Yang and Prof Li Tan) at University of Nebraska-Lincoln, who have given me enormous support during my time at Lincoln and helped consolidated my academic dream.

Finally, I must thank my parent and grandmom for their love and support during the past five years, which have certainly been the most challenging of my life. Always knowing you were available to talk and support me means a great deal. This dissertation is also dedicated to my late grandfather and grandparent (mother side), whom I love dearly. I believe you will be proud of me in heaven. May I move forward with my career with their love and enthusiasm and have an impact on the world large enough for us. None of this would be possible without your support, love and sacrifice.

ABSTRACT

Concrete, a contribution of calcium silicate hydrate mixture has been widely used as manufactured material in buildings, bridges, and airport runways, and is a significant contributor to anthropogenic carbon dioxide (CO_2) emissions. Concrete recycling could help, but the benefits of recycling are limited by challenges such as the energy consumption in the crushing and transport of recycled concrete, acid leaching harmful to the environment, and strength reduction. Humans never stop seeking a way to address the carbon footprint and sustainability of concrete. Although strategies such as point-source CO_2 capture, renewable fuels, alternative cement, and supplementary cementitious materials can yield substantial reductions in cement-related CO_2 emissions, emerging enzymatic technologies based on the mechanisms of enzymatic biomineralization have the potential to radically transform the concrete production emission issues and reach carbon neutralization. In this dissertation, inspired by the extremely efficient process of CO_2 transport in mammal cells, a self-activated healing mechanism for a cementitious matrix and an ultra-strong self-healing enzymatic construction material (ECM) are proposed using Carbonic Anhydrase (CA) enzyme. Results also show the autonomous self-healing of millimeter size cracks in enzyme modified concrete within 24 hours, and that the self-healed concrete regains strength after incubation.

The second part of this dissertation outlines a method of developing carbon negative self-healing enzymatic construction material (ECM). The carbonic anhydrase accelerated the mineralization on the polymer scaffold to form a mineral bridge, which firmly bridges sand particles together. The minerals on the scaffold are typically assembled into uniform clusters to efficiently serve as the stress concentration point and retard crack propagation. The mechanical experiment showed that the compressive strength is more than two times that of minimum

acceptable cement mortar and significantly higher than any currently available biological construction materials. Results also show that the specific strength of ECM is similar to lightweight concrete. In terms of self-healing, the ECM is capable self healing through at least six cycles of fracture while keeping 50% of its original strength. This self-healing process only consumes carbon dioxide without an additional source of energy.

Inspired by the use of laser therapy on tumor tissue, we then proposed an advanced ECM that was integrated with nanoparticles to achieve rapid on-site curing and self-healing. The new ECM called ECM-n, first completed curing building material through photothermal effect and overcame the complicated laboratory dehydration issue of ECM. The whole curing process was employed with a low power laser for a few hours and the crack was successfully healed with the same strength on the ECM-n compare to ECM.

We believe the features of ECM are the key for carbon negative emission, self-healing, and multifunctional construction materials in frontier applications such as temporary shelter bases, building secondary structures, pipe transport in extreme weather and even could be space bases construction under high concentrations of carbon dioxide planet-Mars.

Published Content

Chapter 3 has been adapted from: Jessica A. Rosewitz, Shuai Wang, Suzanne F. Scarlata, Nima Rahbar, An enzymatic self-healing cementitious material, Applied Materials Today, Volume 23, 2021, 101035, ISSN 2352-9407, https://doi.org/10.1016/j.apmt.2021.101035.

Chapter 4 has been adapted from: Shuai Wang, Suzanne F. Scarlata, Nima Rahbar, A self-healing enzymatic construction material, Matter, Volume 5, Issue 3, 2022, Pages 957-974, ISSN 2590-2385, https://doi.org/10.1016/j.matt.2021.12.020.

Chapter 5 has been adapted from: Shuai Wang, Suzanne Scarlata, Nima Rahbar, Curing and self-healing of enzymatic construction materials using nanoparticles, Cell Reports Physical Science, Volume 3, Issue 9, 2022, 101039, ISSN 2666-3864, https://doi.org/10.1016/j.xcrp.2022.101039.

Contents

List of Figures

List of Tables

1 INTRODUCTION

1.1 Thesis Goals

Buildings account for 40% of global energy consumption and 33% of greenhouse gas emissions [1] [2]. Concrete has been a major material in building for over two centuries due to its strength, durability, and versatility. However, the key ingredient in cement production for concrete is responsible for 8% of global carbon dioxide (CO_2) emissions [3]. According to industrial statistics, each kilogram of cement produced emits nearly 1 kg of CO_2 [4]. Multiple methods have been proposed reduce this carbon footprint, such as: developing alternative types of cement, incorporating recycled materials, and improving the durability of concrete. None of these proposed concepts keep the material strength nor achieve fundamentally zero or low carbon emission.

Carbon mineralization is a natural process whereby CO_2 transforms into a solid mineral and is sequestered in rocks. As specific rocks are weathered globally by carbonic acid resulting from the dissolution of atmospheric CO_2 in natural waters, calcium and bicarbonate are eventually transported to the oceans where they eventually precipitate as calcium carbonate (limestone), sequestering CO_2 from the atmosphere in limestone. The inclusion of calcium is essential in cement production, as the carbon mineralization process results in the creation of calcium salts, which are known to greatly diminish carbon dioxide emissions. Biomineralized Materials (BMs) constitute an important class of low-CO_2 composites synthesized by activating photosynthesis of cyanobacteria or nutrient solution precursors with calcium aqueous solutions [5] [6]. Numerous studies have shown that BMs exhibited engineering performance (e.g., self-healing, self-generate, self-replicate, and self-sustainability) comparable or even superior to synthetic polymers [7] [8] [9]. However, many questions remain about this important class of materials in

terms of the mechanical properties for their use in construction and utilization for carbon footprint in sustainable environments.

To address the above issues, we successfully developed an enzymatic self-healing concrete, which was designed for the capability of millimeter scale crack self-healing. Afterward, we developed a carbon negative emission concrete substitute material that combines carbon sequestration and multiple cycles of self healing with outstanding mechanical properties. This dissertation focuses on bringing clarity to (i) an enzymatic method to produce concrete with self healing ability, (ii) the development of concrete substitutes with high compressive strength, (iii) a new material capable of multiple self- healing cycles, (iv) a new material that can sequester carbon.

Understanding the composition and internal structural mechanisms of self healing concrete and enzymatic construction material, developing testing standards, and establishing physical and chemical-based models for performance evaluation are all important to the scaling up commercial application of these materials.

1.2 Overview

To reduce the carbon dioxide emissions from concrete manufacture, three advanced materials were developed with different functions, including carbonic anhydrase modified self-healing concrete, enzymatic construction material and nanoparticle modified enzymatic construction material. Applying multiple characterization experiments, including scanning electron microscope (SEM), Powder X-ray diffraction (XRD), Fourier-transform infrared spectroscopy (FTIR), Raman spectroscopy and Micro-CT, etc., are combined with traditional theoretical calculation, which includes heat transfer modeling, crystal growth modeling. The above content

leads to a total of four chapters and is briefly outlined in Figure 1-1.

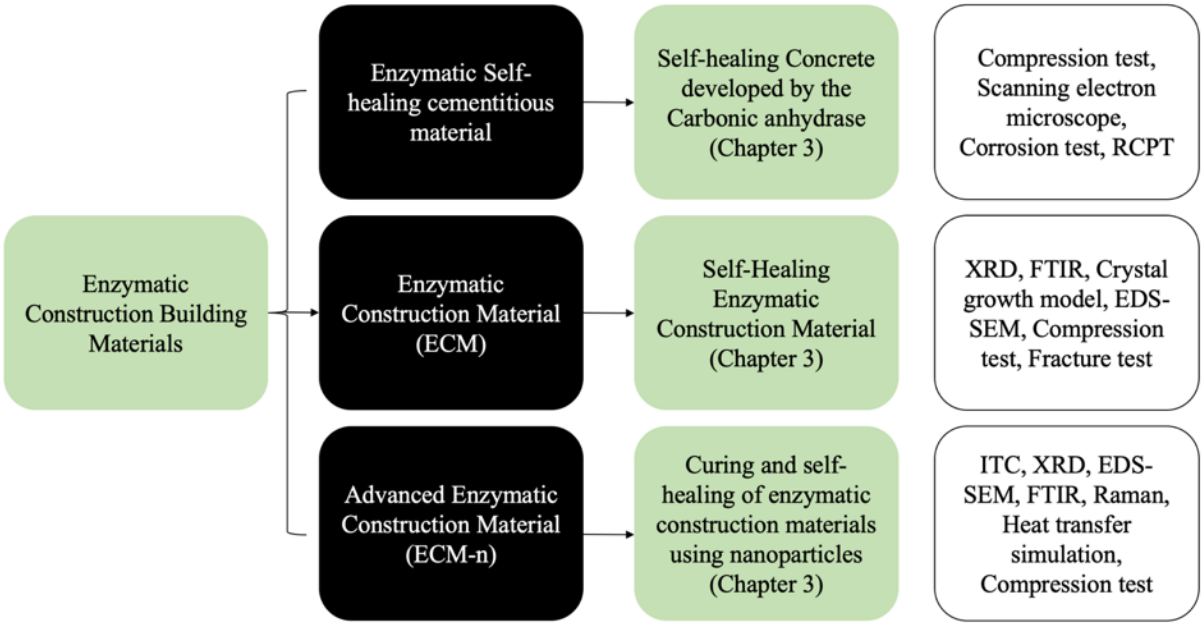

Figure 1-1. An overview of the dissertation research, along with the experimental and modeling employed.

2 Literature Review

This chapter starts with a review of the global challenge facing the cement industry, which motivates the search for sustainable alternatives with low CO_2 emissions and reliable mechanical properties. Thereafter, I briefly introduce carbon capture and sequestration and their relationship with infrastructure materials followed by a summary of existing biological construction materials with a particular focus on the key concepts, theories, and debates that have shaped the field to date. I then suggest the major material design framework and experimental method of the self healing enzymatic concrete, enzymatic construction materials and advanced enzymatic construction material and identify unknown fields of benefits and weakness in these materials. The issues that have been neglected in the field of bio-construction materials are reviewed, with

a focus on their strength mechanism on the microscale. Finally, the lower cost of material fabrication and scaling up method on an industrial scale will be highlighted and proposed.

2.1 Global Challenge

According to data from the International Temperature Dataset (ITD) compiled by the World Meteorological Organization (WMO), the past eight years have been the warmest on record globally, driven by rising greenhouse gas concentrations and accumulated heat. The global average temperature in 2022 is about 1.15 [1.02 to 1.27] above pre-industrial (1850-1900) levels [10]. The period from 2015 to 2022 is the warmest eight years on human record. Over time, the global average temperature is likely to break the Paris Agreement's 1.5 limits.

In 2022, several major weather disasters claimed many lives and livelihoods and undermined health security, food security, energy security, water security, and infrastructure. Global warming and long-term climate change trends are expected to continue as heat-trapping greenhouse gases accumulate in the atmosphere. Extreme heat waves, droughts and devastating floods affected millions of people and caused billions of dollars in economic damage, according to the WMO's Interim Report on the State of the Global Climate 2022 [11]. Large parts of North America were affected by strong storms in late December 2023. Some areas in the east were damaged widely by heavy snow and cold temperatures. Over 37 billion metric tons of CO_2 released from the earth, which contributed to 76% of greenhouse gas emissions, see Figure 2-1.

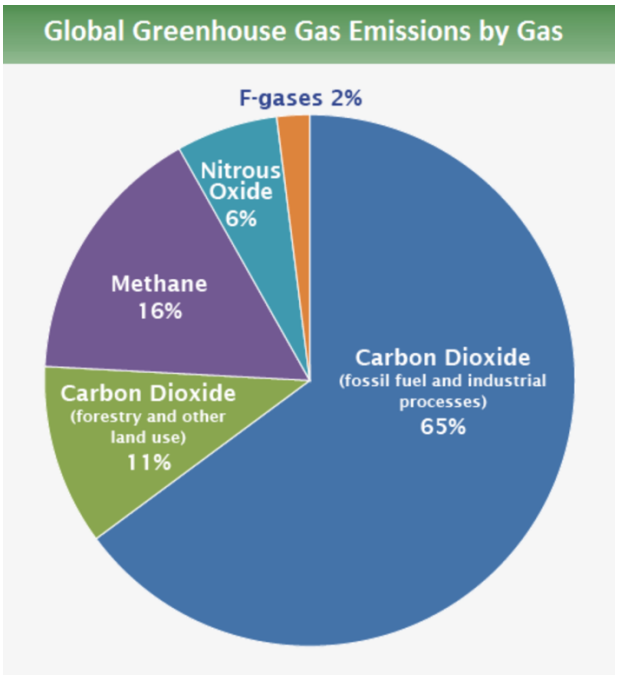

Figure 2-1 The overview of global Greenhouse Gas Emissions from 2010 [12].

2.2 Carbon capture, sequestration, and utilization in construction

Carbon capture, carbon sequestration, and carbon utilization have gained significant attention in recent years as ways to mitigate the impact of carbon emissions on the environment. Some research mentioned that restoring and protecting the world's soil could absorb more than 5 billion metric tons of carbon dioxide each year [13]. However, restricting the use of soil will undoubtedly have a huge impact on human survival. In the construction industry, carbon capture has been explored as a means to reduce the carbon footprint of building materials such as cement. wood and bamboo. Fehling et al. [14] investigated the use of carbon capture and utilization technologies to reduce the carbon footprint of cement production. The study found that carbon capture technologies could reduce the carbon emissions of cement production by up to 80%. Carbon sequestration is the process of capturing and storing carbon in natural or artificial reservoirs such as forests, soils, and geological formations. For example, Olivine, a type

of magnesium iron silicate mineral, has the ability to capture and store carbon dioxide (CO_2) through mineral carbonation. This process occurs naturally over geological time scales, as CO_2 reacts with olivine to form solid carbonates such as magnesite ($MgCO_3$) and serpentine ($Mg_3Si_2O_5(OH)_4$) [15]. A study by Borowski et al. [16] investigated the potential of using bamboo as a carbon sink in the construction industry because of its high growth rate. The study found that bamboo could sequester significant amounts of carbon and that it had the potential to be a sustainable alternative to traditional building materials such as concrete and steel. Carbon utilization involves using carbon dioxide as a feedstock for the production of value-added products such as fuels, chemicals, and building materials. Abomohra et al. [17] reported the resource of carbon dioxide as a feedstock for the production of bricks. The study found that the carbon dioxide cured bricks had similar compressive strength to traditional bricks and that they had the potential to reduce the carbon footprint of the construction industry. Carbon capture, carbon sequestration, and carbon utilization are emerging techniques in the construction industry that can be developed synergistically with carbon capture applications in different fields [18, 19]. While these techniques are still in the early stages of development, the current state of research suggests that they have significant potential to contribute to the sustainable development of the construction industry. Further research and development are required to fully realize the potential of these techniques, but they offer a promising way forward in the fight against climate change.

2.3 Autonomously self-healing concrete and method

Due to the benefits of durability, high strength, versatility and cost-efficient characteristics, concrete, the most consumed construction material in the world, is used in widespread infrastructures such as bridges, buildings, pavements, etc. Life Cycle Assessment results

revealed that to produce 1 m^3 of concrete, its production required 2,775 MJ of energy, accompanied by 410 kg CO_2 [20]. Due to the substantial increase in cement production, there has been a sharp rise in CO_2 emissions. In 1990, global CO_2 emissions from cement plants were 576 million tons, but by 2006, this figure had nearly tripled, reaching 1.88 billion tons. Without any intervention, it is predicted that the amount of CO_2 emissions from the global cement industry will reach 2.34 billion tons by 2050. The global carbon budget averaged over the last half-century is shown in Figure 2-2. Figure 2-2 displays the average global carbon budget for the past 50 years, indicating that fossil CO_2 emissions were responsible for 82% of the total emissions, while land-use changes contributed 18%. The emissions were distributed among the atmosphere (45%), ocean (24%), and land (30%). The global CO_2 emission can be calculated base from these data is around 40.3 $GtCO_2$/year.

The development of cracks in concrete is a major factor in compromising the functional integrity of the structure, thus limiting service life and sustainability because of unwanted events such as thermal deformation, external stresses and corrosion [22]. When cracks are exposed to the surface of the concrete, liquids, and gases (chloride ions) are able to penetrate the deeper layer of the structural matrix. Reinforcing rebar starts to contact the environment which causes a corrosion acceleration, whereby the risk of structure collapse is increased. Self-healing concrete was proposed and developed to improve the durability of concrete structures. Self-healing concrete was designed to repair cracks autonomously, without the need for human intervention. Autogenous healing is a natural self-healing process that occurs in the concrete due to the continued hydration of cementitious materials, which can heal cracks from 10 to 100 μm in month-long periods of time [23]. However, autogenous healing is restricted to minor cracks and several months time. The process is only effective in high-humidity environments, and it is

difficult to fully control and achieve ideal results. More importantly, the strength loss because the calcium source of naturally self-healing is consumed from the concrete matrix, which typically alters the integrity of the structure

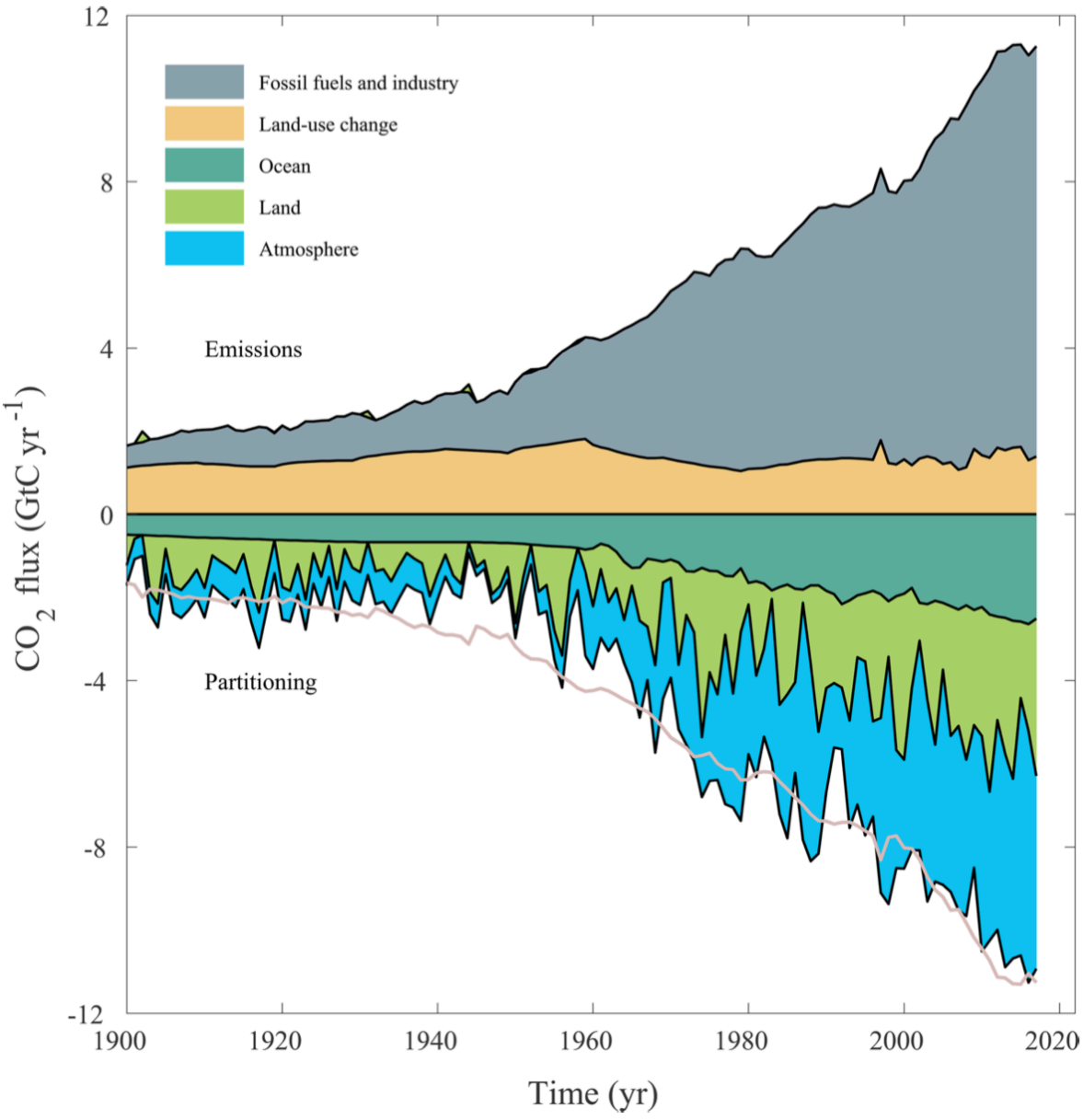

Figure 2-2 Combined components of the global carbon budget for fossil CO_2 emissions (grey) and emissions from land-use change (brown), as well as their partitioning among the atmosphere (blue), ocean (turquoise), and land (green) [21].

Researchers are exploring alternative approaches to self-healing concrete that can minimize the impact on the strength and integrity of the material. There are Several methods were proposed to design self-healing concrete. One method used mineral admixtures, such as fly ash [24], silica fume [25], and slag [26], which can improve the mechanical properties of concrete and promote autogenous healing. Another method is to apply bacteria in concrete that produce calcite, such as Bacillus pasteurii [27, 28, 29], Bacillus cohnii bacteria [30] and Sporosarcina pasteurii [31]. Another type of self-healing concrete is to use microcapsules that contain healing agents, such as methylmethacrylate or polyurethane, to self-heal cracks in the cementitious matrix. Engineered Cementitious Composites (ECC), a fiber-reinforced cementitious composite, due to the presence of microfibers within the cement matrix, allows the material to deform and redistribute stress when under load [32, 33, 34]. When cracks occur, the fibers in the ECC matrix can bridge the gap, forming a tight bond that prevents the crack from spreading further. However, all approaches mentioned above either only exhibit self-healing performance with cracks within micrometer scale and are time-consuming or expensive and add engineering complexity. Thus, an enzymatic self-healing concrete was proposed in order to better overcome these challenges.

2.4 Biological functional construction materials

Self-healing concrete production still uses cement as the matrix, the production of which releases CO_2. Alternatives to this cement need to be found. Nature provides us with a wealth of inspiration for designing sustainable and resilient infrastructure that relies solely on abundant natural resources. Some research about the development of biological materials in construction

structure was highlighted recently, such as fungal-based biomaterials developed by fungal mycelium which is grown on a particulate or granular lignocellulosic feedstock material for several days. The fungus consumes the feedstock material and infiltrates it, growing a dense hyphal mycelium network that binds together feedstock particles and fibers, thus forming a bulk biocomposite material [35, 36]. Calcium mineralization is a crucial method to immobilize carbon dioxide. The biomineralization process consists of the biological synthesis of minerals by microorganisms. MICP (Microbial-Induced Calcium Carbonate Precipitation) is a biochemical process that occurs in various environments such as soils, caves, freshwater, marine sediments, and hypersaline habitats. The microbial communities produce enzymes and other metabolites that facilitate the transformation of calcium and carbon-containing compounds into calcium carbonate. MICP has been extensively studied in recent years, and researchers are exploring its potential applications in a variety of fields, including construction, agriculture, and environmental remediation [37, 38]. MICP can be used to improve the mechanical properties of soil, reducing erosion and improving soil stability. Additionally, it can be used to sequester carbon, helping to mitigate the effects of climate change. Living building materials (LBM) were engineered that are capable of both biological and structural functions, which was created by inoculating an inert structural sand-hydrogel scaffold with Synechococcus sp. PCC 7002, a photosynthetic cyanobacterium [39]. Growing calcium carbonate on a polymer scaffold to provide the concentrated stress support for the structural function. Embedding of minerals into biological tissues and scaffolds is a very common process in nature, e.g., bone, enamel, or nacre, and leads to hybrid materials with extraordinary properties due to the synergetic interplay of inorganic and organic components at various levels of hierarchy ranging from the molecular up to the mesoscale level [40]. Natural composites achieve strength and toughness through complex

hierarchical designs that mimic natural structures in the synthesis of structural materials. Calcite mineralization was explored in various self-assembly composites and hierarchical composites. Researchers insert calcium carbonate crystals which are deposited deep inside the cellular structure of the wood to improve flame retardancy [41]. An, etc. exploits living bacteria and 3D-printed materials to grow bionic (such as stomatopod dactyl club) mineralized composites, which exhibit high specific strength and fracture toughness. The authors claim the material it is comparable to natural composites and has exceptional energy absorption capability superior to both natural and artificial counterparts [42]. Espinosa etc. added calcium carbonate platelets in the synthetic nacreous material that is able to further improve nacre's toughness [43].

2.5 Network formation of enzymatic construction materials (ECM)

Organic molecules and inorganic components merge within living cells in natural materials like bones, resulting in unique combinations of traits like regenerative capacity and mechanical resilience that synthetic materials lack. From the last decade, it seems impossible to create materials that possess both 100% self-healing properties and net negative carbon emissions through CO_2 consumption. Furthermore, there is no discussion about the material through biological approaches that can attain the same level of strength as conventional construction materials. The most cutting-edge bio-structural materials, in terms of carrier selection generally through the 3D printing of artificial carriers or plant-directed growth to build a certain strength of the platform, then as a scaffold to grow crystals [*44,* 45]. Designed to mimic cement concrete, the composite objects are lighter than traditional products and can be strategically inserted into structures to provide higher stiffness in areas with high demand. Through previous experiments and theoretical dual verification, we establish a three elements theory for biological construction

building materials (sand, scaffold, and mineral crystals) to assemble sand aggregate tightly together, achieving high mechanical properties. Similar to aggregate in concrete, which refers to the inert materials, such as sand, gravel, and crushed stone, that are mixed with cement and water to create concrete. The primary function of sand in ECM is to provide volume, strength, and durability to the finished product. The sand plays a crucial role in determining the properties of the ECM. The type, size, geometry, and roughness of sand used can affect the density, workability, and strength of the ECM. The use of appropriate aggregates is essential to ensure the desired performance and longevity of the ECM. Scaffolds are essential in biological functional materials because they provide a structure and support for the growth of new tissues, organs, and other biological structures. In tissue engineering, scaffolds are used as three-dimensional structures to support the attachment, growth, and differentiation of cells. The scaffold provides a template for the cells to attach and organize themselves into the desired tissue structure. The scaffold must have the appropriate properties, such as porosity, mechanical strength, and biocompatibility, to support cell growth and function. Scaffolds can also be used in the development of implantable devices, such as artificial organs or prosthetic limbs. And the scaffold serves as a framework for the attachment of biological components, such as cells or tissues, to create functional structures that can replace damaged or missing body parts. In building materials, the scaffold is chosen for providing mineral nucleation sites, guiding crystal growth, and bridging sand particles. It is equivalent to the joints and ligaments between human bones transmitting and connecting tissue information. Elements such as calcium, phosphorus, and magnesium are critical for the formation and maintenance of bones and teeth. These elements, when combined into minerals, provide the necessary strength and hardness to support the body and protect organs. On the other hand, mineralization is a process that allows

contributes to carbon sequestration by converting carbon from organic matter into inorganic minerals that can remain stable in soils for long periods [46]. Calcium is the major carbon sequestered constituent in ECM, which stores and captures CO_2 during material production. Calcite is also one of the most common minerals in nature and has relatively high compressive strength, which contributes both significant durability and strength within ECM. As a proof-of-concept, we recently demonstrated that ECM achieves high compressive strength and capable self-healing in six cycles by three components: sand, hydrogel and enzymatic calcite. More details are discussed in chapter 4.

2.6 The mechanism of mineral grow on polymer substrate

Biomineralization involves the formation process of mineral crystals by living organisms or through the use of biological materials. This process provides inorganic based skeletons with dynamic behavior, which is a complex and dynamic organ with both structural and metabolic functions. In the case of mineral growth on a polymer substrate, biomineralization can be induced through the addition of specific molecules or through the modification of the polymer surface.

The process of biomineralization simply concludes: first, create a conducive surface to mineral growth through the polymer substrate modification. Assigning functional groups can provide nucleation sites and applying a coating agent promoted chemical interaction between mineral and substrate. The mineral ions can be introduced to the system, either through a solution or through a template that directs the formation of the mineral crystals on the substrate [47].

When the mineral ions begin to nucleate and grow on the polymer substrate, the specific crystal crystallinity and morphology of the mineral can be influenced by the properties of the polymer substrate and the conditions under which the mineral growth occurs. Increasing the pH of the precursor solutions, particles will undergo polymorphic transformation from vaterite to calcite depending both on the pH values and the $[Ca^{2+}]$:$[CO_3^{2-}]$ ratios [48]. In some cases, the mineral crystals may grow in a specific orientation or pattern on the polymer substrate [49].

The challenging part of biomineralization is the incorporation of the mineral crystals into the polymer matrix. This can be achieved using coupling agents, adhesive proteins [50] or through the creation of hydrogen bonds between mineral-polymer interfaces. The resulting materials often have excellent mechanical properties, biocompatibility and multifunctionality compared to the original polymer substrate.

Crystallization takes place after nucleation sites formed on the substrate. Atoms or molecules aggregate together, and self arrange themselves during the solidification of the primary phase. The nuclei originate from clusters of solute molecules at the nucleation sites–solute interface. Nuclei originate from both mechanisms, with mechanical attrition being promoted at higher contact forces [51]. Molecular aggregates from solution nucleate to form crystallite on the surface of a seed crystal which catalyzed further nucleation [52]. Figure 2-3 presented an example of crystal nuclei breeding on the substrate surface under micrometer scale. The experimental investigation of crystal growth was performed using a fresh seed of paracetamol crystal. The surface topology of a seed exhibited a change from smooth texture to rough texture of the surface.

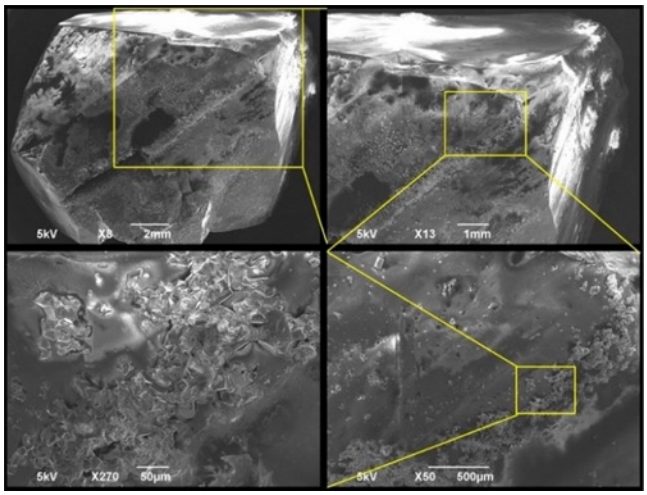

Figure 2-3 the SEM images of crystal nuclei breeding on the mineral substrate surface [53].

Overall, the mechanism of mineral growth on a polymer substrate involves the modification of the substrate surface, the nucleation and growth of the mineral crystals, and the incorporation of the mineral crystals into the polymer matrix. These processes can be controlled and optimized to create materials with tailored properties for a variety of applications.

2.7 Interface and adhesion study within ECM

The adhesion between the individual layers in crystal growth such as calcium carbonate and sand, calcium carbonate and polymer scaffold, sand and polymer scaffold is important for understanding mechanical mechanisms in the biological functional materials. The interfaces of crystal growth on scaffold substrate have not been investigated systematically. Hence, in recent years, dual focused ion beam-scanning electron microscopy (FIB-SEM) and atomic force microscopy (AFM) techniques have been developed for the analysis and measurement of physical and chemical components in interface and the adhesion between surface pairs that are relevant to the robustness of interfaces in material systems. FIB-SEM is a powerful tool for site-specific

sample preparation and subsequent analysis by EDS, TEM, and BSE to the highest energy and spatial resolutions. It provides a cross-section view of the sample's interior for mechanism study. The AFM has emerged as a powerful tool to obtain nanostructure details and biomechanical properties of biological samples, including biomolecules and cells [54] [55]. It also can measure the changes in the mechanical property such as adhesion between two single nanoparticles. FIB-SEM enables the characterization of the internal morphology of the cell, which in conjunction with AFM, provides important information on the adhesion force and interface morphology, which are affected by various processes occurring during the molecular interfacing with surfaces and 3D structures. In the calcite crystal and polymer scaffold, the surface layer of the scaffold determines the stabilization of crystal on the scaffold given by either the chemical properties for the functional groups creating hydron bonds or and physical phenomenon for the van der war bonds by roughness to reach the steady state. The interface adhesion of calcite and silica is comparatively weak, which is crucial to the overall strength of the material, and it is necessary to improve the final mechanical properties by initially developing the adhesion between calcite and silica.

2.8 Expected cost and engineering scaling up

Bringing materials from the laboratory to the real-world application environment is often more complex than the phase of materials development. Many materials remain at the laboratory level and do not progress to widespread commercial use. The most common challenges arise mainly from excessive costs, the lack of effective scaling-up methods and competition from existing materials. The comparison of ECM, LBMs and concrete is listed in Table 2-1. Sand is a naturally occurring granular material composed of rock fragments, minerals, shells, and other particles. The carbon dioxide can be considered zero and the cost is only generated from the

extraction and transportation. The carbonic anhydrase is isolated from all mammalian tissues, plants, algae, and bacteria, and with the development of mass production can be obtained relatively cheaply. Calcium can be obtained from natural brines or seawater, where abundant mineral ions can be extracted easily with instrument upgrading. Gelatin is extracted by hydrolysis of biological materials. Producing 1kg gelatin/hydrogel will release 3k CO_2, which means produce 1kg ECM will release from gelatin/hydrogel production. The cost of food service used gelatin is available on the market for around $10 per pound. Over 90% of ECM is sand, which reduces the difficulty of scaling up the ECM. The preparation, fabrication and curing process of ECM is similar to concrete production, However, a large transformative technology should be ready for the production of new materials. The existing concrete preparation instruments can be used to prepare ECM, and the curing period for ECM is one day, much less than the 28 days required to fully cure concrete.

Table 2-1 The cost, amount of CO_2 emission, net CO_2 absorption and health impact of concrete, LBMs and ECM.

Standard brick (92 x 57 x 203 mm)	**Cost**	**CO_2 emission/year (included raw materials production)**	**Net CO_2 Absorption**	Health Impact
Concrete	~$1	8% of the world's **carbon dioxide**	1kg release 1kg	Slightly
LBMs	~$360	No data record	No data record	Chronic diseases
ECM	**~$60**	**~0.1kg/kg (from hydrogel production)**	**>0.2kg/kg**	No

Chapter 3

Chapter Information: Jessica A. Rosewitz, Shuai Wang, Suzanne F. Scarlata, Nima Rahbar, An enzymatic self-healing cementitious material, Applied Materials Today, Volume 23, 2021, 101035, ISSN 2352-9407**, https://doi.org/10.1016/j.apmt.2021.101035.**

Authorship contribution statement: Shuai Wang: Formal analysis, Methodology (self-healing experiment and test accordingly), Writing (self-healing section)- review & editing.

3 Self-healing Concrete developed by the Carbonic anhydrase enzyme

3.1 Abstract

Concrete is the most widely used material in the world and is responsible for 8% of global carbon emissions. It is inherently brittle, and it requires frequent repair or replacement, which are expensive and generate large volumes of CO_2. Current methods of repair by agents such as mortar and epoxies result in structures with reduced strength and resiliency due to material mismatch, therefore, a self-healing cement paste (concrete's main matrix) is needed to overcome this problem. The most well-known self-healing mechanism is based on the use of bacteria and microbes, which are slow and have limited applications, as well as unknown health effects. Inspired by the extremely efficient process of CO_2 transfer in biological cells, this study introduces a method to develop a self-healing mechanism in a cementitious matrix using trace amounts of the enzyme Carbonic Anhydrase (CA). CA catalyzes the reaction between Ca^{2+} ions and atmospheric CO_2 to create calcium carbonate crystals with similar thermomechanical properties as the cementitious matrix. The crystal growth rate using this method is orders of magnitude faster and more efficient than bacterial methods, resulting in the healing of large flaws on timescale orders of magnitude shorter. This method is capable of self-healing samples with millimeter-scale flaws within 24-hours and is significantly faster than all current methods

that need a minimum of 28-days for strength recovery of microscale cracks. This inexpensive method is biologically safe, actively consumes CO_2 and avoids using unhealthy reagents. It can be an efficient mechanism to repair and strengthen the existing concrete structures.

Keywords: Enzyme; Cementitious; Self-healing

3.2 Introduction

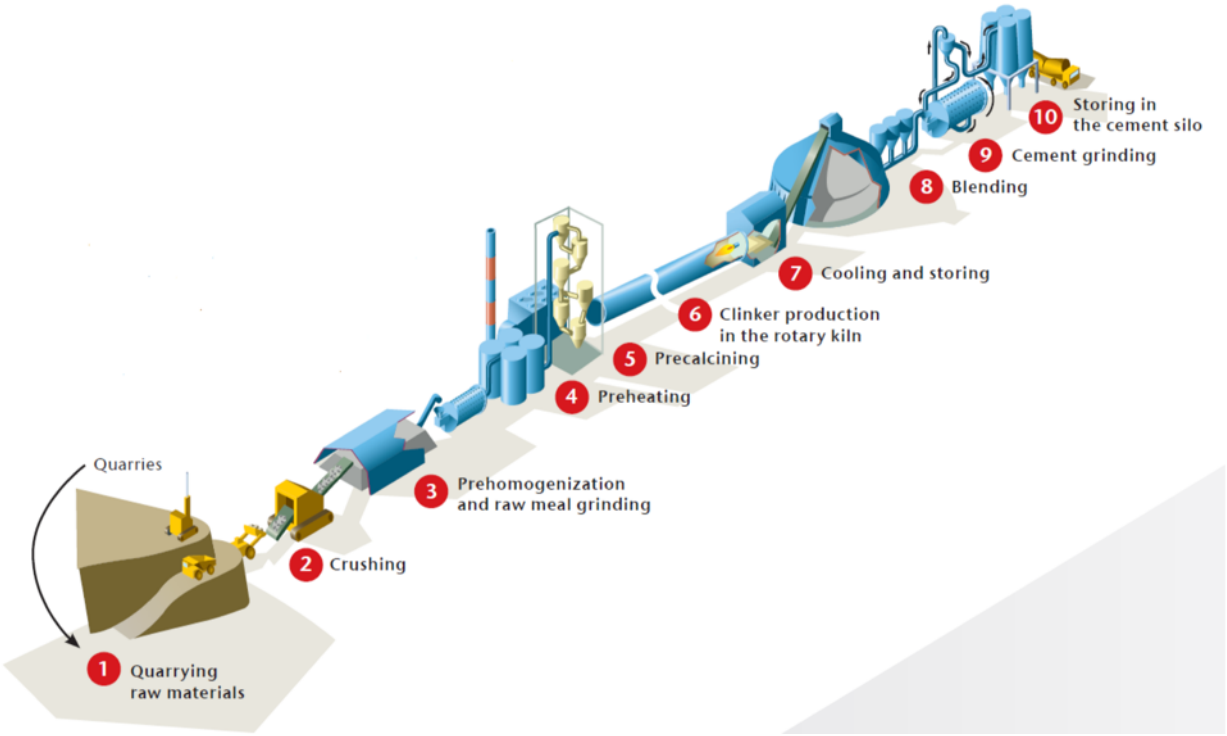

Figure 3-1 Cement industry production procedures.

Most infrastructure is composed of concrete, and indeed, in its many forms, it is the single most used material in the world. However, the use of concrete comes at an environmental cost. Figure 3-1 showing a details of cement production from manufacturing and the major carbon dioxide released from clinker production [56]. While the production of concrete materials does not produce a large volume of carbon emissions by itself, its sheer volume is responsible for

almost 8% of human made global carbon emissions [57], and 3% of global energy demand [58]. Therefore, healing rather than replacing concrete offers a significant benefit to the environment. Here, we present a new paradigm by introducing a novel mechanism to naturally heal cement paste that actively consumes CO_2 rather than generates it.

Inherent brittleness of concrete leads to damage through several mechanisms such as freeze-thaw cycles pervasive in our environment. Current repair processes for cracked and damaged concrete rely on matching dissimilar materials, such as the inorganic C-S-H of concrete with organic petroleum-derived epoxies. The success of repairing concrete by patching and resurfacing processes relies upon the removal of the damaged material, which can cause further damage. Universally, rehabilitating concrete with mismatched materials creates additional flaws in the repairs, undermining the process [59]. The repair process can take several forms, but the general first step is to chip away until only sound concrete remains, often exposing the reinforcing steel bar. One study found that only around 50% of repairs are durable while around 25% failed [60]. Furthermore, only after 5–7 years, most repairs failed. The main mechanisms of failure here are the bond breakage between materials due to chemical attack, thermal fluctuation, and inadequate preparation or application.

Here, inspired by the extremely efficient process of CO_2 transfer in biological cells, we present an enzyme-driven mechanism to repair cracked and damaged cement paste matrix that eventually results in a tougher and less permeable material [61]. Biological enzymes are proteins that catalyze a chemical reaction at an extremely rapid rate without being consumed in the process and are inherently safe and reliable [62]. Our method uses the carbonic anhydrase enzyme that is a natural enzyme found in all living organisms including humans. CA catalyzes the reaction between water, calcium ions (Ca^{2+}) (calcium chloride dyhydrate) and CO_2 to

produce calcium carbonate ($CaCO_3$) [63], which, as we show, self-assembles into a stable material that incorporates into the cement paste structure to fill the cracks. CA is the fastest known enzyme for this process and produces calcium carbonate at an exponential rate limited only by diffusion [64, 65] Contrary to other repair materials, such as organic epoxies, calcium carbonate is a material with similar thermal and mechanical properties to cement paste and will produce a final product that has similar strength, thermomechanical properties modulus, and thermal expansion coefficient. This CA method will, therefore, result in a material with significantly improved mechanical properties over conventionally repaired material by removing the stress concentrations that arise from material dissimilarities. Because CA is not consumed in the reaction, only a small amount is required. It can also remain in the cement paste structure for extended periods (since it is not a living species) even in an unprotected form, thereby enabling the potential for self-healing properties in the long-term. Most importantly, the small size of the CA molecule allows deep penetration in thick substrates.

Our method involves incorporating CA into a cement paste mix, which is the first step in developing a self-activated healing cement paste mix. At this stage, we have shown evidence of self-healing by crystal growth triggered by hydration in enzyme-modified samples. We have also presented the complete regaining of strength in 24 h for a cement paste sample with a 3×1 mm flaw. We find that the enzyme is viable after the wet cement paste mix cures into a solid phase. Not only does this method present a paradigm shift for rapid, strong, and safe healing of cement paste, but it is also a modern demonstration of an environmentally conscious solution for a materials problem. The overall process is presented in Figure 3-2.

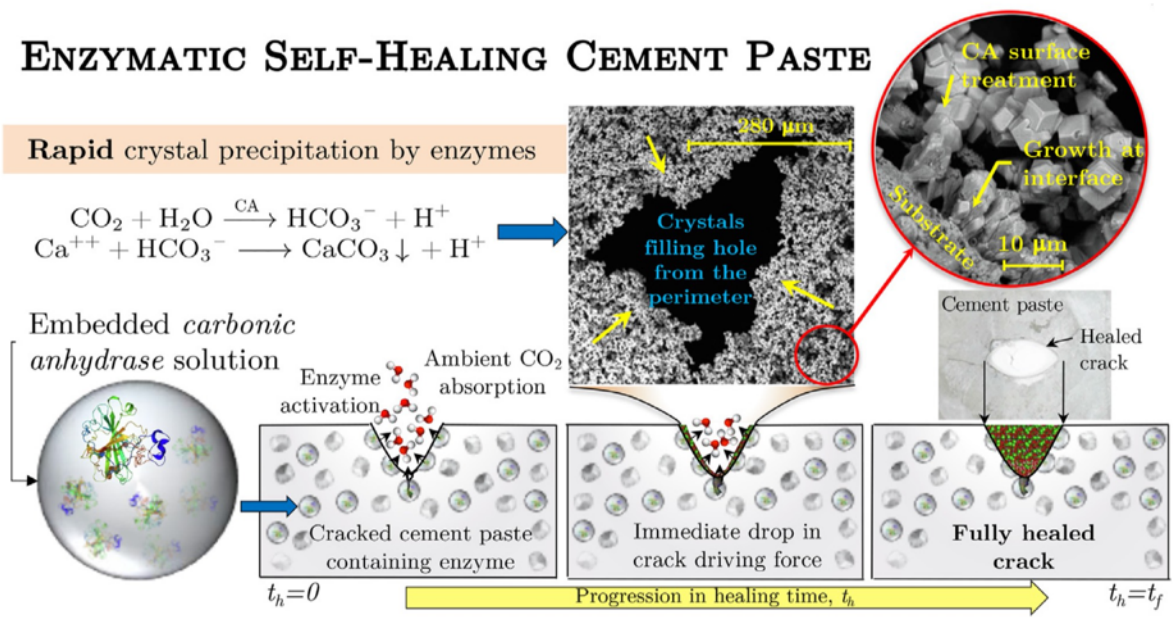

Figure 3-2 Self-healing extremely durable cement paste using enzymes.

3.3 Materials and methods

3.3.1 The Carbonic anhydrase enzyme

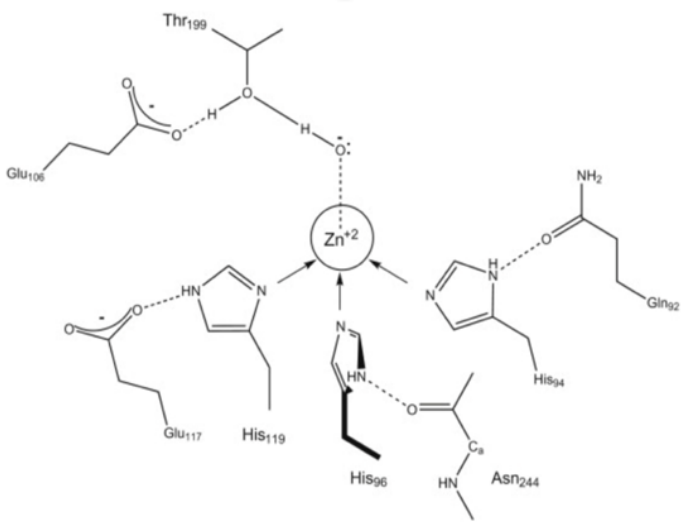

a)

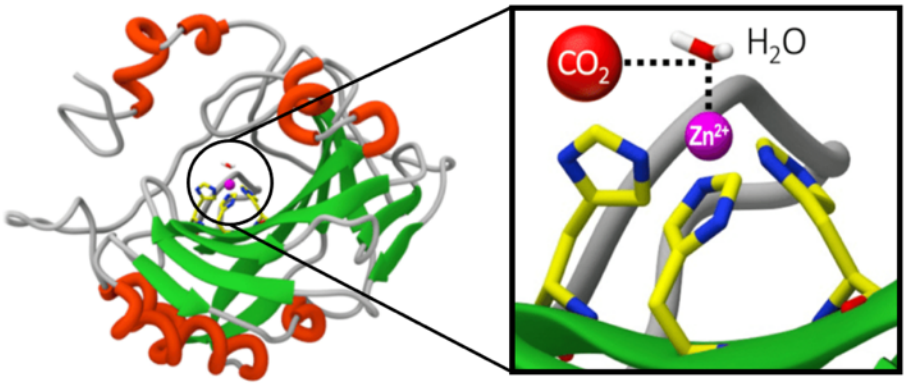

b)

Figure 3-3. The active site of human carbonic anhydrase. Ribbon representation of the carbonic anhydrase (CA) enzyme. (b) Active site of CA determined by molecular simulations (vide infra).

A zinc ion (Zn^{2+}) surrounded by three coordinating histidine and a water molecule comprises the active site [66].

Enzymes are proteins that, in the simplest sense, catalyze, or speed up, the rate of a biological reactions. They are not bound to the end products of the reaction but rather maintain the same properties whether they have catalyzed one reaction or thousands of reactions. CA is the fastest known enzyme with an extremely high rate of turnover that is almost diffusion controlled [66, 67]. CA catalyzes the reversible hydration of carbon dioxide (CO_2) and water (H_2O) to bicarbonate (HCO_3^-) and protons (H^+) through the following reaction (Figure 3-3):

$$CO_2 + H_2O \overset{CA}{\rightarrow} HCO_3^- + H^+ \quad (3\text{-}1)$$

$$Ca^{2+} + HCO_3^- \rightarrow CaCO_3 \downarrow + H^+ \quad (3\text{-}2)$$

and in the presence of calcium ions, the calcium carbonate forms and precipitates out of solution. In this way, the reaction is essentially irreversible, and the enzyme will keep rapidly forming calcium carbonate until all the reaction reactants are consumed. The physical orientation and structure of the amino acids that make up the proteins determine the function of any enzyme [67].

3.3.2 Self-healing experiment on cement mortar

To perform the healing process, the self- healing enzyme-modified cement paste mix was created out of dry and sieved Portland cement powder, deionized (DI) water, and the CA enzyme, termed “CA-Mod” in section Compressive strength of Repaired concrete and “ESH” in

section Compressive strength of self-healing concrete. The CA enzyme 100 µL of 100 µM concentration in DI water and cement with a mass ratio of 0.4 was mixed for 2 minutes to prepare the samples (The samples mix design is described on Table 3-1 Summary of mix preparation data for control and CA-Mod sample batches: CA-Mod-5x).

To achieve the healing purpose, a millimeter-scale cement paste was designed, which required the creation of custom molds. The molds were cast from a silicone rubber, which was pliable enough to remove the samples from the mold undamaged. The silicone molds were created by casting into a 3D printer. A 7.8 mm × 7.8 mm × 3 mm cube-shaped cement paste with a 3 mm × 1 mm vertically oriented elliptical flaw was created with and without flaws for compression testing to compare intact control samples to those with flaws self-healing with the enzyme. 14 curing days samples were selected for all of the self-healing samples. Aqueous solutions of the 0.1 M Tris buffer and 2M calcium chloride are thoroughly mixed and used to perform self-healing process (see Figure 3-5 for details of the two-part enzyme solution).

Table 3-1 Summary of mix preparation data for control and CA-Mod sample batches.

Notation	Portland cement (g)	Water (g)	Water to cement ratio	CA amount (μL) and concentration (μM)
Control	200	80	0.4	0
CA-Mod-5x	200	80	0.4	100 μL, 100 μM

A small amount (to just wet the entire surface slightly) of calcium solution was sprayed onto the entire surface of flawed sample then placed it into an Erlenmeyer flask and pulped with a single-hole rubber cap. A rubber tube connected with a carbon dioxide tank, which enters the flask through the hole to fill with carbon dioxide. The flask is filled with CO_2 for about half an

hour, turn off the carbon dioxide gas, and the white particles can be observed on the surface. When the surface is fully desiccated, spray a small amount of calcium and CA mixing solution again and fill with CO_2 gas. Repeat the above steps every two hours then put the sample into a $60°C$ oven for additional 24 hours of drying.

The self-healing samples and control (Figure 3-3) were tested for compressive strength following the methods in ASTM C109 [68]. Uniaxial compressive loading was recorded with an electromechanical load frame with a maximum limit on the load cell of 31.5 kN (Instron 5567AR1986, Instron, Norwood, MA, USA), conducted under displacement control at a rate of 1.27 mm/min. Testing was conducted at ambient temperature ($23°C$).The compression test set up and failure samples are shown on Figure 3-4.

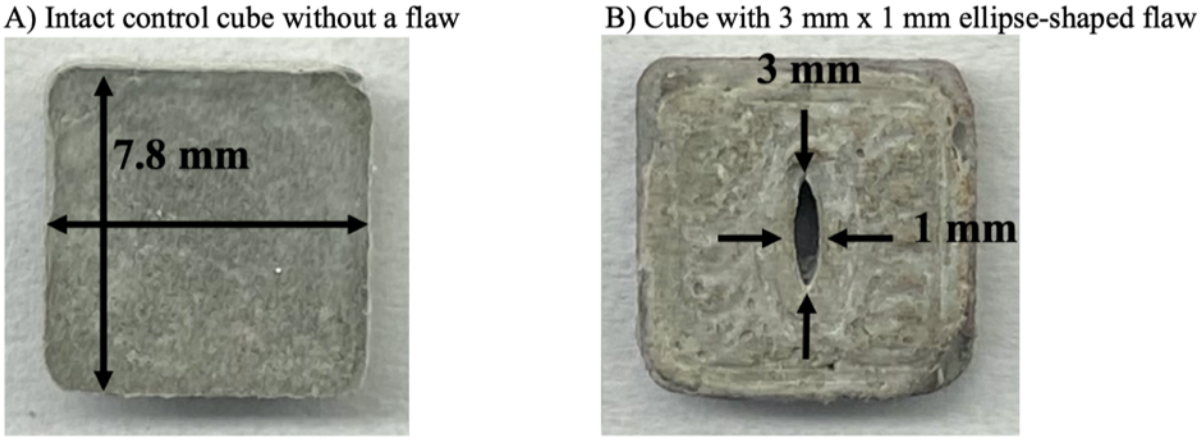

Figure 3-4 The 7.8 mm × 7.8 mm × 3 mm cube-shaped samples used for compressive strength testing. A) An intact control sample; B) A flawed sample with a manufactured 3 mm tall by 1

mm diameter ellipse shaped through hole.

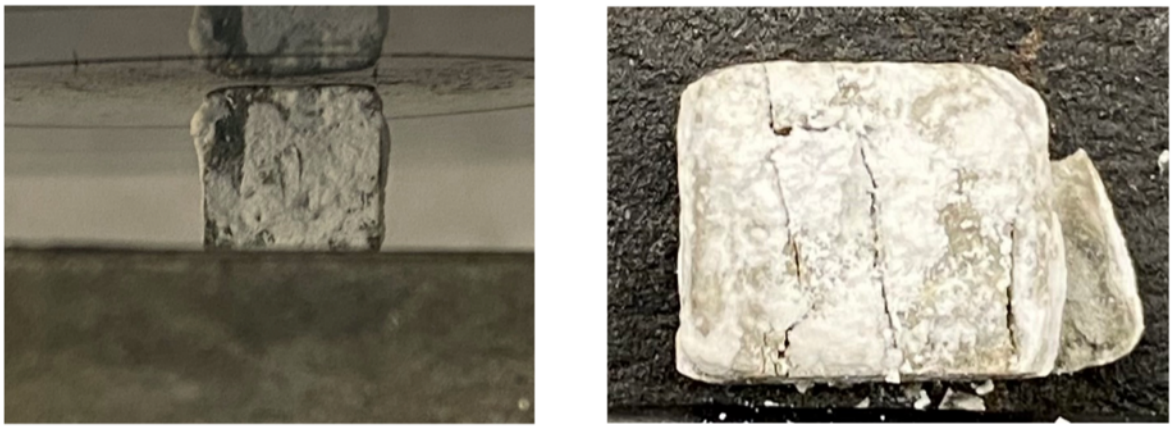

Figure 3-5 (Left) The experiment of compression for 7.8 mm × 7.8 mm × 3 mm rectangular prism sample. (Right) shown the sample is failure after compression.

The enzyme catalyzed self-healing process begins with the preparation of a two-part solution in a beaker on a stir plate. Solutions of the 0.1 M Tris buffer (PH = 8.3) and 2M calcium chloride are thoroughly mixed by stir bar for 2 min and then sprayed on the surface of CA enzyme modified cement pasted sample with crack (Figure 3-4). Sample is placed into flask and plug with a single hole rubber cap. CO_2 gas are enter into the sealed flask through the tube and the calcium carbonated crystals would produce by CA enzyme catalyzation. (Figure 3-6).

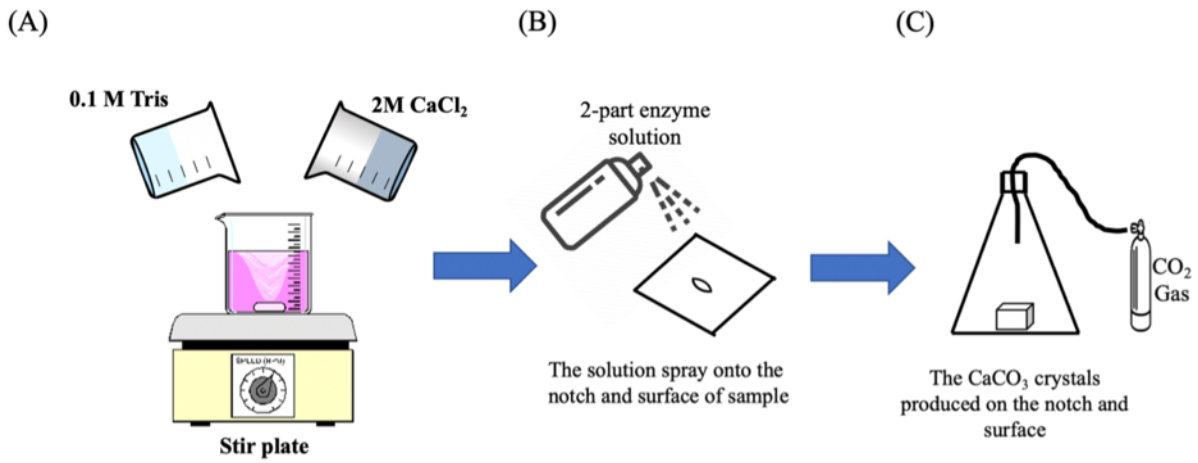

Figure 3-6 The preparation process of 2-part enzyme solution, solution treatment of flawed cement paste samples, and CO_2 treatment of flaws in the cement paste samples. (A) A 50/50 mix of aqueous 0.1M tris buffer and 2M Calcium chloride are mixed by stir bar. (B) Then mixing solution is sprayed on the CA enzyme modified sample surface. (C) The carbon dioxide gas is entered through flask for 20 minutes to assist self-healing process.

Concrete's main function is to carry compression. The compressive force is essentially carried by the cement paste that adheres the particles together in the matrix. Hence, to clearly present the evidence of self-activated healing using the proposed mechanism following the procedure similar to MICP, described in the SI section: Details of the self-healing method, we compared the mechanical strength of the 7.8 mm × 7.8 mm × 3 mm square shaped samples with a 3 mm × 1 mm vertically oriented elliptical flaw prepared in three ways: cement paste samples with carbonic anhydrase, noted here as CA-Mod-5x, notched and intact control cement paste (i.e. no prefabricated flaw) samples. All of the sample mixing designs were consistent with CA-Mod-5x and were cast and cured in the curing room for 14-days. A small amount of aqueous calcium solution described in previous paragraph was sprayed on the CA-Mod-5x sample's surface and

placed in a chamber containing CO_2 for 24 h. This is done to replicate the MICP self-healing method for comparison, as it is not possible to repair large defects without the presence of extra calcium. The samples were then dried for 24 h in the 60 ℃ and tested for compressive strength. The results presented in section 3.4.3.

3.3.3 Microstructure analysis

The calcium carbonate crystals deposited on the surface of the CA-Mod-5x samples are shown in Figure 3-7. After the CA treatment on a CA-Mod-5x substrate, SEM shows a dense layer on the substrate composed of many interconnected cubic-shaped calcium carbonate crystals (Figure 3-7 A). The CA treatment also repairs a hole from the perimeter inward, with crystals building and growing on each other to fill the void (Figure 3-7 B). A free end of a cluster from the CA treatment shows interconnected crystals (Figure 3-7 C). The interface between the CA treatment and the CA-Mod-5x substrate (Figure 3-7 D) shows a columnar growth at the interface layer between the substrate and the crystals from the CA treatment. This interfacial growth suggests a strong bond between the self-activated repair and the substrate.

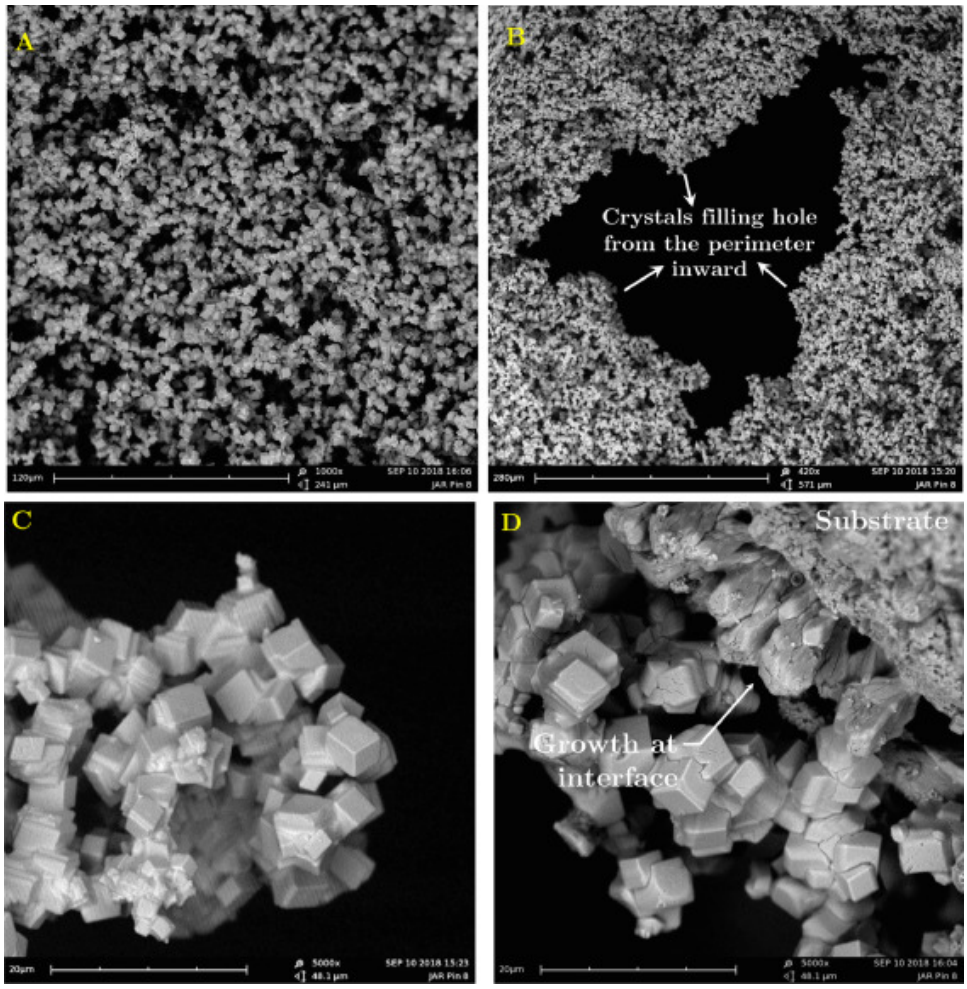

Figure 3-7 SEM images of the CA treatment on the CA-Mod-5x substrate, with scale bars. A) The CA treatment, 1000X. B) The CA treatment filling a hole from the perimeter, with crystals building and growing on each other to fill the void, 420X. C) A free end of a cluster from the CA treatment shows interconnected crystals, 5000X. D) Crystal growth at the interface between the CA-Mod-5x substrate and the CA treatment shows bonding to the substrate and transition to the CA treatment, 5000X.

3.3.4 Chloride ion permeability by RCPT

The rapid chloride permeability test is a standard test method (ASTM C1202–19) [69] used to determine the chloride ion penetration resistance of concrete. The test measures the time it takes for chloride ions to penetrate into a concrete sample under an electrical field. The test is conducted by applying a voltage between two electrodes embedded in the concrete sample, and then measuring the electrical current that flows through the sample. In this method, the electrical current can be used to accelerate the chloride ingress into concrete. Using this approach, a traditional 90-day in-situ ponding test can be replaced by a 6 hours chloride ion penetration test. Figure 3-8 describes the principle of experiment set up. By inducing an electrical current through a sample suspended between cathode and anode solutions, this method conducts nondestructive testing to determine chloride permeability. The current accelerates and increases chloride ingress into concrete, which allows for results to be obtained in just 6 hours instead of 90 days for a traditional in-situ ponding test. The size of concrete samples is 100 mm in diameter and 50 ± 5 mm thick, cut with a diamond band saw from cylinders of nominal 4”x8” size cast in the curing room for different periods. After slicing, the ribbed cut face was sanded smooth to reduce damaging a mesh sieve in the testing apparatus. The negative cell is filled with a 3% NaCl solution, and the positive cell with a 0.3N NaOH solution. The test cell is checked for leaks and sealed as necessary with silicone high vacuum grease. The negative lead is connected first, then the positive to a 60 V power supply. After 6 hours, the resistivity of the concrete sample is measured and plotted, and the total coulombs passed through the sample is summed at the end of the test.

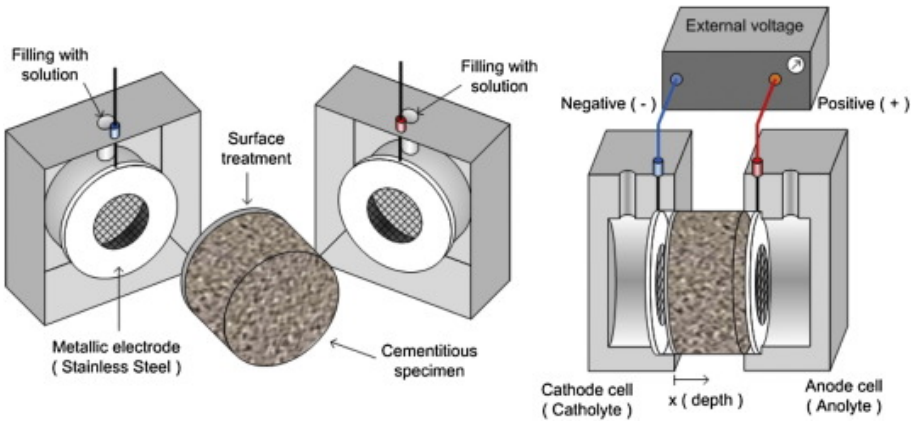

Figure 3-8 Cell-face view and test arrangement of RCPT for the sectional carbonic anhydrase modified concrete specimen [70].

3.3.5 Accelerated vacuum test

The concrete cement samples were cast in cylinder molds of 50mm by height X 100mm by diameter. Then, a curved watch glass (beaker cover) was pressed into the top of the samples, convex side down. This produced a concave top on each cylinder sample, in effect creating a depression to retain water. After curing in a steam room for required days, a silicone ring was placed around the top of the sample. This process is to create a larger space to hold more water than the concave top in the concrete cylinders. Cured cylinders were than dried at room temperature for three days to remove moisture from the sample pores. Then 10 mL of a 10,000-ppm fluorescent red dye was pipetted into the convex top, then the samples placed in a glass vacuum chamber, and pumped for 10 minutes. The chamber was sealed, and vacuum maintained for 24 hours. The next day the pump was run for anther 10 minutes, the chamber re-sealed, and this process repeated for three days. On the fourth day, it was observed that the 10 mL of dyed water had completely adsorbed into the cylinders. After three days drying, the cylinders were conducted the splitting test following the standard ASTM C496 [71]. The split tensile test is an

indirect way of evaluating the tensile strength of concrete. In this test, a standard cylindrical specimen is laid horizontally, and the force is applied on the cylinder axially on the surface which causes the formation of a vertical crack in the specimen along its diameter. The splitting tensile experimental setup is shown in Figure 3-9. After test, the inner penetration of the dye was observed under ultraviolet light.

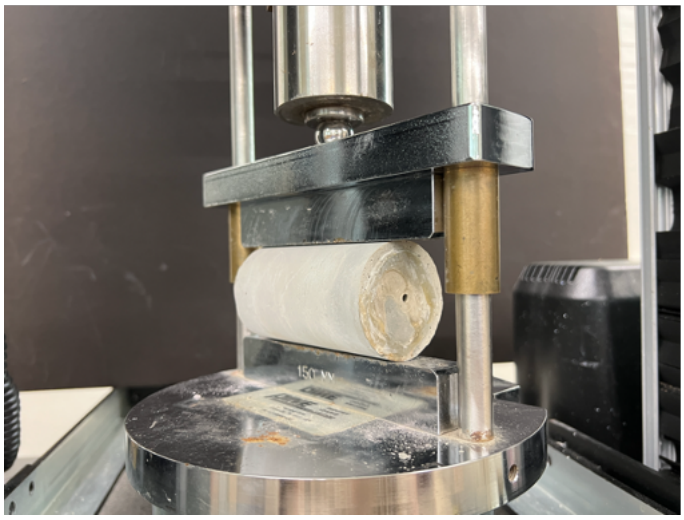

Figure 3-9 The splitting tensile test experiment set up for 2x4 in cylinder concrete samples.

3.3.6 Accelerated Corrosion Test

An experiment was conducted to evaluate the effectiveness of adding CA to reduce corrosion. To simulate natural corrosion on reinforced concrete, a fast and reliable test called the Accelerated Corrosion Test (ACT) was utilized. The ACT involves a plastic tank containing a 5 wt% NaCl solution, two stainless steel plates acting as cathodes, and a 30 V DC power source. The test specimens were 4 x 8 in cylinders filled with mortar and embedded with a 1ft wire-brushed steel rebar at the center to act as the anode for current transport. The sodium chloride solution served as the electrolyte in the experiment. To accelerate the corrosion process and shorten the test period, an anodic potential of 30 V was applied. To prevent crevice corrosion,

epoxy was applied to the top of the concrete cylinder where the rebar exited the mortar. After curing, the samples were placed into the ACT and a data logger recorded the voltage. The experiment schematic diagram and laboratory setup are presented in Figure 3-10. The initiation of corrosion was observed at the deflection point (lowest point) of voltage curve.

a) 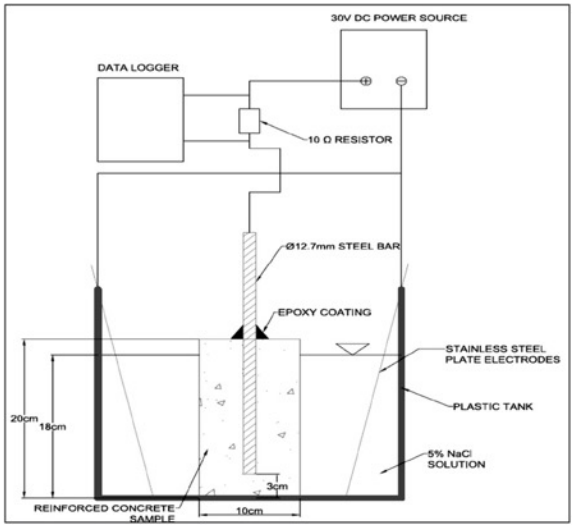

b) 

Figure 3-10 a) Schematic of accelerated corrosion test (ACT) for rebar reinforced concrete [68], b) corrosion experiment set up of enzyme modified reinforced concrete.

3.3.7 Carbonic anhydrase repaired cement paste

Several small-scale cement paste samples were prepared in this manner and used for testing. A 25 mm cube sample was created with and without flaws for compression testing (Figure 3-11), to compare intact control samples to those with flaws repaired with the enzyme product. A 10 mm diameter by 3 mm thick circular coupon chip was cast and used for optical microscopy of a sample self-healed and repaired with the four-part enzyme solution (Figure 3-11).

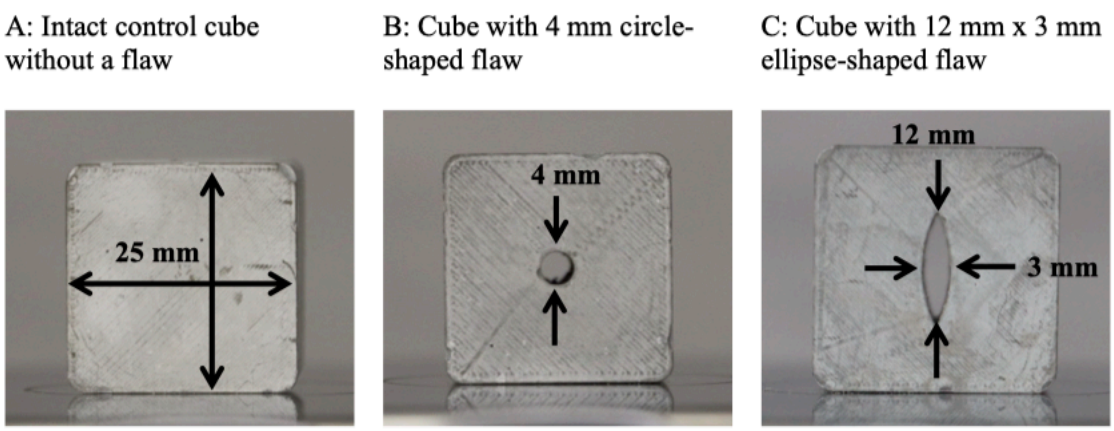

Figure 3-11 The 25 mm cube-shaped samples used for compressive strength testing. A) An intact control sample; B) A flawed sample with a manufactured 4 mm diameter circle-shaped through hole; C) A flawed sample with a manufactured 12 mm tall by 3 mm diameter ellipse-shaped through hole.

The enzyme catalyzed repair process begins with the preparation of a four-part solution in a beaker on a stir plate. Solutions of the Carbonic anhydrase (CA) enzyme, a 0.1 M Tris buffer, and 2M calcium chloride are thoroughly mixed and then ultrapure carbon dioxide gas is bubbled through (Figure 3-12, left). As the CA enzyme creates calcium carbonate through catalysis of the carbon dioxide to bicarbonate conversion (releasing an H^+) so that Ca^{2+} from dissolved calcium chloride and carbonate derived from deprotonation of bicarbonate (releasing another H^+), the pH of the solution decreases. Over a 20-minute time period of catalysis, the pH drops from an initial value of 9.6 to a final value of 7.4. At this point, the carbon dioxide gas is removed, and the solution is maintained on the stir plate (Figure 3-12 B&C).

The aqueous calcium carbonate solution is now ready to be used to fill large holes or flaws in intact cement paste samples, or to plug surface pores and repair surficial defects. For

samples where the need is to fill a small discrete hole, the aqueous calcium carbonate solution is placed into a funnel directly over the hole (Figure 3-12 right). For other samples which are to be fully coated over their entire surface in order to plug pores and repair surficial damage, then a sample is placed into the beaker of suspended calcium carbonate. In all repair cases using the suspended calcium carbonate, the calcium carbonate settles and self-assembles onto cement paste surfaces.

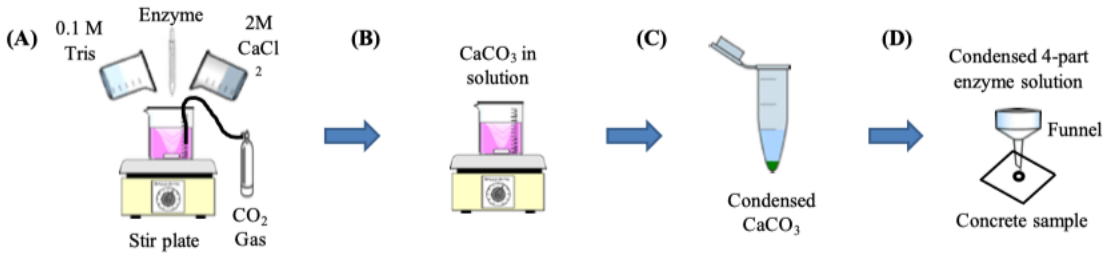

Figure 3-12 The preparation process of 4-part enzyme solution, creation of calcite crystals in solution, and treatment of flaws in the cement paste samples. (A) A buffered solution of the CA enzyme is added to a 50/50 mix of aqueous 0.1M Tris buffer and 2M calcium carbonate. (B) Then carbon dioxide gas is bubbled through for 20 minutes to create an aqueous solution of calcium carbonate. (C) The solution is centrifuged to remove excess supernatant and condense the calcium carbonate in solution. (D) To repair a flaw in a cement paste sample, a funnel is placed directly over the flaw into which the aqueous calcium carbonate solution is poured. The calcium carbonate settles and self-assembles onto the cement paste surfaces.

3.4 Results and Discussion

3.4.1 Mechanism of Self-healing

The self-activated healing mechanism relies on the long-term survival of the CA enzyme within the cementitious matrix. The CA enzyme is inherently stable, thus making it an ideal candidate for the extreme 12–13 pH of fresh concrete. Its ability to survive in the repaired cement paste matrix was studied over time, and the CA-Mod-5x mix design was evaluated for potential in establishing a self-activated healing mechanism in cement paste mix using SEM. While the morphology of the control cement paste samples shows surface irregularities and unhydrated cement needles (3-13 A), the surface of CA-Mod-5x samples shows a regular and even substrate (3-13 B). After the initial curing, the CA-Mod-5x samples were soaked in DI water for 7 days, and SEM was used again to investigate crystal formations. The investigation showed large crystals present on the surface (3-13 C), which are the result of the CA enzyme within the CA-Mod-5x substrate. Figure 3-12 D shows a cluster of these partial cube-shaped crystals ranging from 5 μm to an impressive 20 μm, at higher magnification, with the CA-Mod-5x substrate present in the background. The samples were soaked in DI water for 7 days, then oven dried at 50 ℃ for 3 days and imaged with SEM. These results show that, in the CA-Mod-5x cement paste, the free CA enzyme incorporated into the wet cement mix is still active after curing. After the application of only water, the calcium carbonate crystal growth on the surface of CA-Mod-5x suggests the potential for self-activated healing capabilities, that can repair large defects.

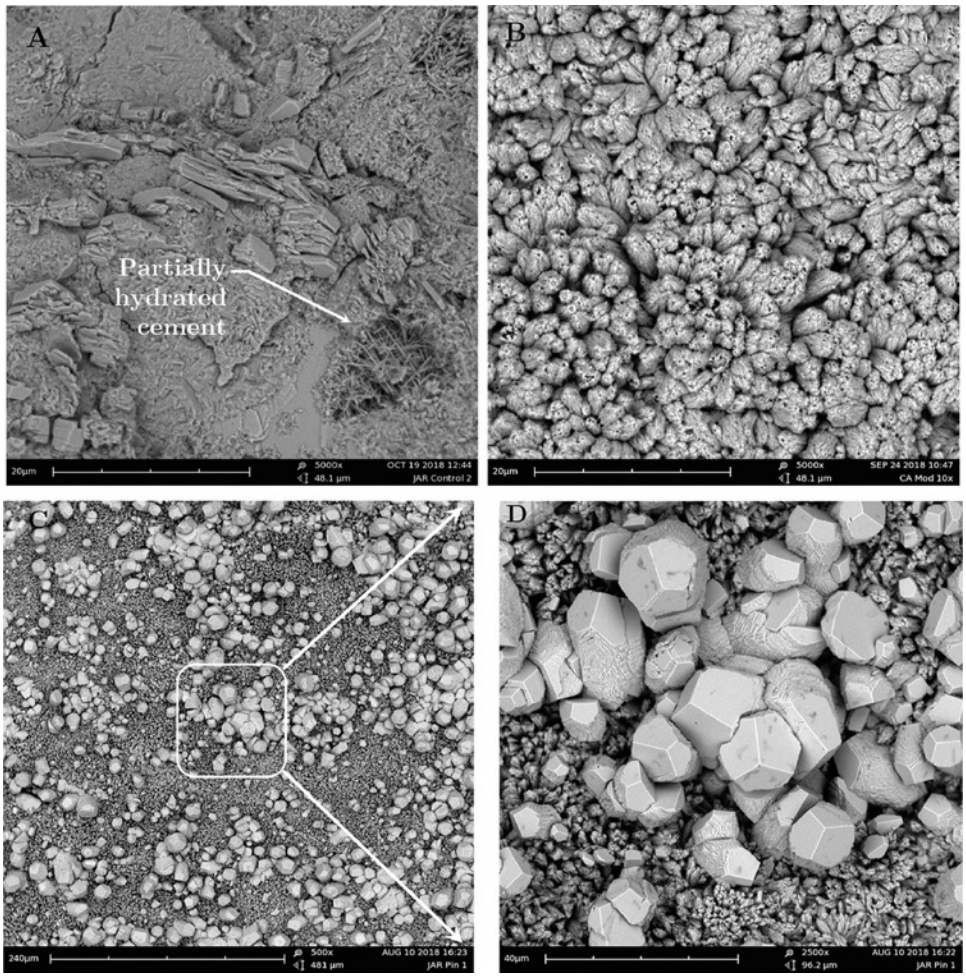

Figure 3-13 SEM images with scale bars of A) Partially hydrated cement needle-like particles are present in the control sample, 5000X; B) The cured surface of a CA-Mod-5x sample shows regular and even crystal formation, 5000X; C) Crystals develop on the surface of a CA-Mod-5x sample after soaking in DI water, 500X; D) A magnified view of the surface crystals on a CA-Mod-5x sample show evidence of cubic shapes and clustered formation, 2500X.

3.4.2 Compressive strength of self-healing concrete

It can be observed that CA-Mod-5x samples fully regains 97.5% compressive strength compared with control samples, clearly showing the regaining of the strength in enzyme-

modified cement paste samples with a millimeter-scale notch in 24 h, see Figure 3-13. Under the catalysis of carbonic anhydrase, a high concentration of bicarbonate ion was able to react with calcium rapidly on the sample surfaces. As it can be observed from the SEM images in , the self-activated healing process is accomplished through the fast growth of a dense formation of calcium carbonate crystals on the surface of the crack resulting in completely covering the notch and healing the sample in 24 h. The SEM images of the self-healed samples show that enzymatically catalyzed calcium carbonate crystals fill the cracks with solid crystalline precipitate, bringing compressive strength up to that of intact control specimens Figure 3-14. The increases in tensile strength and fracture toughness are also further proof that there is a bond between the crystals and the cementitious matrix. The current bacterial self-activated healing mechanism in cementitious matrices are not capable of recovering even micron-scale flaw sizes in a similar timeframe [73]. Figure 3-15 shows a close view of the morphology of calcium carbonate grow on the calcium silicate hydrate substrate. Here, we have clearly shown the full strength recovery of a self-activated healing sample in 24 h.

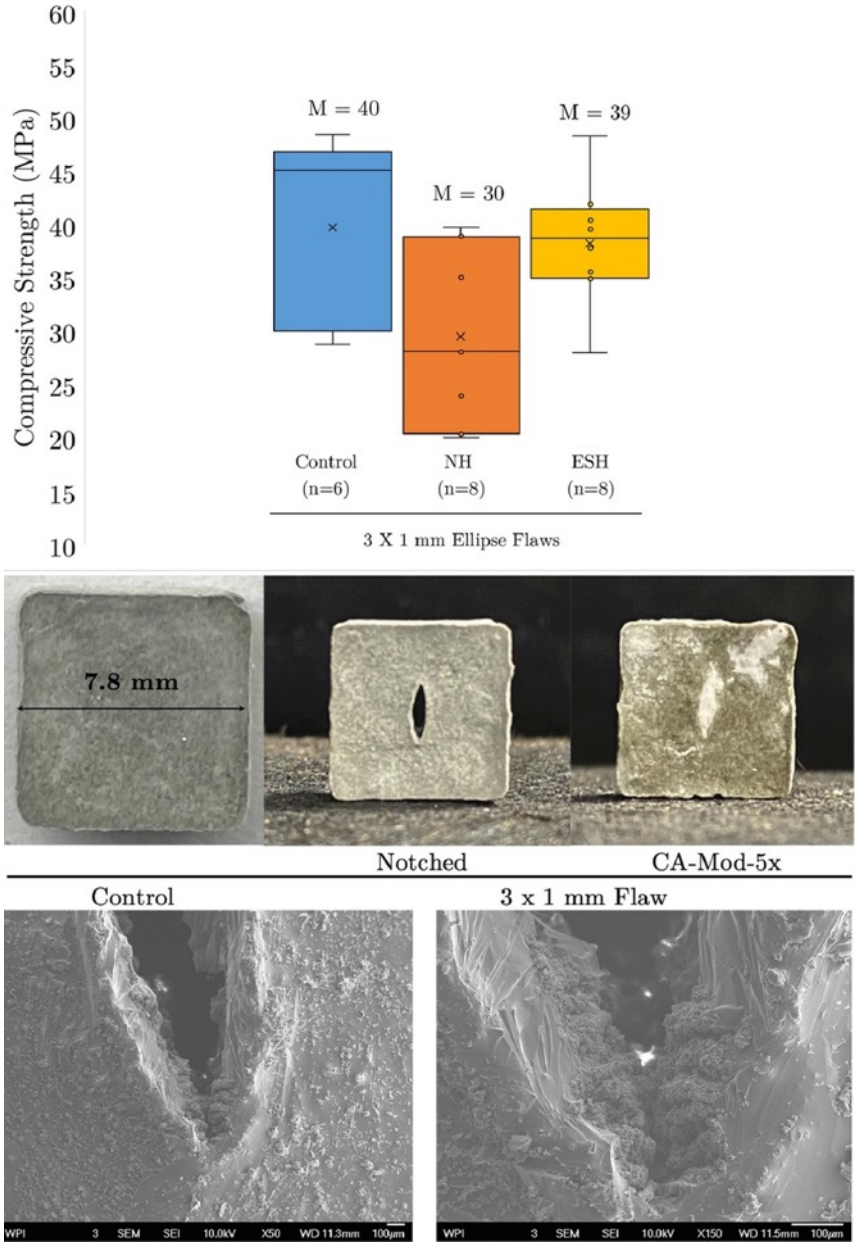

Figure 3-14 Compressive strength test results for control, notched, and CA-Mod-5x cement paste samples. Top: Comparison of compressive strengths of 7.8 mm square shaped samples. The mean for each data set is shown above. (Control: M = 40, SD = 8.06, n = 6; NH: M = 30, SD = 7.83, n = 8, p = 0.036; ESH: M = 39, SD = 5.52, n = 8, p = 0.696). The CA-Mod-5x samples with a 3x1 mm vertically oriented elliptical flaw obtain 97.5% strength, where the strength of notched samples reduced to 75% of the intact specimen. Middle from left to right: Control,

notched with a 12x3 mm flaw and CA-Mod-5x samples. Bottom: The SEM images shows the growth of crystal on the crack tip region.

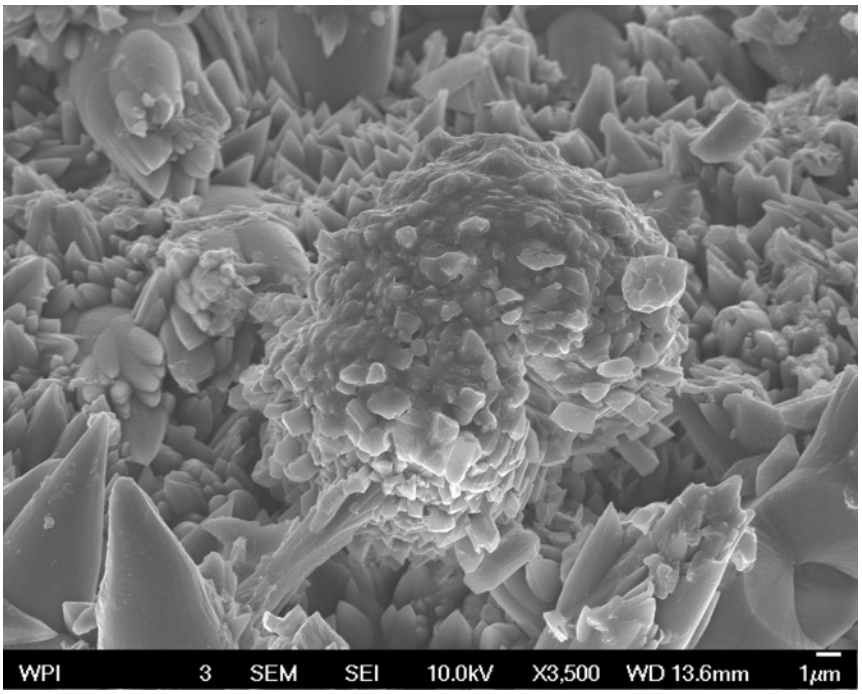

Figure 3-15 A close view of Calcium carbonate crystal growth from the cement substrate surface.

3.4.3 Compressive strength of Repaired concrete

In order to study the repair performance of the proposed mechanism on existing cementitious matrices, we also compared the mechanical properties of the flawed cube-shaped samples repaired in three ways: (1) enzyme repaired (ER) samples, (2) samples repaired with the control cement paste mix (CR), and (3) non-repaired samples (NR), compared to intact control cement paste (i.e. unfractured) samples to verify the proposed mechanism.

Cube-shaped specimens of cement paste were created for mechanical compressive testing, with two types of flaws. The control and flawed samples are shown (Figure 3-14 bottom) in the orientation used for compressive testing. The normalized values of compressive strengths with respect to the control are presented in Figure 3-16 top. The ER samples with a vertically oriented elliptical flaw (representing a macroscale crack) exhibit more than 100% strength of the undamaged control specimens, while CR samples have 80% strength, and the NR samples show about 83% strength of the undamaged control specimens. The ER samples with a 4-mm circular flaw have a compressive strength of 85% of the strength of the undamaged control specimens, while CR samples have 73% strength, and the NR samples exhibit 69% strength of the undamaged control specimens.

The results clearly show that cube-shaped samples with built-in flaws can regain their original compressive strength using a very small amount of enzyme, the calcium carboante is precipitated in a very short time period (4 minutes with the application of CO_2 fume). The large size of the repaired flaws (~10 mm) exhibits the astounding capability of the proposed method in the repair of cement paste samples. The literature does not describe any other biologic-based method that can fill such a large flaw size and with a material similar to cement paste in thermomechanical properties.

The samples with large circular or elliptical flaws almost fully regain their original strength after the application of the CA enzyme. The regaining of the strength in the case of the cement paste samples with large elliptical holes (size 12 mm tall × 3 mm wide and extending through the cube sample the entire 25 mm length, representing a large crack) is slightly lower than the sample with a circular hole (4 mm diameter and extending through the cube sample the entire 25 mm length). Specimens geometries are shown in Figure 3-8. This is essentially due to

the statistical nature of brittle fracture and the relatively larger size of the cracks in these samples comparing to the size of the samples. Overall, these studies show our repair method can regain the mechanical properties of cement paste samples with different large size flaw geometries. We note that all previous work using alternate methods has only focused on regaining the compressive strength and establishing water-tightness, but used with significantly smaller flaw sizes over a much longer period.

The results of the compression testing for cured enzyme-modified mix samples over 7-day, 14-day, and 28-day curing periods are studied and there is little to no change from 7-days to 14-days to 28-days for control cement paste sample strengths, see Figure 3-16. A Student's *t*-test was conducted to compare the CA-mod-5x samples' compressive strength values against the control samples, see Table 3-2. The CA-treated samples show significant differences from control at 7-days by an average of 7 MPa. However, at 14-days, the strength of the CA samples is stronger by at least 5 MPa. At 28-days, the Control and CA data averages are within error. There is an average 14 and 20 MPa increase in strength from 7 days to 14 days for all enzyme-repaired samples at three enzyme concentration strengths, and an average increase of 10 MPa from 7 days to 28 days. These results suggest that the amount of CA enzyme in the CA-Mod 5x mix is a good starting point to fine-tune the enzyme to cement paste ratio for optimization.

Table 3-2 Compressive strength data for enzyme modified cement paste mix designs evaluated at the standard age intervals of 7 days, 14 days, and 28 days after casting.

Type	Age at testing	Number	Compressive strength (MPa)	Standard deviation	Standard error	95% confidence interval
Control	7 d	26	43	6.6	1.3	± 2.7 (41, 46)
	14 d	14	43	7.0	1.9	± 4.0 (39, 47)
	28 d	15	45	5.8	1.5	± 3.2 (42, 48)
CA-Mod-1x	7 d	9	36	6.5	2.2	± 5.0 (31, 41)
	14 d	9	46	4.4	1.5	± 3.4 (43, 50)
	28 d	10	39	14.2	4.5	± 10.2 (28, 49)
CA-Mod-5x	7 d	10	31	6.0	1.9	± 4.3 (26, 35)
	14 d	10	49	4.2	1.3	± 3.0 (46, 52)
	28 d	9	46	5.8	1.9	± 4.4 (42, 51)
CA-Mod-10x	7 d	9	36	8.1	2.7	± 6.2 (30, 42)
	14 d	9	47	3.3	1.1	± 2.6 (45, 50)
	28 d	10	47	4.8	1.5	± 3.4 (43, 50)

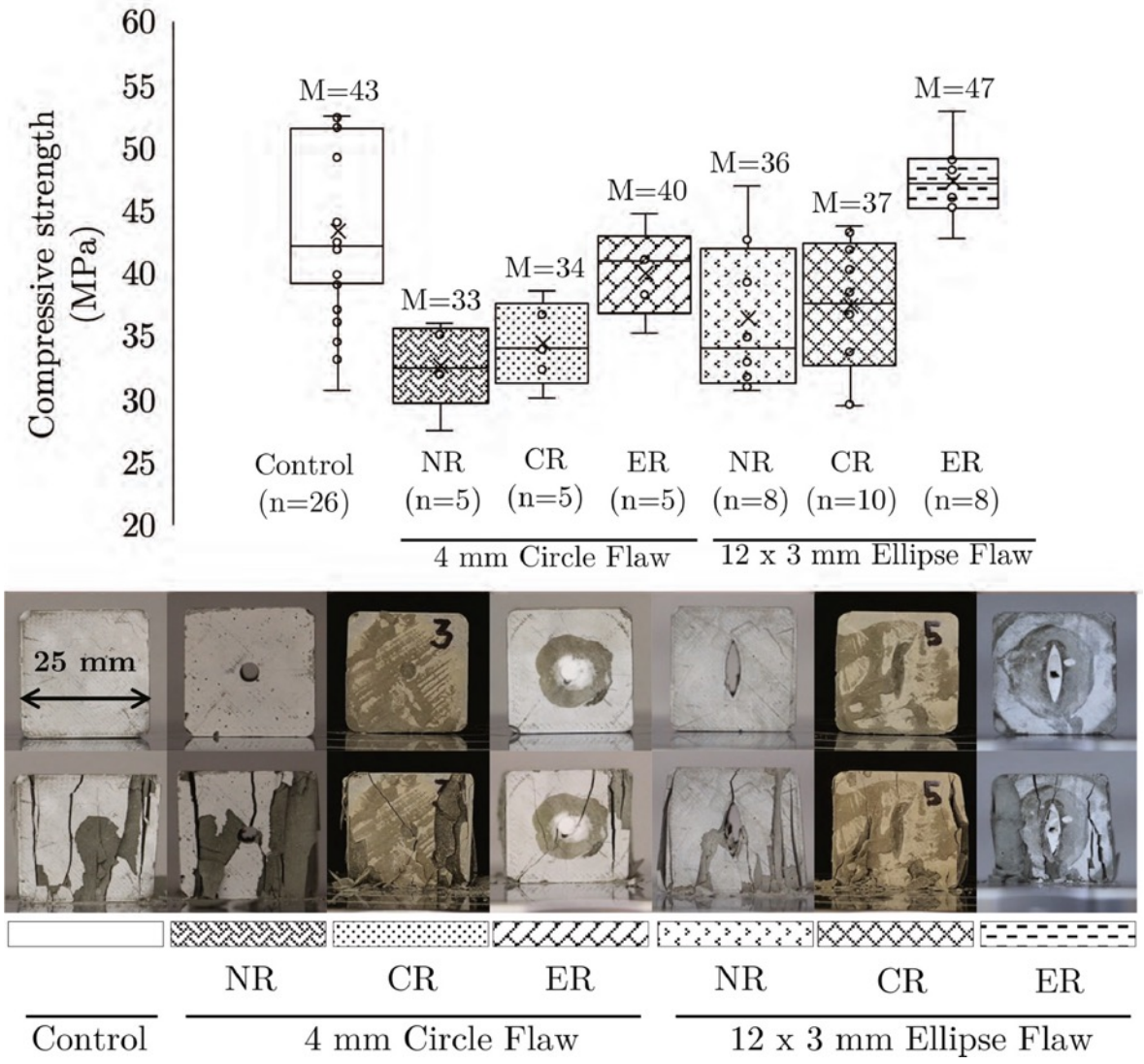

Figure 3-16 Compressive strength test results for control, NR, CR and ER repaired cubes, with means shown above each data set and pictures of samples during and after testing. Top, from left to right) Control samples show a mean 43 MPa compressive strength. For samples with a 4 mm circular flaw, NR samples show 75% strength of intact control, CR samples obtain 80% strength, while ER samples obtain a high 93% strength (statistical significance vs. control: Control: M=43.4, SD=6.6; 4mm-NR M=32.4, SD=3.5, t=3.895, p=0.002; 4mm-CR: M=34.4, SD=3.6, t=3.188, p=0.014; 4mm-ER: M=40.0, SD=3.7, t=1.210, p=0.413). For sample with a 12×3 mm vertically oriented elliptical flaw, NR samples obtain 84% strength of intact control, CR samples obtain 88% strength, while ER samples obtain an impressive 108% strength (statistical significance vs. control: Control: M=43.4, SD=6.6; 12 × 3-NR: M=36.4, SD=6.0, t=2.988, p=0.018; 12 × 3-CR: M=37.6, SD=5.0, t=2.682, p=0.030; 12x3-ER M=47.3, SD=3.2, t=1.622, p=0.210). Bottom, from left to right) Images of samples before compression experiment in the top row, and fractured samples after the tests on the

bottom row: Control sample; 4 mm circular flaw NR, CR, and ER; and 12 × 3 mm flaw NR, CR, and ER.

3.4.4 Real scale concrete repaired by Carbonic anhydrase

a) 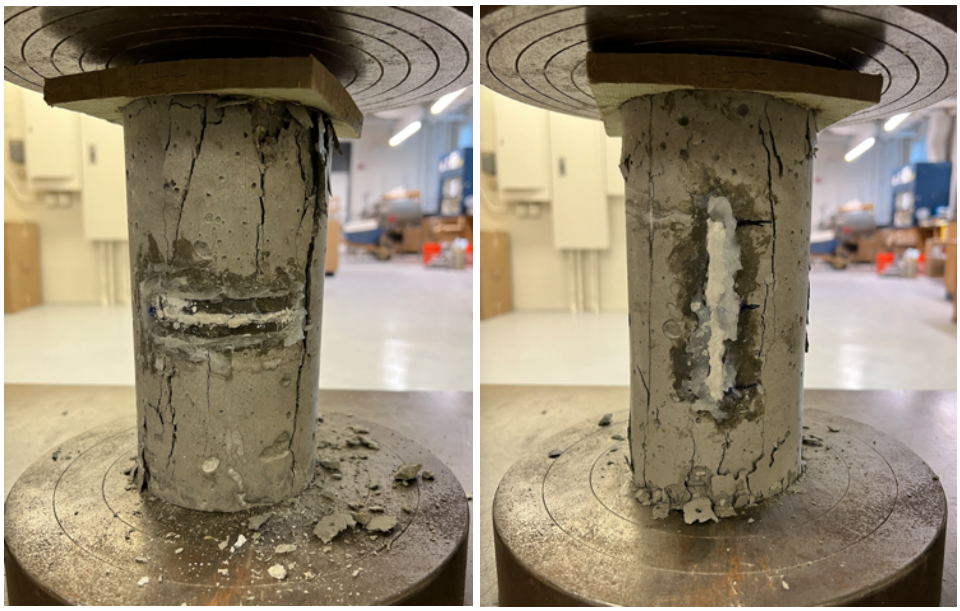

b) 

c) 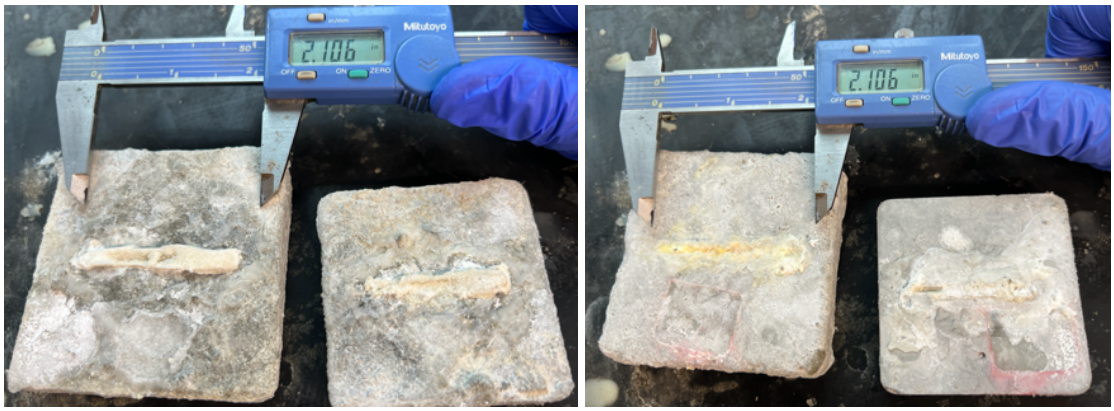

d) 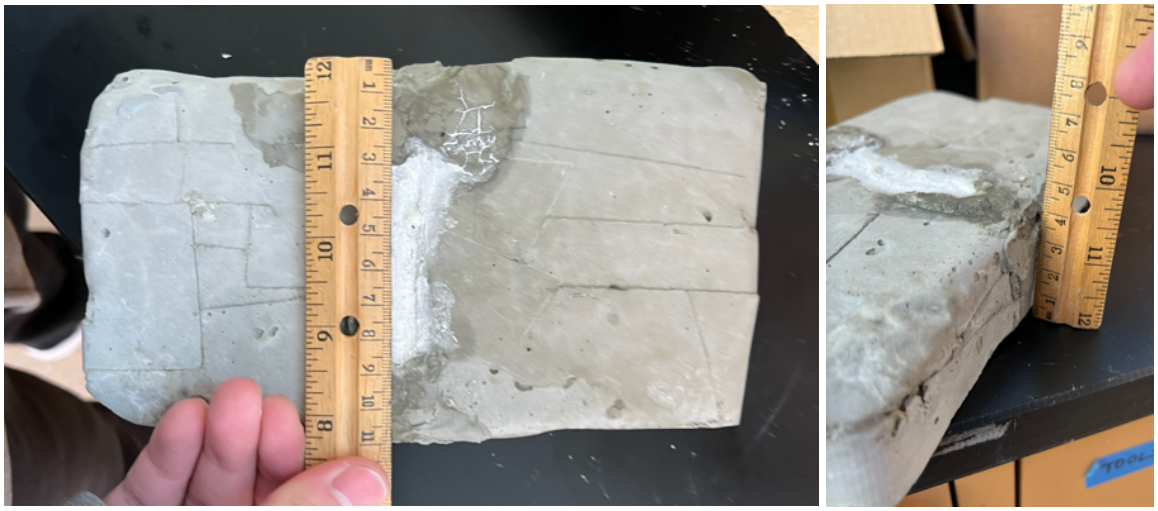

Figure 3-17 a) Carbonic anhydrase repaired lateral direction and axial direction notch (2 in arc length) in 4x8 in cylinder concrete. b) Gelatin served as substrate and filled in the penetrated notch of concrete. c) Carbonic anhydrase repaired prenerated notch (2.1x0.2x0.5 in) of cement paste in front (left) and back (right) side. d) Carbonic anhydrase repaired large scale penerated notch (2.1x0.5x1.6 in) of concrete.

Repair of small cracks and fractures of small cement samples bathed in a carbonic anhydrase enzyme solution (CA) has been described in a US patent [61]. In situations where the CA repair solution must be applied to crack on a surface where immersion is not practical, the repair solution will flow through the material becoming dilute and not accelerating repair. By

incorporating CA onto a substrate, such as a silicon bead, or in a solvent that does not allow fast diffusive flow through the concrete, such as hydrogel, accelerated repair can occur.

Carbonic Anhydrase from bovine erythrocytes was purchased from Sigma Aldrich (30 kDa) 2.9 mg enzyme was dissolved in 1 mL deionized water, aliquoted and stored at freezer until use.

Thin cement paste slabs were manufactured in a similar manner to the cement paste slab. Silicone molds were made from 3D printed parts to create 30cmx15cm slabs with 6 cm thick. Each slab was manufactured with an 8cm length x 0.5cm width x 6cm depth notch at the concrete center. The concrete slab was mixed with all-purpose gravel and sand followed with ASTM C33 [74] specifications and the ratio of material components following (cement: sand: gravel: water = 1:1.45:1.91:0.467).

The enzyme product was precipitated from a 49.6: 49.6: 0.74: 0.0003 volume percent solution of four parts in a beaker on a stir plate: 200 mL of 2M calcium chloride dihydrate, 200 mL of 0.1M Tris base, ultrapure water, and a 15 uL aliquot of 20 mM (dissolute from 0.2 mL of 2.9 mg/mL CA) bovine CA. Thus, the amount of CA used was very small.

The same method was used to prepare the enzyme calcite solution. The solution was left to stand for 24 hours and then remove the supernatant. The enzyme calcite solution was well stirred for two minutes and the 20 mL siphoned solution was to heat up to 35℃. 1g of gelatin (Knox) was mixed with the 20 ml solution for two minutes and make sure all gelatin is dissolved in the solution (the ratio of gelatin solution needs to be adjusted depending on the dimension of the notch). The prepared concrete slab was placed in two stands so that the notch is suspended. 10 mL enzyme calcite solution with gelatin was filled in the notch evenly and make sure all solution covers the notch. Air drying for 24 hours then filling the rest of the 10 ml solution in the

notch, see Figure 3-17 b. During this process, the gel-calcite solution sealed the notch to keep fresh calcite solution in the notch. After 24 hours of air drying, start filling up the enzymatic calcite solution in the sample notch. Inspection was made to see if any solution leakage from the bottom occurred after filling. Then further air drying too place for an additional 24 hours; the enzyme calcite solution was again filled up and the process repeated for 5 days. Finally, the notch was thoroughly repaired after air drying, see Figure 3-17 c & d.

3.4.5 Concrete chloride ion permeability by RCPT

The preliminary results are presented in Figure 3-19 a. The results show that permeability of control mix designs is ranked as high, and that of CA-28d is moderate. However, the results of RCPT are not representative and can only be used as an assistant for permeability analysis because the solution temperature rises to 60 ℃ during the operation of the experimental apparatus, which can physically and chemically alter the solution inside of the concrete pores. On the other hand, RCPT is complex in terms of sample preparation requirements to ensure that the surfaces of the cutting samples are parallel each other and that there are no defects on the sample surface. In Figure 3-19 b, the chloride ions permeability of different curing days for CA and control samples are presented. During the test, the permeability coefficients of the samples decreased with the curing day increase and all of CA modified concrete samples at 7, 14, and days show a lower permeability than control samples.

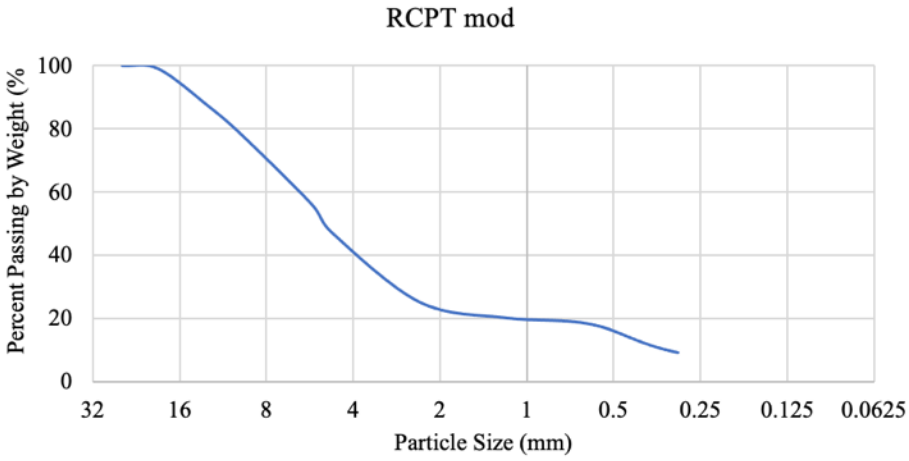

Figure 3-18 Aggregate gradient distribution for Rapid Chloride permeability test (RCPT) sample.

a)

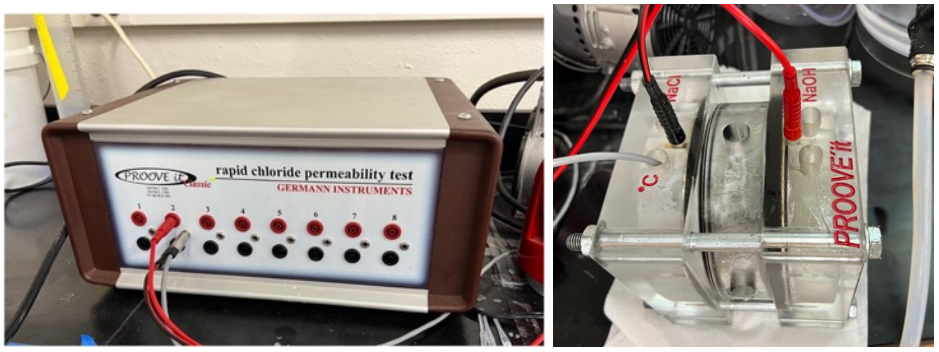

b)

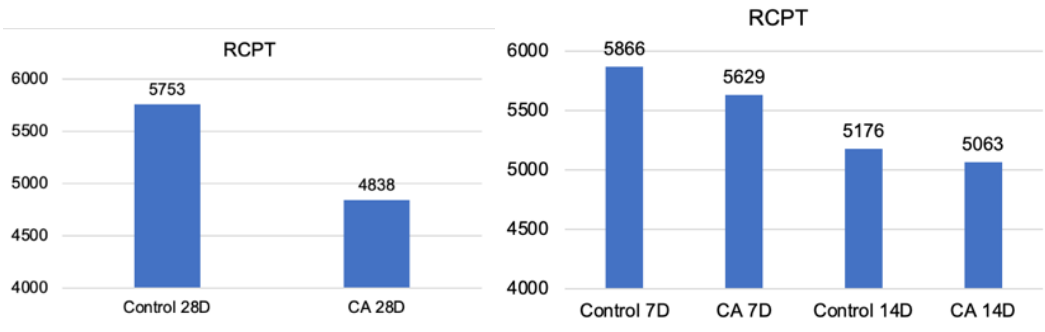

Figure 3-19 a) The rapid chloride penetrability test data logger (records charge passed) and sample cell, b) recording the charge passed (coulombs) on carbonic anhydrase modified portland cement concrete samples at different curing days.

3.4.6 Accelerated vacuum test

The concrete cement samples were cast in cylinder molds of 50mm by height X 100mm by diameter. Then, a curved watch glass (beaker cover) was pressed into the top of the samples, convex side down. This produced a concave top on each cylinder sample, in effect creating a depression to retain water. After curing in a steam room for required days, a silicone ring was placed around the top of the sample. This process is to create a larger space to hold more water than the concave top in the concrete cylinders. Cured cylinders were than dried at room temperature for three days to remove moisture from the sample pores. Then 10 mL of a 10,000-ppm fluorescent red dye was pipetted into the convex top, then the samples placed in a glass vacuum chamber, and pumped for 10 minutes. The chamber was sealed, and vacuum maintained for 24 hours. The next day the pump was run for anther 10 minutes, the chamber re-sealed, and this process repeated for three days. On the fourth day, it was observed that the 10 mL of dyed water had completely adsorbed into the cylinders. After three days drying, the cylinders were conducted the splitting test following the standard ASTM C496 [75]. After test, the inner penetration of the dye was observed under ultraviolet light. Figure 3-20 shows a comparison of 28 curing days cement between CA modification and control, the control sample without CA treatment exhibits a deeper dye penetration of around 14.6 mm, three times larger than the CA-modified cement sample. The slit tensile test results were presented in Figure 3-21, showing a higher splitting tensile strength on both 14- & 28-days CA modified cement. The inclusion of CA in cement possibly enhances the bond strength of calcite silicate hydrate (CSH) gel.

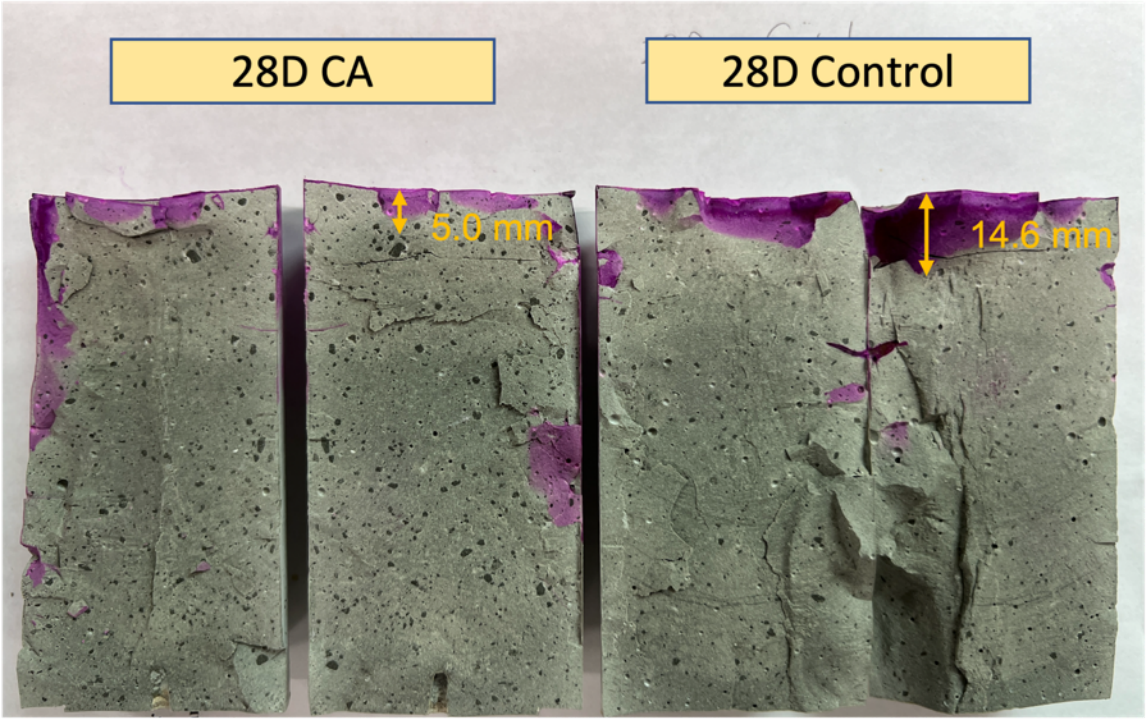

Figure 3-20 The dye penetration test of carbonic anhydrase modified cement sample compares with plain cement sample.

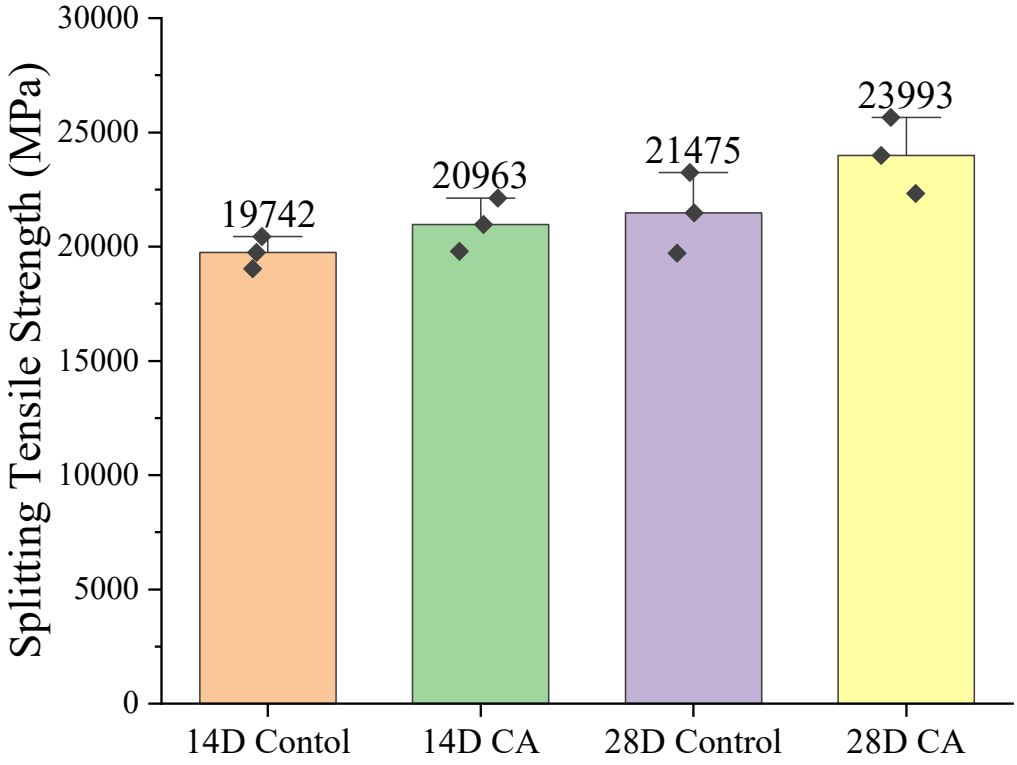

Figure 3-21 The splitting tensile strength of carbonic anhydrase modified cement sample in different curing periods.

3.4.7 Accelerated corrosion test (ACT)

Figure 3-23 shows the ACT results for rebar reinforced concrete samples cured in 7-, 14-, 28-, 48- and 64- days. Once a sharp increase in voltage (indicating the initiation of corrosion) was observed, the test was immediately terminated. The results show that CA greatly extends the time before cracks are initiated showing a significant protection against corrosion in every single curing group. Based on our previous studies, the mechanism underlying this protection is the formation of calcium carbonate crystals in the voids of cement matrix which causes an increase

in the resistance of the concrete matrix. The electric current is decreased for a given applied voltage.

Another benefit is that when crystals are grown in the cement matrix it can enhance the concrete compressive strength and would not prevent the second hydration of the cement. The present of crystals increase the concrete crack tip opening displacement where increase the properties of inherent interface.

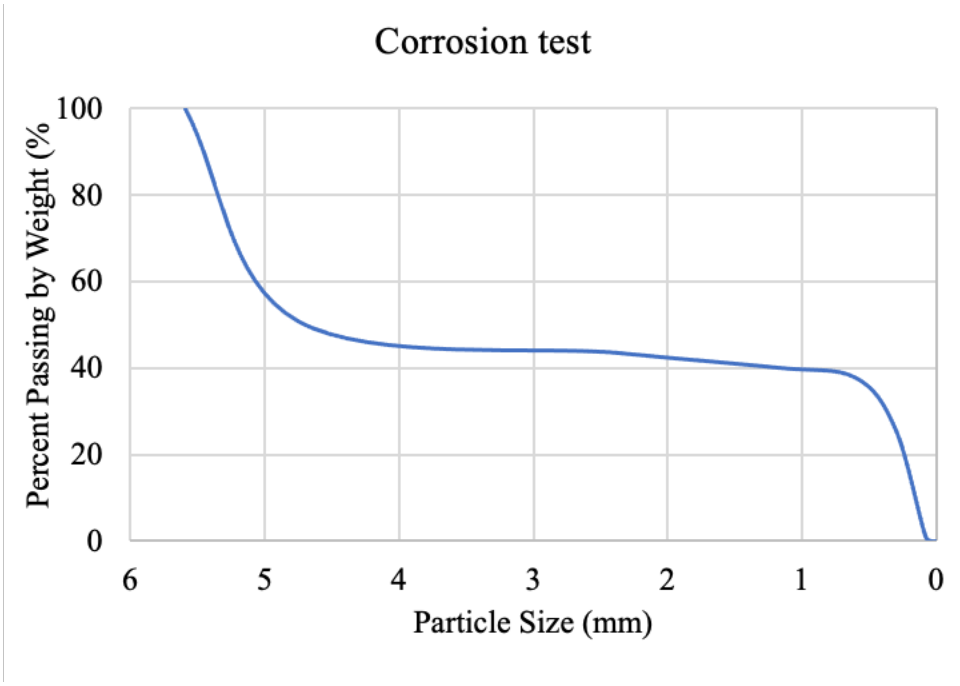

Figure 3-22 Aggregate gradient distribution for accelerated corrosion test samples.

a)

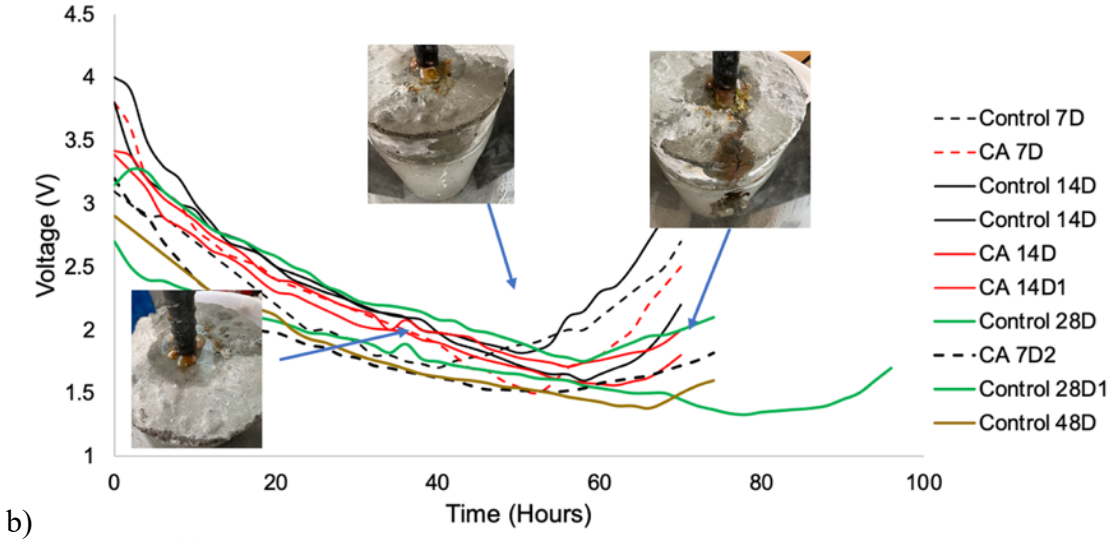
Voltage (V)
4.5
4
3.5
3
2.5
2
1.5
1
0
20
40
60
80
100
Time (Hours)
Control 7D
CA 7D
Control 14D
Control 14D
CA 14D
CA 14D1
Control 28D
CA 7D2
Control 28D1
Control 48D

b)

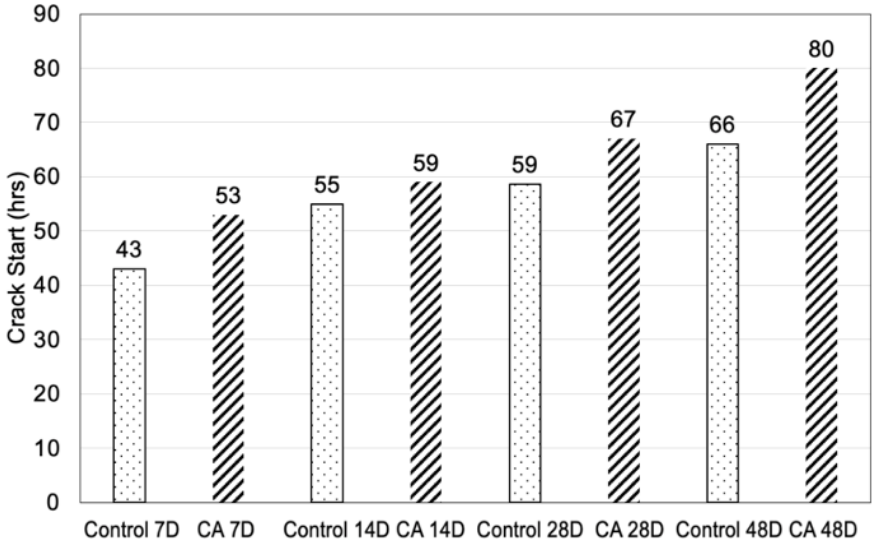
Crack Start (hrs)
90
80
70
60
50
40
30
20
10
0
43
53
55
59
59
67
66
80
Control 7D
CA 7D
Control 14D
CA 14D
Control 28D
CA 28D
Control 48D
CA 48D

c)

Figure 3-23 a) A typical Accelerated Corrosion Test setup, b) Fracture initiation data on 7-, 14-, 28-, 48-day samples with enzyme (1g cement/1μl enzyme). Before the samples crack, the brown color liquid bleeds from the interface between the top of the cylinder and rebar, and the crack starts from the axial edge of concrete indicated by the deflection point where the voltage starts to increase, after the samples entirely fail. c) The comparison of time of the initial crack between CA modified and control samples under same voltage. It can be observed that fracture in all samples occur later than in the control samples.

3.4.8 Enzyme repaired flawed cement cube

All samples were designed with a consistent water:cement ratio of ~0.5. Two different mixes were prepared with elliptical flawed and flawless cubes in six groups. The samples were cured in a controlled environment steam room at 100% humidity and within a temperature range of 20–25 ℃ and stored there until repairing. After the samples have cured for an appropriate amount of time, the silicone funnels were attached, and a second water-tight seal was created between the bottom of the cement samples and an acrylic sheet. These sealed samples were cured for about 24 hours. The repair agent followed a water-cement ratio of ~0.8 to improve the workability and this facilitated repair without the use of admixtures or superplasticizer, which could have an adverse chemical interaction that could alter the activity of the enzyme catalysis. The elliptical flaws were repaired by cement or cement with CA (cement: CA = 1g:1ul) on the vibrated table for ten minutes, and then return to steam room for further curing. The sample after compression test was presented in Figure 3-24. And the compressive strength of all repaired cement samples was presented in Figure 3-25. The CACA (CA modified cement repair CA cement cube) outperform other groups of samples and comparable to the CA cube (CA modified

cube). All groups of samples with CA showing a higher compressive strength than the samples without either CA repairment or CA modification. This is because the inclusion of the CA accelerates the calcite crystals growth in the cementitious matrix, which increases the strength of the structure.

Figure 3-24 The sample of carbonic anhydrase modified cement repaired carbonic anhydrase modified cement cube.

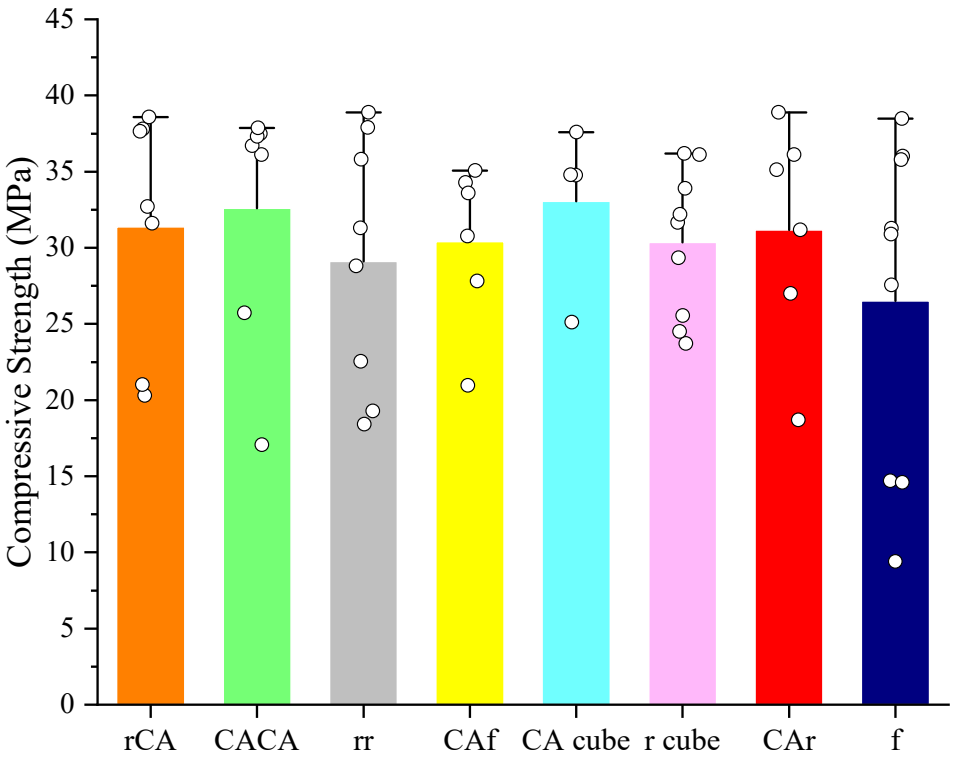

Figure 3-25 The effect of compressive strength for carbonic anhydrase modified cement repaired cement with build in flaw. Here, rCA (cement repair CA modified cement), CACA (CA modified cement repair CA modified cement), rr (cement repair cement), CAf (CA modified cement with flaw), CA cube (CA modified cement cube), r cube (cement repair cement), CAr (CA modified cement repair cement), f (cement with flaw).

3.5 Summary and Conclusion

This work establishes a new paradigm for an enzyme-enhanced self-activated healing mechanism in cement paste structures, where compression is the essential function of the cement paste matrix. The efficiency of the enzymatic method in comparison with MICP is more than two orders of magnitude, which leads to the healing of significantly larger cracks in two orders of magnitude shorter time-scale. We show that the CA enzyme is still viable after several weeks of

curing through pH monitoring of samples, and methods to increase its longevity are presently being pursued as future work. Finally, the impact of this work goes beyond repairing cement paste. This potential for a self-activated healing cement paste mix using the CA enzyme has created a firm foundation upon which to build future self-healing ceramics systems requiring large and rapid production of crystals for repair. In summary, inspired by the evolutionary optimized biological process of CO_2 transport in biological cells by the CA enzyme, this study shows the remarkable capability of the CA enzyme in catalyzing the precipitation of calcium carbonate crystals to create self-healing cementitious matrices.

Chapter 4

Chapter information: Shuai Wang, Suzanne F. Scarlata, Nima Rahbar, A self-healing enzymatic construction material, Matter, Volume 5, Issue 3, 2022, Pages 957-974, ISSN 2590-2385, https://doi.org/10.1016/j.matt.2021.12.020.

4 Enzymatic Construction Material (ECM)

4.1 Abstract

Concrete is one of the main contributors to global CO_2 emission, and efforts to find an alternative to concrete have not been fully successful. Inspired by the process of CO_2 exchange in biological cells, this paper introduces a novel method to create a negative-emission enzymatic construction material (ECM) with self-healing capabilities. The concept proposed in this paper uses carbonic anhydrase (CA) to catalyze the reaction of CO_2 and water to produce bicarbonate and promote the precipitation of calcium ions in the aqueous solution as calcium carbonate crystals. The resulting ECM has compressive strength and Young's modulus more than twice that of the minimum accept- able for cement mortar and other alternative building materials. The strengthening mechanism through the growth of mineral bridges that hold the sand particles in the structure of ECM is also modeled and studied. This report provides a new path for development of environmentally friendly construction materials with low cost.

Keywords: enzyme; carbonic anhydrase; self-healing; construction materials; carbon negative; crystal growth; concrete alternative

4.2 Introduction

Second only to water, concrete is the most consumed material on earth, with three tons per year used for every person [74]. Every year, waste concrete from construction and CO_2 emissions from cement production and transport increase, and concrete alone now contributes to

9% of total CO_2 emissions [77]. Climate change caused by increased CO_2 levels due to human activity is the biggest existential threat facing the world. Therefore, reducing CO_2 emissions to reduce the greenhouse effect and the rise in the earth's temperature is an urgent task. To help alleviate the above-named problems, researchers have previously applied biological methods to repair concrete through calcite deposition [78, 79].

Inspired by the process of CO_2 exchange in cells, we have previously proposed a novel mechanism of using enzymes to rapidly repair damaged concrete and create a self-healing cementitious matrix [80]. Natural enzymes are proteins that catalyze a chemical reaction rapidly without being consumed in the process and are inherently safe and reliable [81]. Carbonic anhydrase (CA) is a fundamental enzyme found across all species. Fourteen isoenzymes of CA have been found in the human body, and these variants have slightly different structures and properties that optimize their activity in different tissues. All CA enzymes play the same critical physiological functions in cell respiration by reacting CO_2 with water to yield carbonic acid in the body tissue and reversing this reaction in the lungs to generate CO_2. Hence, in non-biological systems, CA can be used to induce calcite precipitation [82]. Keeping in mind that the sequestration of CO_2 is based on chemical fixation of carbonate minerals such as calcite, aragonite, and magnesite, we propose a biomimetic CO_2 absorption mechanism using biocatalysts such as CA to reduce local CO_2 concentrations emitted from the production of cement [83].

Despite progress in developing functional concrete, such as the use of enzyme-catalyzed calcite precipitation to repair concrete, the preparation of self-healing concrete containing bacteria, or self-healing concrete containing a capsule system, production of concrete cement generates CO_2. To fundamentally solve the CO_2 emission problem of concrete production, a

viable substitute material for cement needs to be discovered. On the basis of the technique of microbially induced calcite precipitation (MICP) previously investigated and applied on self-healing concrete mortar [84], Srubar et al. incubated Synechococcus from a photosynthetic cyanobacterium in MICP to develop long-term-viability building materials (LBM), which enables successive regenerative ability [85]. However, the mechanical properties of LBM compared with standard cement mortar are not improved, and this material is not yet able to be used for practical construction applications. Additionally, the mechanism of crystal precipitation and growth within the bio-scaffold of LBM is inefficient, resulting in a material with low density whose maximum strength is about 3.5 MPa.

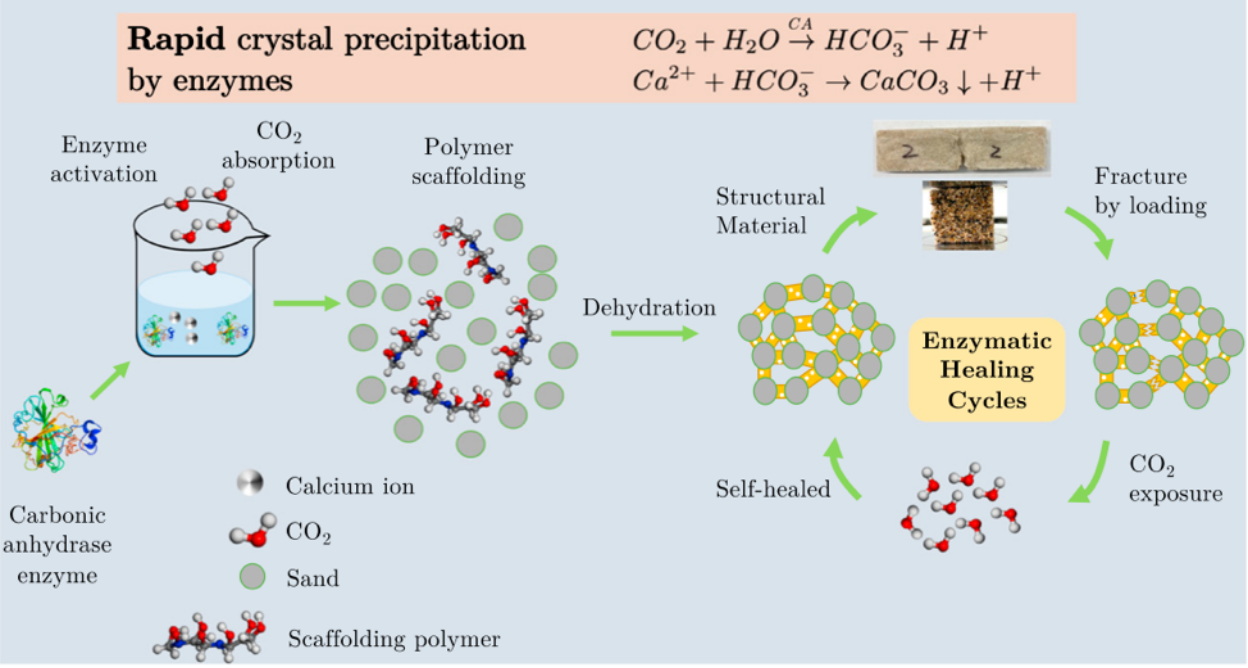

Figure 4-1 Schematic diagram showing the construction process of ECM and its mechanism for sustainable self healing behavior by carbon dioxide exposure.

Here, we report on the development of self-healing construction material using sand aggregates, a trace amount of CA, a small dose of scaffolding material with a crosslinking agent,

and a calcium source, the principle and experiment is presented in Figure 4-1. This material is twice as strong as LBM and needs only 24 h until maximum strength is achieved compared with LBM, which requires 7 days, and regular cementitious concrete, which requires 28 days. Curing of the material can be performed at a high temperature in a short period or at room temperature for a more extended period. This enzyme-driven method bridges the sand particles and results in a dense, stiff, strong, and relatively tough structural material that can heal itself repeatedly upon exposure to a calcium source and CO_2. Two fabricated ECM products are shown in Figure 4-2.

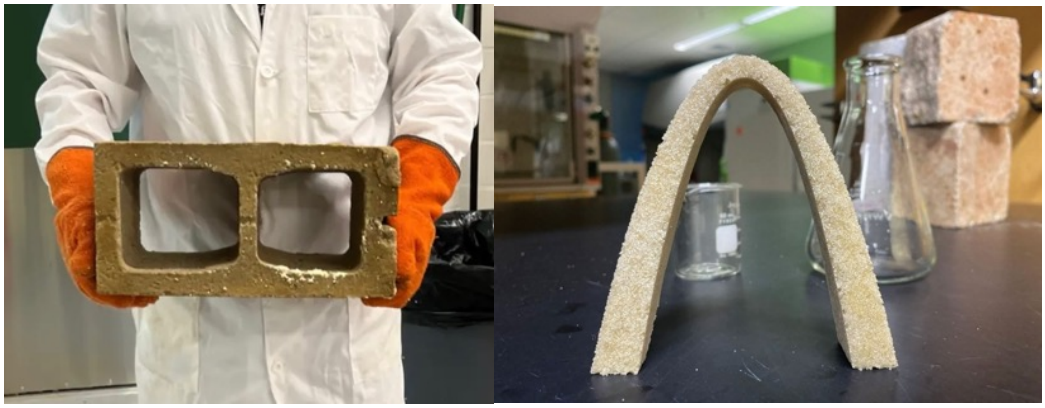

Figure 4-2 Two exhibits of ECM: ECM standard cinder block (20 x 20 x 40 cm) and St. Louis arch (height in 15 cm).

4.3 Materials and methods

Table 4-1. The compositions of solutions.

Name	Enzyme	Base	Gelatin	Calcium	Sand
Ca				√	
BCa		√		√	
BEC	√	√		√	
ECA	√			√	

Table 4-2. The compositions of sand slurry samples.

Name	Enzyme	Base	Gelatin	Calcium	Sand
ECa	√			√	√
GCa			√	√	√
BGC		√	√	√	√
BGE	√	√	√	√	√
ECM	√		√	√	√

4.3.1 Enzymatic solution preparation

The analytical grade carbonic anhydrase (CA), calcium chloride dihydrate, and tris (hydroxymethyl) aminomethane (THAM) were obtained from Sigma-Aldrich Chemical Company. To prepare enzyme matrix solution, 2.9 mg of CA and 1 mL of deionized water were mixed into aliquots and then shaken evenly in the horizontal direction for 2 min Five microliters of 100 mM CA solution was pipetted to each of the empty aliquots and then stored in the freezer.

4.3.2 Calcite solution preparation

To prepare a buffer solution, 0.1 M Tris (ordered from Sigma-Aldrich) was added to 200 mL of deionized water and stirred on the magnetic stirrer for 2 min. Then, 10 mL of 100 mM CA solution was added into buffer solution and stirred for another 2 min 2 M calcium chloride dihydrate-saturated solution was prepared on the stirring hot plates at 35 ℃, at 600 rpm for 2 min. Here, calcium chloride dihydrate was chosen as the calcium source because it can generate calcite more efficiently [86]. This is because the calcium ions must first combine with carbonate ions in solution to form calcium carbonate and high concentration of free calcium ions in the solution expedites the dissolution of calcium chloride dihydrate. When the calcium chloride dihydrate was dissolved substantially, mixing with buffer solution for an additional 2 min. CO_2 gas was then introduced into the solution at a rate of 5 bubbles per second for 10 min and stirred

throughout the process at 250 rpm. A pH electrode was immersed in the solution to record the entire process. It can be observed that some white fog was produced from the solution after 5 min. The experiment was ended at 15 min, and the flow of CO_2 gas was stopped. The solution was then settled for 4 h, and the supernatant was siphoned to prepare a highly concentrated calcite solution. To prepare the solution for the high-pH condition samples (BGE and BGC), the base chemical (sodium hydroxide) was added to the buffer solution (0.4% w/v) at the beginning of the experiment and mixed thoroughly until sodium hydroxide particles dissolved completely.

4.3.3 Weigh gain experiment

Four groups of solutions were prepared (Ca: Ca^{2+}; BCa: Base + Ca^{2+}; BEC: Base + CA + Ca^{2+}; ECA: CA + Ca^{2+}) similar to the method described in the 4.3.1 Enzymatic solution preparation section. Each solution was weighed out before precipitation started. The solution was then aerated with ultra-pure CO_2 gas (5 bubbles per second in constant flow rate) for 10 min and stirred throughout the entire process. The weight of the solution was measured again immediately after the end of the experiment prior to any significant water evaporation. A checklist table of compositions of solutions is presented in Table 4-1.

4.3.4 Cubic and cuboid ECM sample fabrication

All specimens were prepared using the same materials and geometry. This level of consistency in experimental design and specimen preparation provided a solid basis for later comparison of different types of material combinations. #No. 50 grade (retained on a 300-mm sieve) white sand was dried in an 80 ℃ oven for 24 h then cooling to 35 ℃ before using. Gelatin (10% by weight, Knox) (gelatin/solution) was mixed with sand for 2 min. The amount of calcite

solution and sand follows the ratio of (0.3 v/w). Gelatin was chosen because of its chemical compatibility with CA, since the completely soluble temperature of gelatin is 35 ℃, which is within the temperature range of CA activity. The sand-gelatin mixture was placed in 3D printing silicone molds (cubic, cuboid, and pre-notched cuboid). The calcite solution was then titrated on the surface of the sample. Please note that the matrix of sample ECa did not mix with the gelatin. The samples were allowed to settle for half an hour until the solution was completely saturated in the matrix. The ECM samples were finally desiccated in a 100 ℃ oven for 24 h and removed from the mold for mechanical testing. Samples (25 mm^3) were prepared for uniaxial compressive tests. A loading rate of 1.27 mm/s was chosen here. The single-edge notch beams were prepared for fracture and self-healing experiments, and the plain beams were prepared for the bending test. A checklist table of compositions of sand slurry samples is presented in Table 4-2.

4.3.5 X-ray diffraction and Fourier transform infrared spectroscopy analysis

To confirm chemical composition and crystallinity of the crystals, we analyzed the dried enzyme solution product by powder X-ray diffraction (pXRD) and Fourier Transform Infrared Spectroscopy (FT-IR). pXRD was performed on a Bruker AXS D8 Focus (Bruker, Billerica, MA, 102 of 190 USA) at 25℃, and the pXRD spectrum used a CuKa radiation source at 40 keV and 40 mA from 20° to 90° of 2θ with a step size of 0.100°, against baseline. FT-IR was carried out on a Bruker Optics Vertex 70 equipped with a Specac Golden Gate Diamond Single Reflection ATR element (Bruker, Billerica, MA, USA).

4.3.6 Crystal growth investigation

Experiment procedures

The well mixed sand and gelatin mixture were stabilized on the glass slide by placing the glass slide in a conical flask with a single stopper hole, covering a single hole rubber stopper on the flask head and inserting a tube capable of introducing carbon dioxide. The tube is close (~10 cm) to the sample surface to allow gentle introduction of carbon dioxide. CO_2 was stopped at 5, 10 and 20 minutes to record the process. Note that when material is in the gel state the in-situ measurement of the bridge sizes is difficult. For better observation of the crystal growth process, samples were dehydrated and imaged by SEM and optical microscopes. The same volume of calcium solution was added to the sample at 5 and 10 minutes because the sample has already been desiccated for imaging.

Crystal bridge growth model

In an oversaturated calcium chloride solution, gelatin scaffold serves as the site that provides a stable platform for calcite crystal nucleation and growth. The calcium carbonate then continues to precipitate around bridges causes the surrounding concentration of calcium carbonate to be lower than the entire aqueous system.

The solute $CaCO_3$ that precipitates at the gelatin surface is denoted here as C_R. The molar concentration of crystals in the solid mineral is represented by C_r. The molar concentration of $CaCO_3$ in the solution around the solid mineral is denoted as C_0. This latter variable is very low because the solubility of calcium carbonate is only 13 milligrams per liter [87]. The solute ions of $CaCO_3$ around the solid mineral are adsorbed and precipitated, which result in a low concentration (C_0) of $CaCO_3$ but above saturation. The distant $CaCO_3$ solutes diffuse to the surrounding of the mineral bridge, thus continuing the growth of the mineral crystals. The concentration profile is shown in Figure 4-3 left. Three defined concentrations follow a relationship written as $C_r > C_R \gg C_0$.

Now, the diffusion flux J can be derived into the number of $CaCO_3$ molecules (dQ) that are moving toward the interface within a time interval, dT, to form the mineral bridges (Figure 4-3) can be calculated using the Fick's first law [88]:

$$J = \frac{dQ}{dT} = D(2\pi r dl)\frac{\partial C}{\partial r} \tag{4-1}$$

where, D is the diffusion coefficient, dl is the length of element along the bridge's direction, r is the distance from the center of the lattice beam and C(r,T) is the instantaneous concentration of the solution. For the mineral bridge interface to advance a distance, dr, within a time interval, dT, the change in the number of solute $CaCO_3$ molecules within the mineral bridge can written as:

$$dQ = (C_r - C_0)(2\pi r dl)dr \tag{4-2}$$

By equating the quantities in Equations 4-1 and 4-2, we can obtain [89]:

$$\frac{dr}{dT} = \frac{D}{C_r - C_0}\frac{\partial C}{\partial r} \tag{4-3}$$

The concentration gradient, ∂C/∂r, can be further estimated by a simplified linear concentration profile as shown in Figure 4-3 right as [90]:

$$\frac{\partial C}{\partial r} = \frac{C_R - C_0}{L} \tag{4-4}$$

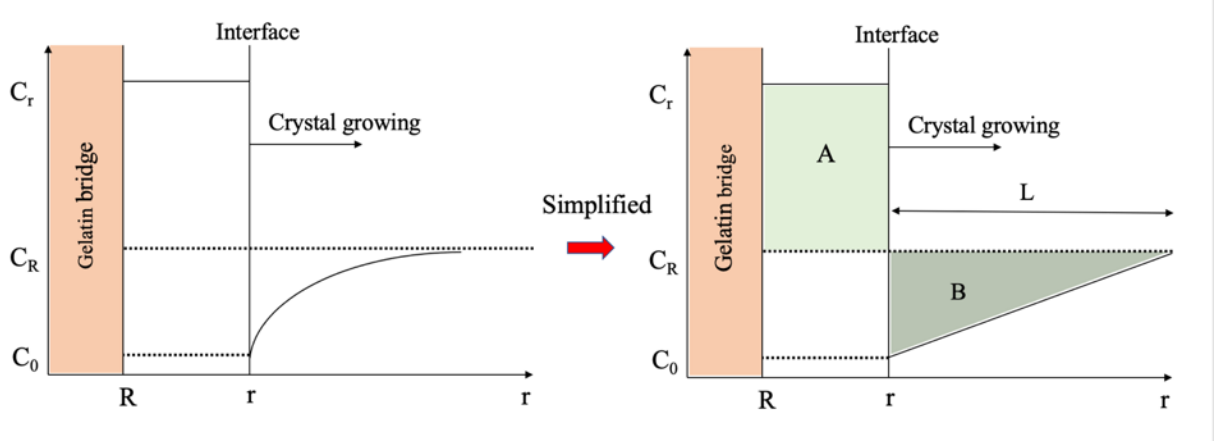

Figure 4-3 Left) Concentration of calcium as a function of the radius of a bridge. Right) a linear approximation of the concentration profile [90].

The growing distance of crystals from C_0 to C_R was denoted as L. Therefore, by equating the molar numbers of $CaCO_3$ in the two shaded areas A and B, in Figure 4-3 right, we have:

$$\pi(r^2 - R^2)(C_r - C_R)dl = \pi[(r + L)^2 - r^2](\frac{C_R - C_0}{2})dl \tag{4-5}$$

we can obtain L as

$$L = \sqrt{r^2 \frac{2C_r - C_R - C_0}{C_R - C_0} - R^2 \frac{2C_r - C_R}{C_R - C_0}} - r \tag{4-6}$$

Using the above equations, the growth rate of a mineral bridge can be derived as

$$\frac{dr}{dT} = \frac{D(C_R - C_0)}{(C_r - C_0)\left(\sqrt{r^2 \frac{2C_r - C_R - C_0}{C_R - C_0} - R^2 \frac{2(C_r - C_R)}{C_R - C_0}} - r\right)} \tag{4-7}$$

and since C_0 is negligible, it can be further simplified to

$$\frac{dr}{dT} = \frac{DC_R}{c_r\left(\sqrt{r^2\frac{2C_r-C_R}{c_R}-R^2\frac{2(C_r-C_R)}{c_R}}-r\right)} \tag{4-8}$$

If we define the mineral bridge thickness as $H = r - R$, Equation 4-8 can be rewritten as:

$$\frac{d(H/R)}{d(DT/R^2)} = \frac{1}{\frac{C_r}{C_R}\sqrt{(H/R+1)^2\left(\frac{2C_r}{C_R}-1\right)-(\frac{2C_r}{C_R}-2)}-\frac{C_r}{C_R}(H/R-1)} \tag{4-9}$$

The initial condition is $H(T = 0) = 0$. Now, if we set $C_r/C_R = \theta$, $H/R = \alpha$, and $DT/R^2 = \beta$, we will have:

$$[(\sqrt{(\alpha+1)^2(2\theta-1)-(2\theta-2)})\theta-\theta\alpha-\theta]d\alpha = d\beta \tag{4-10}$$

Finally, by setting the boundary condition, when $T = 0$, the $\beta = 0$, and integrating Equation 4-10 from 0 to β, we will have

$$\frac{\theta(\theta-1)}{\sqrt{2\theta-1}}\left\{\left[(\alpha+1)\sqrt{\frac{2\theta-1}{2\theta-2}}\sqrt{\frac{2\theta-1}{2\theta-2}(\alpha+1)^2-1}-\ln\left(\sqrt{\frac{2\theta-1}{2\theta-2}(\alpha+1)^2-1}+(\alpha+1)\sqrt{\frac{2\theta-1}{2\theta-2}}\right)\right]-\left[\frac{\sqrt{2\theta-1}}{2\theta-2}-\ln\left(\sqrt{\frac{1}{2\theta-2}}+\sqrt{\frac{2\theta-1}{2\theta-2}}\right)\right]\right\}-\theta\left(\frac{\alpha^2}{2}+\alpha\right)=\beta \tag{4-11}$$

Theoretically, mineral crystals start to precipitate in a few seconds, and thus the initial time T_0 cannot equal zero. The experimental parameters assumed: $R = 200\ \mu m$, $\theta = 4.8$ and $D = 1.6\ x\ 10^{-9} m^2/s$ [90]. The mineral bridge thickness as a function of time is plotted in Figure 4-16. It can be observed that the experiment results agree reasonably well with the presented model.

4.3.7 Self-healing experiment

To examine the self-healing capability of ECM, single-edge notch-sand slurry beams were prepared, similar to the method presented in the cubic- and cuboid-samples fabrication process section. The first cycle was initiated with the beam samples that were fractured completely in two pieces under three-point bend test and then placed back into the silicon mold. For the success of the self-healing experiment, it was necessary to assemble the two parts as close as possible following the crack pattern. To demonstrate the self-healing process, a constant amount of 2 mL of the calcium-enzyme solution was titrated evenly on the surface of the crack region. Then CO_2 gas was aerated through a rubber tube with constant pressure on the crack surface for 10 min. Samples were desiccated in the 100℃ oven for 24 h before undergoing the three-point bending fracture test. The above fracture/healing procedures were repeated six times and the data reported.

4.3.8 Reinforced ECM

We tested the ability of tannin to improve ECM performance. To this end, we added tannin, 0.8% by weight, to ECM. This amount is significantly higher than the amount of gelatin used to achieve stronger crosslinking. In theory, the gelatin-tannin system can form more

numerous and stronger bonds at a faster rate than the gelatin system. However, the performance of crosslinking bonds in compression is not as good as in tension. The powdered wine tannin from Midwest Homebrewing and Winemaking Supplies. Inc was selected. Tannin was mixed with gelatin at 28% by weight gelatin and sand particles and stirred for two minutes. Calcium carbonate solution was prepared in a similar fashion described for prior experiments and heated to 35℃. The matrix was then poured into the cubic silicon mold and 7 mL solution was pipetted on each cube. The samples were then desiccated before conducting the compression test.

A 50% concentration of glutaraldehyde was acquired from TCI AMERICA Co. as the ECM crosslinking agent. ECM samples were then prepared as described in the Cubic and cuboid ECM sample fabrication section. A 1:1 gelatin/glutaraldehyde ratio was then added by weight on the surface of the ECM samples. The samples were placed at room temperature for half an hour until the gelatin/glutaraldehyde solution was completely permeated into the sample. Last, samples were desiccated for another 24 h and then mechanically tested.

4.3.9 AFM (Atomic Force Microscopy) study adhesion within ECM

The silica attached cantilever method and adhesion (pull-off) force between sand and calcium carbonate, sand and scaffold, calcium carbonate and scaffold were performed on Asylum MFP3D-BIO. The force spectroscopy data was obtained using the software (IGOR PRO program). For the particle attached experiment, we prepare 10 – 30 silica beads in 1 drop of 70% ethanol aqueous on the glass slide. The experimental procedure for the particle attachment study involves the preparation of a sample consisting of 10-30 silica beads dispersed in a 70% ethanol aqueous solution, which is placed onto a glass slide. A small amount of UV gel is applied on the same slide, and a single bead in the vicinity of the UV gel is identified for attachment using

Atomic Force Microscopy (AFM). The AFM is calibrated, and a Silicon Nitride AFM probe (Manufacturer: NanoWorld) with a spring constant of 0.08 N/m and length of 200 µm is used to approach and subsequently move away from the UV gel. The spring constant of the probe, as determined by AFM, is approximately 0.045 N/m. Next, the probe is used to approach a single silica bead and is exposed to UV light for 30 minutes to induce particle attachment. Subsequently, a layer of calcium carbonate powder is prepared on the glass slide, and the single force experiment is repeated to obtain a force displacement curve. To perform adhesion experiment, the silica attached with cantilever was moved on top and pushes into the calcite sample (radius = 5 um) for specific period/load until it reaches a defined cantilever deflection and force. Then reversing the direction as the cantilever retracts from the calcite surface. The tip remain attached to the calcite surface until enough force pulls it off the surface, which appears as adhesion. The scan rate (loading/unloading rate) was 0.50 Hz in all experiments.

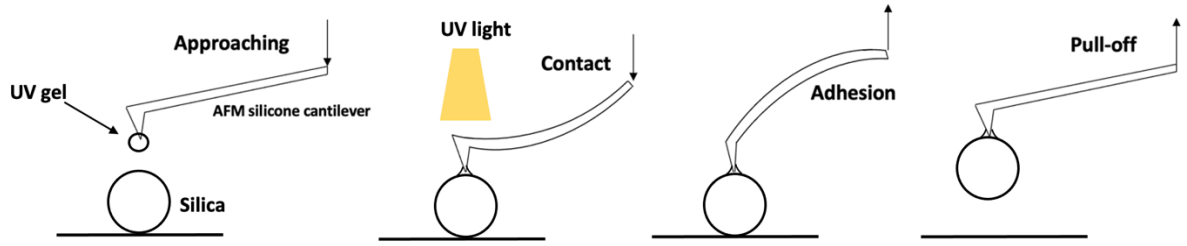

Figure 4-4 The AFM contact mode procedure for adhesion experiments. In the presence of calcium carbonate layer, attaching silica on cantilever tip through UV gel, which under cured UV light for 30 minutes before adhesion experiment. The experiment described the corresponding tip-sample interaction phenomena of silica and calcium carbonate crystals.

4.3.10 FIB-SEM study interface within ECM

Dual focused ion beam-scanning electron microscopy (FIB-SEM) is a cutting-edge technology currently used for for investigating the nanoscale surface interface. The FIB-SEM technology can be summarized simply as sample milling by a guided ionic beam at a specific preselected point of interest, which is then followed by SEM imaging. Figure 4-5 presents the details of the main components on the FIB-SEM. The ion beam column is fixed at an angle of 52°~55° with a vertical axis of the electron beam. Ga is chosen as for the ion source due to its low melting point (29.8℃), low volatility, and low vapor pressure and being easily distinguished from other elements [91]. Applying an electric field causes the liquid metal to take on a conical shape with a diameter ranging from 2 to 5 nanometers. This occurs due to a balance between electrostatic and surface tension forces. After extraction from the ion gun, the Ga^+ beam undergoes acceleration with a voltage range of 1 to 30 kV and passes through the condenser and objective lenses. As the beam scans the sample surface, a variety of ion beam-material interactions occur, producing products that can be collected and analyzed by multiple detectors. The cross-sectioning of the calcite bridging sand particle sample was performed with the FEI Scios Dual Beam FIB/SEM equipped with Oxford EDS/EBSD. First, the sample should be prepared with flat surface and coated with a 20-nm gold layer (EMS Q150R Sputter Coater). Then, the samples were then tilted by 52° and a 1–0.5-µm layer of platinum surface protection layer was deposited on the target area via electron beam-induced deposition with a current of 0.5 nA and a voltage of 30 kV. The cross section was milled using a current of 15 nA. The cleaning cross section was used 1 nA. The SEM, BSE and EDS images were acquired after cutting

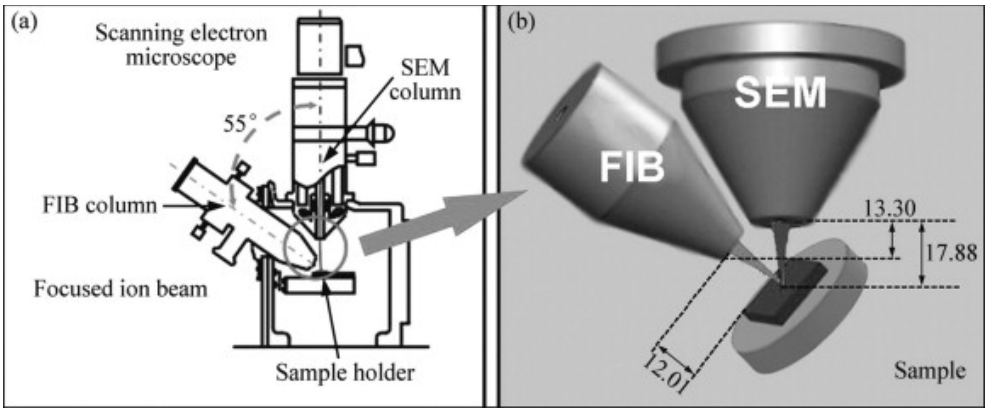

Figure 4-5 Fundamental schematic of dual FIB-SEM system [92].

4.3.11 Scaling up ECM cinder block

A standard size (8x8x16 in) cinder block silicone mold was prepared with a larger size wood case, see Figure 4-6 a. A concrete cinder block was coated with a waterproof agent for 24 hours of drying in the ambient condition and then placed inside a 4-inch perimeter longer wood box case. 2-parts silicone was stirred well for two minutes and poured into the wood case along with half an hour's vibration to facilitate air bubble removal (Figure 4-6 b). After 24 hours of curing, silicone mold was taken out from the wood case and sprayed with cooking oil to assist the sample demolding (Figure 4-6 c). Finally, ECM sand slurry was poured into the silicone mold and dehydrated in an 80℃ oven for two days before demolding (Figure 4-6 d). Figure 4-6 e shows the finished ECM cinder block.

a)  b) 

c) 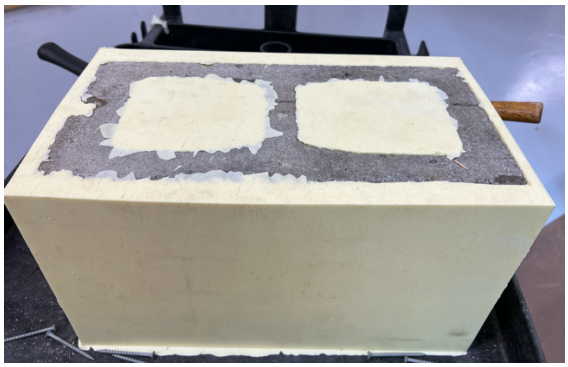 d) 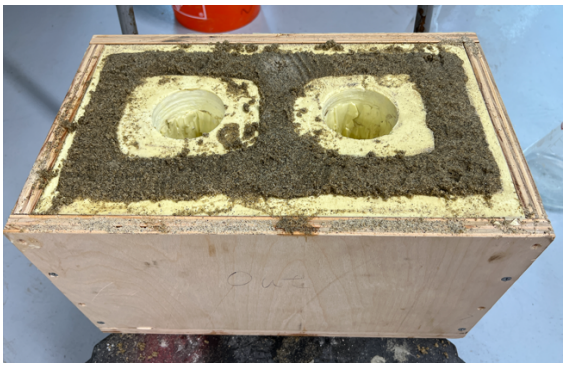

e) 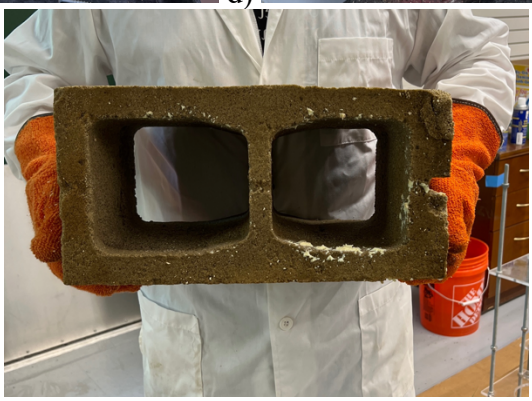

Figure 4-6 The ECM cinder block fabricated process on a real scale.

4.4 Results and Discussion

4.4.1 Catalytic performance of Carbonic anhydrase

The enzyme-catalyzed process, structure fabrication, and microstructure of ECM are shown schematically in Graphical abstract. Production of ECM is initiated by CA, which is stable in the range of pH from 6.5 to 8.5 and temperatures of 30–50℃. The reaction conditions generate an environment that promotes enzyme stability, consumes CO_2, and avoids unhealthy reagents and pollutants. The mechanism of crystal growth on the scaffold yields outstanding mechanical properties. Being an enzyme, CA is not consumed as the material cures, and the trace

amount of CA remaining in the material is ready to reinitiate the process giving ECM self-healing ability.

CA is one of the fastest known enzymes in terms of catalytic activity that can consume CO_2 at a rate that approaches a diffusion-controlled process [93]. As depicted in Graphical abstract, the creation of ECM is based on CA catalyzing the rapid precipitation of $CaCO_3$ to create mineral bridges that connect the sand aggregates in two separate steps: CA first catalyzes the reversible hydration of CO_2 to bicarbonate (Equation 3-1), which then reacts with calcium ions in the solution to precipitate $CaCO_3$ (Equation 3-2). The efficiency of the reactions depends on four key factors: (1) the concentration of calcium ions, (2) the concentration of dissolved inorganic carbon, (3) the pH value, and (4) the availability of a nucleation site [94, 95]. The catalysis by CA enzyme shows a high biomineralization efficiency where the calcite crystals ($CaCO_3$) self-assemble into a sand-gelatin matrix to establish "bridges" between the sand particles. Gelatin serves here as a harmless and odorless scaffold, which gains strength by physical crosslinking after dehydration. It can be regarded as a carrier of crystals, connecting the whole microstructure system.

There is enough ambient CO_2 in the air to drive the chemical reaction shown in Equations 3-1 and 3-2. While the reaction between CO_2 and water is reversible, both sides of the reaction can proceed simultaneously to achieve a 'dynamic equilibrium', which hinders the precipitation of the calcite crystals. In this process, CO_2 dissolves in water to form carbonic acid. Carbonic acid will form a precipitate with free calcium ions, effectively removing product and driving the forward reactions and eliminating the probability of reversal. As the reaction proceeds, a large number of hydrogen ions are produced in the solution, lowering the pH of the solution, which reduces the CO_3^{2-} activity and impedes the forward reaction. Therefore, to ensure efficient

precipitation of calcite, a buffer is added. The buffer solution is composed of a weak acid 'HA' and salt 'Na' where the alkali 'A' bonds with a H^+ ion, keeping the pH value of the solution in the neutral range and promoting precipitation of calcite crystals.

As a first step in developing the material, we wanted to quantify CA efficiency. To accomplish this, we measured the weight gain from the precipitated crystals produced in the enzymatic reaction. The results of the weight gain of four different solutions are presented in Figure 4-8, where the procedures and details are discussed in the Experimental procedures section. Here, Ca represents the aqueous solution that includes only the calcium source; BCa represents the base and calcium source solution; BEC represents the base, CA enzyme, and calcium source solution; and ECA represents the CA enzyme and calcium source solution. Within the same time range, the ECA sample obtained the highest average weight gain, about 0.82 g, which is higher than the BEC samples, about 0.09 g, and significantly higher than Ca samples, about 0.28 g, where the p values of BCa, BEC, and ECA are much less than 0.05 indicating that the datasets have distinctly different means compared with Ca. The pH of the aqueous solutions was monitored at 0 and 10 min with CO_2 aerate (see Figure 4-9). The pH of the ECA solution changes most significantly and is the lowest at 10 min. These results indicate that the carbonation by enzyme catalysis is efficient and the calcium crystallization ability in ECA is the highest in the different groups.

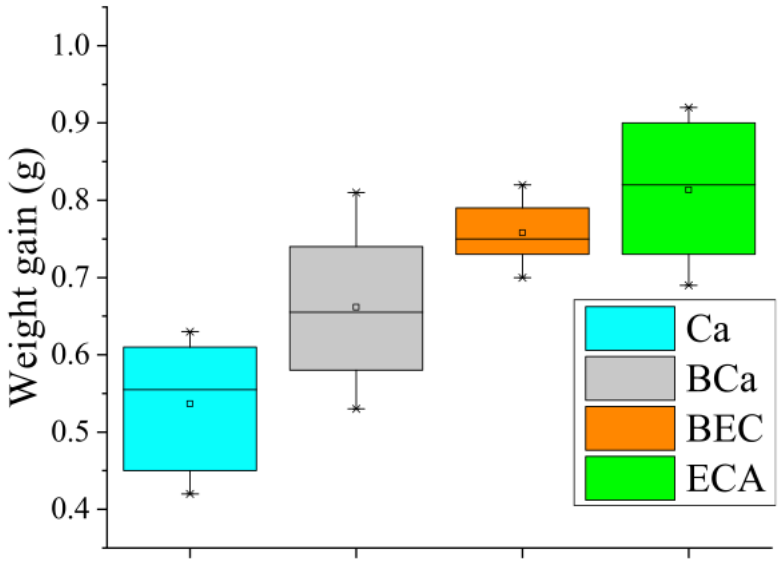

Figure 4-7 The Catalytic performance of carbonic anhydrase. Measurements of weight gain for four different material designs with constant CO_2 gas treatment with a rate of 5 bubbles per second showing that is the highest for ECA samples among all groups. In the boxplot, the median value is illustrated as (-), the mean as (■), the values at 25 and 75% as box edges, and the values at 5 and 95% level as whiskers. Statistical significance versus Ca: Ca: M = 0.54, SD = 0.08; BCa: M = 0.75, SD = 0.05, p = 0.0001; BEC: M = 0.66, SD = 0.10, p = 0.022; ECA: M =0.82, SD = 0.09, p = 0.0001.

It should be noted that the weight gain is not equal to the number of precipitated crystals but indirectly reflects the catalytic ability of the enzyme to convert CO_2. The weight gain in every solution is equal to the quantity of absorbed CO_2, which can be used to calculate the weight of precipitated calcite based on Equations 3-1 and 3-2. The catalytic efficiency K_{cat} of CA at 25 C and pH=9 is around 10^6 molecules/s [96, 97], which is defined as the CO_2 hydration turnover rate or the maximum number of substrate molecules transformed into the product by a single CA in 1 s. The theoretical and experimental results are compared in Table 4-3. The

theoretical result for CO_2 molecules is 3.49 x 10^{23} , and the quantity of the experimental CO_2 molecules is 1.12 x 10^{22} . Considering that the experimental error and the effect of CO_2 on pH (K_{cat} will change by pH), the experimental results agree well with the predicted results in the ambient-temperature regimen, and the enzyme improves carbonation.

Table 4-3 A comparison of the CA enzyme catalytic activity in experiment and theory

Kcat = 10^6 molecules/s	Weight gain (g)	$CaCO_3$ (g)	CO_2 (Molecules)
Experiment	0.82	1.86	1.12 x 10^{22}
Theory	2.56	5.80	3.49 x 10^{23}

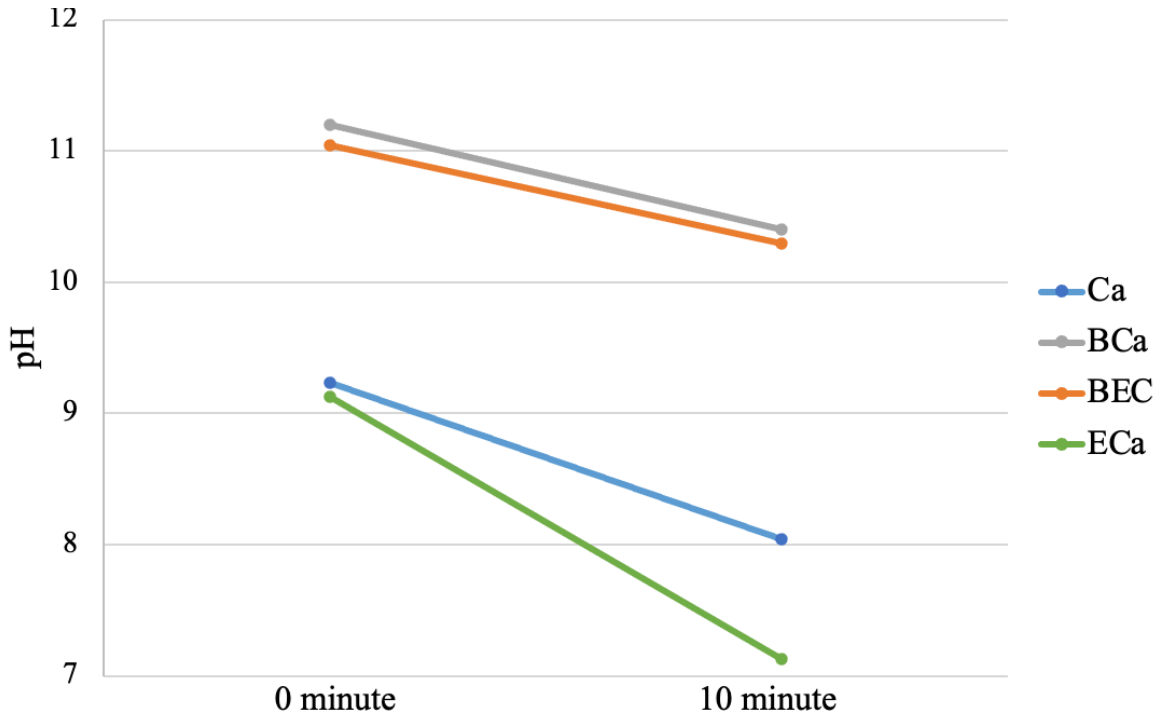

Figure 4-8 The time-dependent pH of aqueous solution with CO_2 aeration.

Comparing the BCa samples in Figure 4-8 with the Ca samples, we find more crystals precipitated after adding a base reagent to the solution. From Equation 3-1, the hydroxide ions neutralize the hydrogen ions in the solution and promote the reaction forward. Wilson et al. previously chose the urease enzyme based on this approach and applied it for biomineralization [98]. The urease uses the nitrogen source urea to produce hydroxide ions to increase the solution pH, causing calcite to precipitate from the calcium ions in the solution. We previously compared the CA-mediated calcite precipitation with the urease method, and the comparisons included mechanical properties and structure formation. The calcite without sand formed by the urease slurry had a non-uniform crystal structure, but the calcite from the CA slurry had a uniform crystal structure in layers. The calcite in the CA method adheres to the sand particles and forms an organized, uniform layered structure, most likely due to the faster production of the precipitates decreasing the mobility of solid particles. Additionally, in terms of mechanical properties, the compressive strength and tangent modulus of the CA samples outperformed the urease samples. These experiments indicate that the CA method is more effective in mineral precipitation and the assembly of sand slurry construction materials.

4.4.2 Microstructural characterization

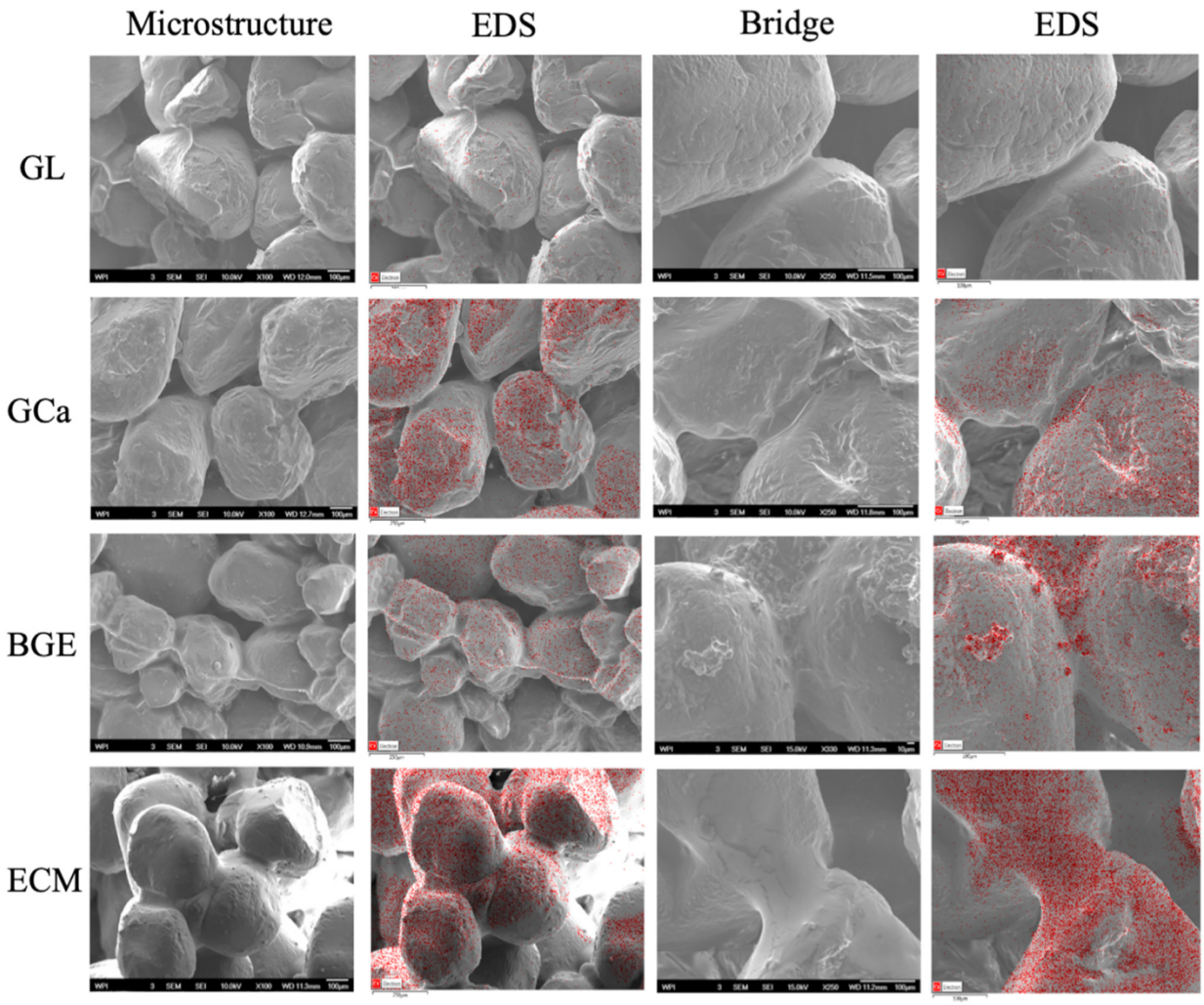

Figure 4-9 Microstructure of sand slurry materials with different compositions. The SEM images and EDS maps compare the effects of the CA enzyme, calcium source, and high pH as aqueous solution additives on different samples. The catalysis of the CA enzymes results in an ECM with an organized structure. Also, calcium is mostly distributed uniformly on the ECM surfaces and bridges. Compared with GL, GCa, and BGE samples, the mineral bridges in the ECM have wider and longer dimensions. Under same condition, the EDS maps of the ECM samples also show the highest amount of calcite crystals compared with the other three groups.

To determine whether the composition and morphology of ECM are influenced by the presence of the CA enzyme, four different compositions were used to assess the quantity of mineral precipitation, mineral distribution, structural arrangement, and bridge sizes. The control, GL (Gelatin + Sand), samples were created with the same media as the ECM (CA + Gelatin + Ca^{2+} + Sand), except for the CA enzyme and calcium source. The BGE (Base + Gelatin + CA + Ca^{2+} + Sand) represents a high-pH control group, where higher pH helps produce more particles of calcite. The GCa (Gelatin + Ca^{2+} + Sand) samples demonstrate the effectiveness of the CA enzyme in crystal precipitation and microstructure, which is fabricated with the gelatin and calcium source.

Compared with the other three groups, the structure of ECM is denser and more organized. The surfaces of GL and groups without CA treatment (GCa) samples are smooth, and their bridges in some domains are too short or too fine. The mineral bridges in BGE are larger than in GL, but the overall arrangement of the structure is inordinate. During the preparation of ECM, most of the calcite crystals were trapped or covered in the gelatin and formed a bridge, and it was difficult to observe the crystal distribution of the surface directly by SEM. The samples were then analyzed by energy-dispersive X-ray spectroscopy (EDS).

EDS can qualitatively determine and locate the crystals by the content of calcium. The results of the distribution of Ca^{2+} from EDS analysis are shown in Figure 4-10. There is no calcium observed in the EDS maps of the GL samples since no calcium was added. EDS revealed a dense distribution of calcium in ECM that contributed to the broader and wider bridges covering a large portion of the surrounding sand particle surfaces. For the GCa and BGE samples, only a small amount of calcium was distributed either on sand surfaces or on bridges.

4.4.3 Fracture mechanism

Figures 4-11A and 4-11B display a close view of the bridging mechanism between ECM and ECa (CA + Ca^{2+}) samples. Although the calcite crystals form a network that bridges the sand particles, the size of the ECa bridge (around 80 mm) is smaller than the that of ECM (around 150 mm), meaning that the gelatin scaffolding enhances and extends the bridges. Similar results have also been previously reported [99]. The crystals align closely in the gelatin, resulting in an organized and dense structure that establishes a mechanism for the enhancement of the mechanical properties of the ECM. The fracture toughness of ECM relies on the mineral-bridging connections among the sand aggregate. Figures 4-11C and 4-11D show ECM samples after mechanical testing, displaying the cracks that propagate in the center of the bridges in the transverse direction. Figure 4-11D shows a typical fractured surface at the crack tip region where a 150-mm-diameter fracture surface is exposed. Figure 4-11E shows that sand aggregates were detached from the matrix. This detachment is the other major fracture mechanism after bridge failure and was found within the sand-gelatin system. However, this mechanism occurs more often during the self-healing cycles.

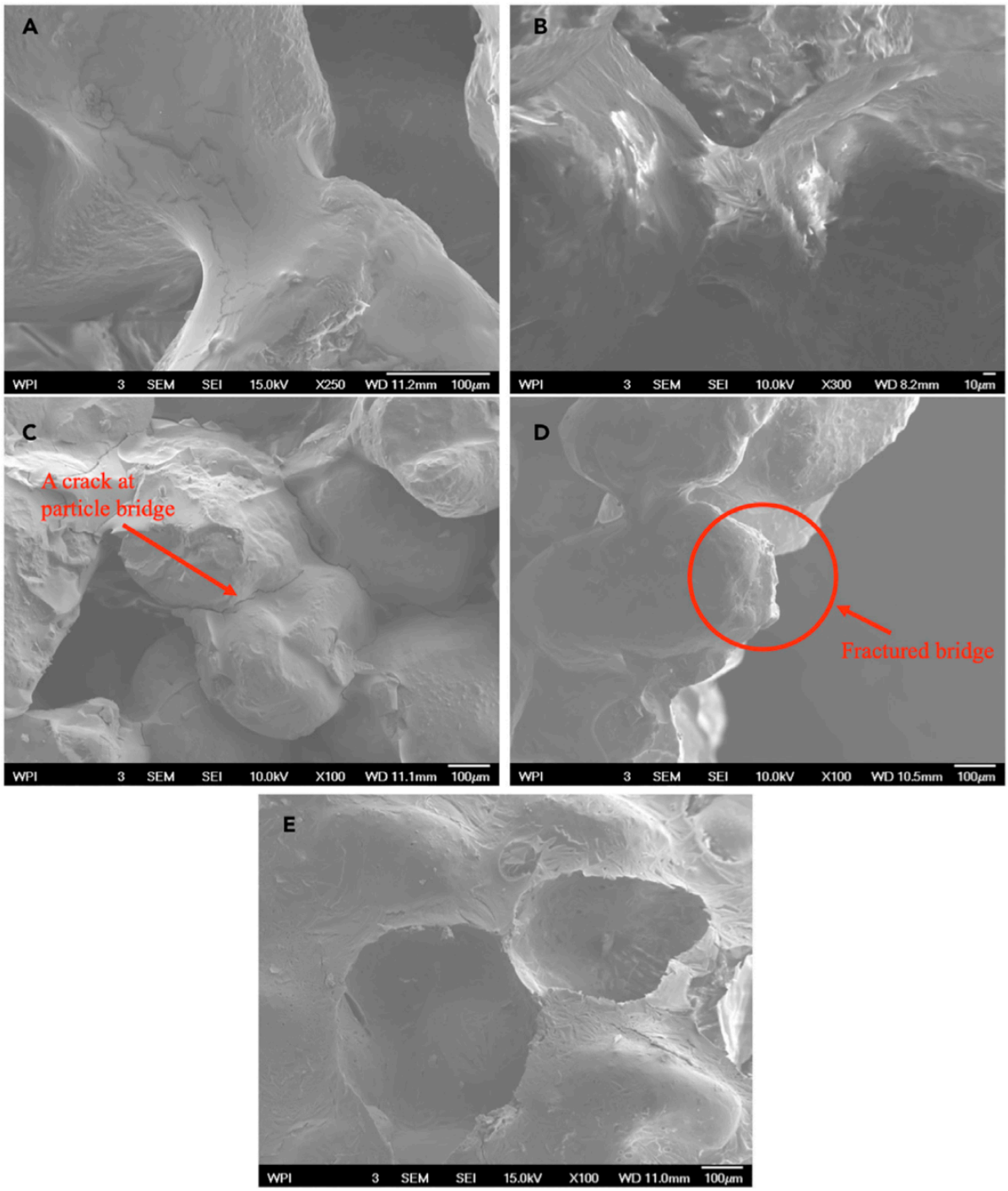

Figure 4-10 Mechanisms of fracture in ECM. (A and B) These SEM images show that the dimension of a typical crystal bridge in non gelatin samples, ECa (B), is smaller than of a typical

bridge in ECM (A). This proves the ability of the gelatin to establish a proper scaffolding framework for crystal formation that further enhances and extends the size of the crystal bridges. (C and D) A typical crack (C) initiates and grows in the calcite bridges bonding the sand particles. A fractured bridge can be observed in (D). (E) An example of the detachment of the sand particles from the matrix.

4.4.4 X-ray diffraction and Fourier transform infrared spectroscopy analysis

To examine the crystallinity and chemical composition of the ECM enzyme product, powder X-ray diffraction (pXRD) and Fourier transform infrared spectroscopy (FT-IT) were performed on a Bruker AXS D8 Focus (Bruker, Billerica, MA, USA) at 25 C, and the pXRD spectrum used a CuKa radiation source at 40 keV and 40 mA from 20° to 90° of 2θ with a step size of 0.100°, against the baseline and Bruker Optics Vertex 70 equipped with a Specac Golden Gate Diamond Single Reflection ATR element (Bruker). The calcium carbonate produced by the enzyme solution was rinsed and dried for analysis. Figure 4-12 compares the pXRD spectrum against the reference spectrum for calcite, and Figure 4-13 compares the FT-IR spectrum of the dried enzyme product against the baseline FT-IR spectrum for calcium carbonate obtained from the RUFF Project database [100]. Both results clearly verify the chemical composition and crystallinity of the enzyme product as calcite.

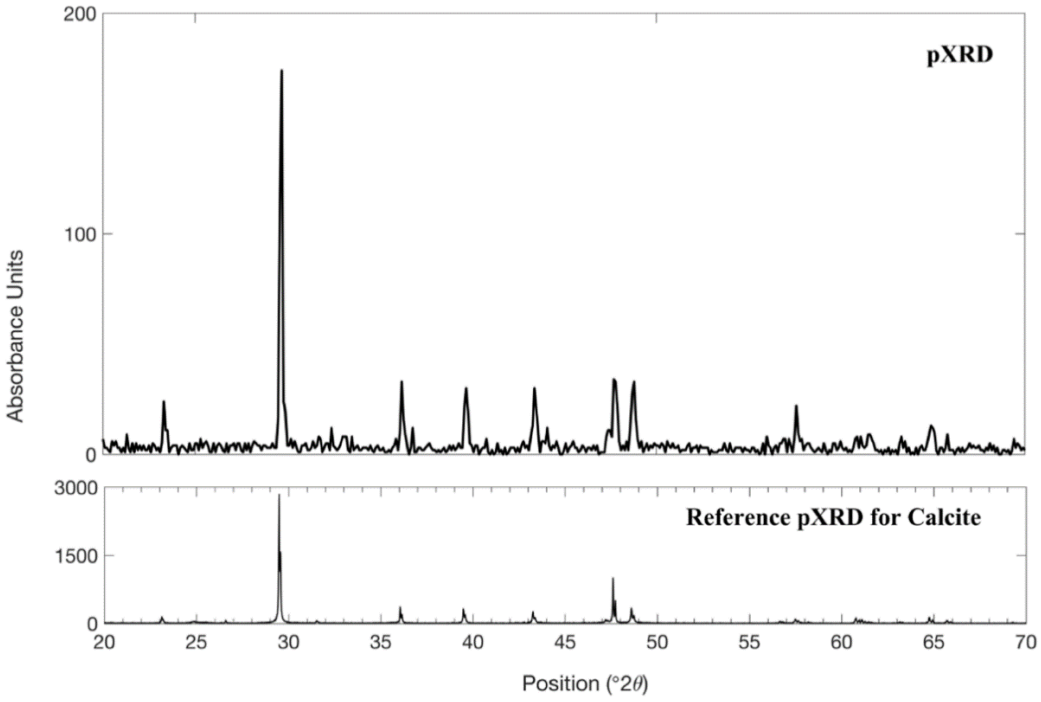

Figure 4-11 Powder X-ray diffraction (pXRD) analysis of the produced crystals from CA enzyme method, with comparison to the reference spectrum for calcite. This comparison confirms the crystallinity of the product resulting from the enzyme method is calcite.

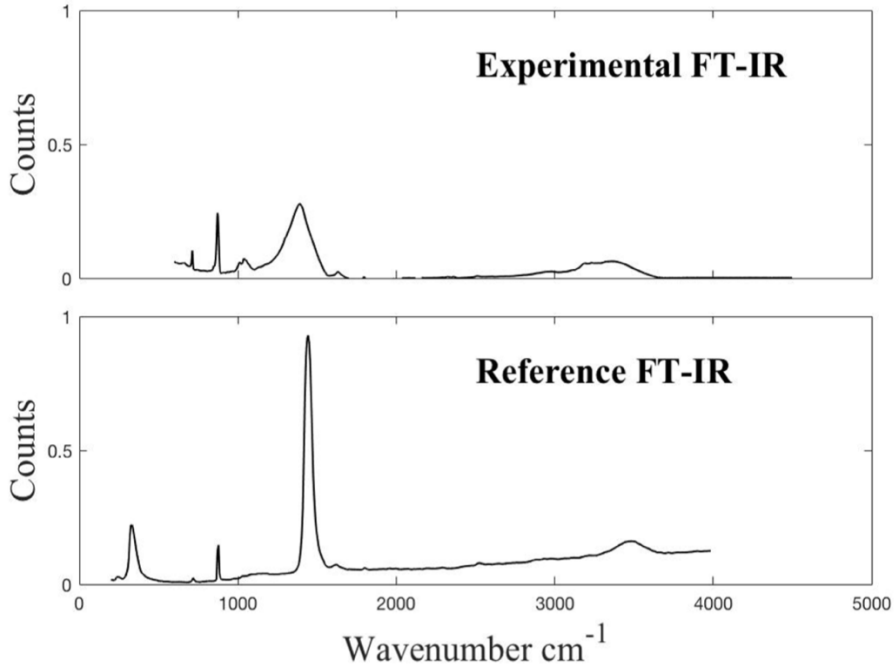

Figure 4-12 Fourier Transform Infrared Spectroscopy (FT-IR) analysis of calcium carbonate produced by enzyme catalysis compared to a reference spectrum where the sample precipitate had a dry weight of 0.4 µg. These data confirm the chemical composition of the repair product resulting from the enzyme solution. The broadening of experimental peaks may be related to the size of the crystalline domains, the presence of defects or strain, or the amount of amorphous content in the calcite crystals.

4.4.5 Mechanism and Modeling of Crystal growth

Understanding crystal nucleation and growth is of prime importance to determine and predict the physical properties of ECM, and we therefore used optical and electron microscopy to study the time lapse of crystal growth in ECM samples. Experimental details for the preparation and execution of these studies are described in the supplemental information section, Crystal bridge growth model. In Figure 4-14, SEM and optical images following the formation of calcite

crystals on sand-gelatin surfaces are presented. In the ECM, the rough surface of the gelatin scaffold and sand provides numerous sites for nucleation of calcite crystals. With CO_2 as a reactant, crystal growth can be defined by heterogeneous nucleation; thus, the energetic-barrier problems associated with preliminary nucleation are inevitable. However, CA reduces the activation energy for the reaction barrier. The CA active site provides a favorable environment for the reactants and transition state, allowing them to interact with each other in a way that lowers the energy barrier for the reaction. Specifically, the zinc-bound hydroxide ion can easily attack the carbon dioxide molecule, forming the bicarbonate intermediate. The enzyme also stabilizes the bicarbonate intermediate and the transition state by forming hydrogen bonds with them, which lowers their energy and makes it easier for the reaction to proceed. From the images in Figure 4-14, we find that calcite crystals form immediately by enzymatic catalysis. Crystal growth then results in the gradual expansion of the cross-sectional area of the bridges and the formation of the bridging network between sand particles. In about 20 min, most geometrical voids are filled, and the structural system shows strong integrity. To further verify the processes of crystal growth, additional SEM and optical images of the bridging network are presented in Figure 4-15.

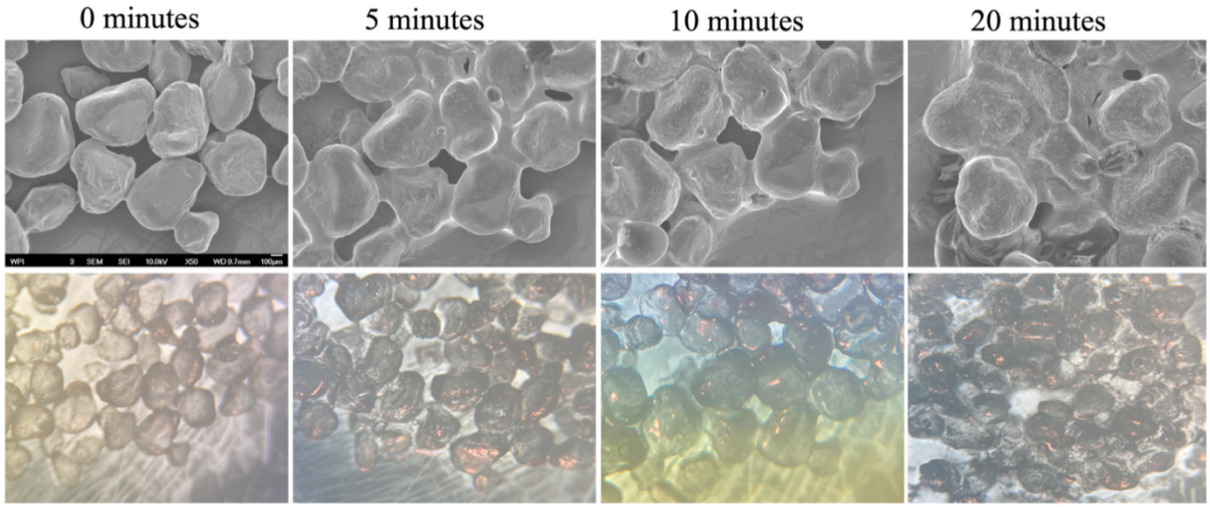

Figure 4-13 Crystal growth within ECM. (Top row) The scanning electron microscopy and (bottom row) optical images of the process of enzymatically catalyzed mineral precipitation and growth in the sand-gelatin system within the first 20 min of the curing process.

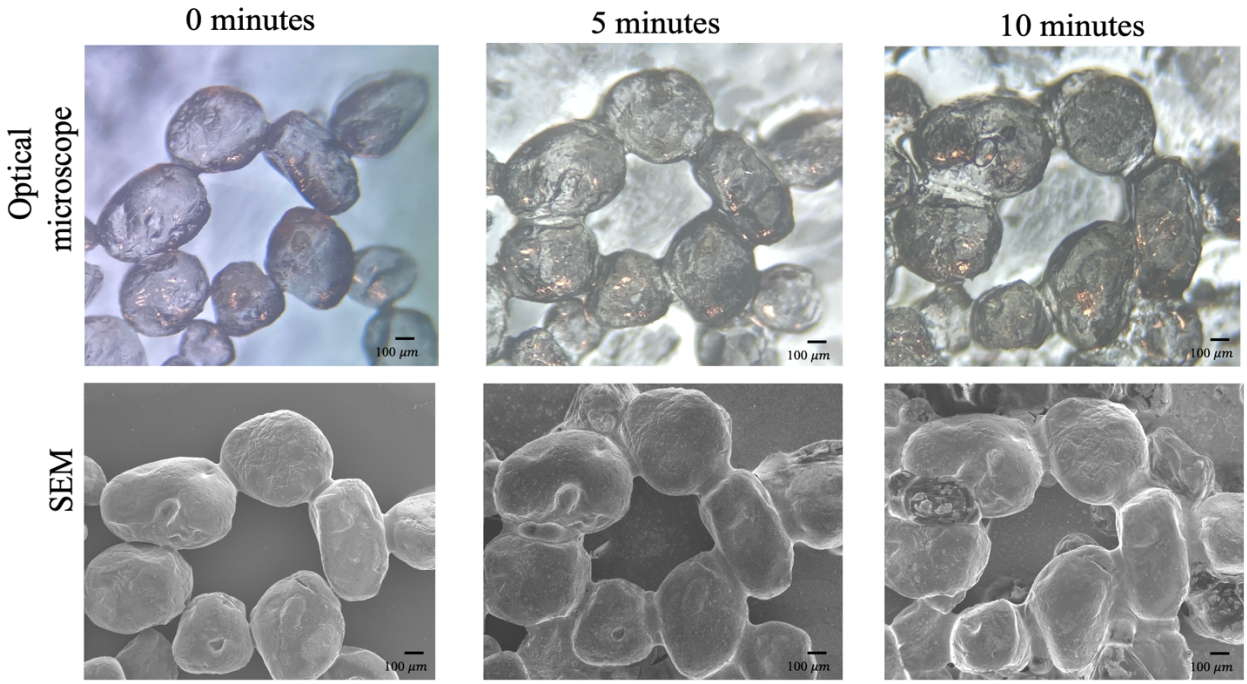

Figure 4-14 Optical microscopy and SEM images of crystal precipitated and the consequent mineral bridge growth in a typical ECM sample within 10 minutes.

Crystal growth in ECM is diffusion controlled. The details of the crystal growth process on the sand-gelatin system using the diffusion relationships by Fick's First Law [101] are presented in the supplemental information section (Crystal bridge growth model). The equations were then analytically solved to verify the experimental results. The equations present the crystals growing on a cylindrical sand-gelatin scaffold element; see Equations (4-1)–(4-11). The results of the crystal growth modeling framework are presented as the average thickness of the mineral bridges as a function of time in Figure 4-16. Whereas we find that the thickness of the mineral bridges grows as a function of time, the rate of mineral growth decreases after about 5

min. In oversaturated $CaCO_3$ solutions, the solute $CaCO_3$ aggregates rapidly to form mineral bridges that grow from the surface of the gelatin scaffold. When the concentration of calcite around the gelatin is below the oversaturation value, the calcite solution must aggregate toward the nucleation site, which will slow down the growth rate of the mineral bridges until reach the oversaturate concentration. At 20 min, the experimentally measured average value of mineral bridge thickness is lower than the theoretical result. This difference is because the catalytic capacity of the enzyme cannot precisely reach the level of theory and is supported by the data in Table 4-3. We believe that the calcite crystal growth on the gelatin in ECM is similar to the growth pattern on other polymer scaffolds [102]

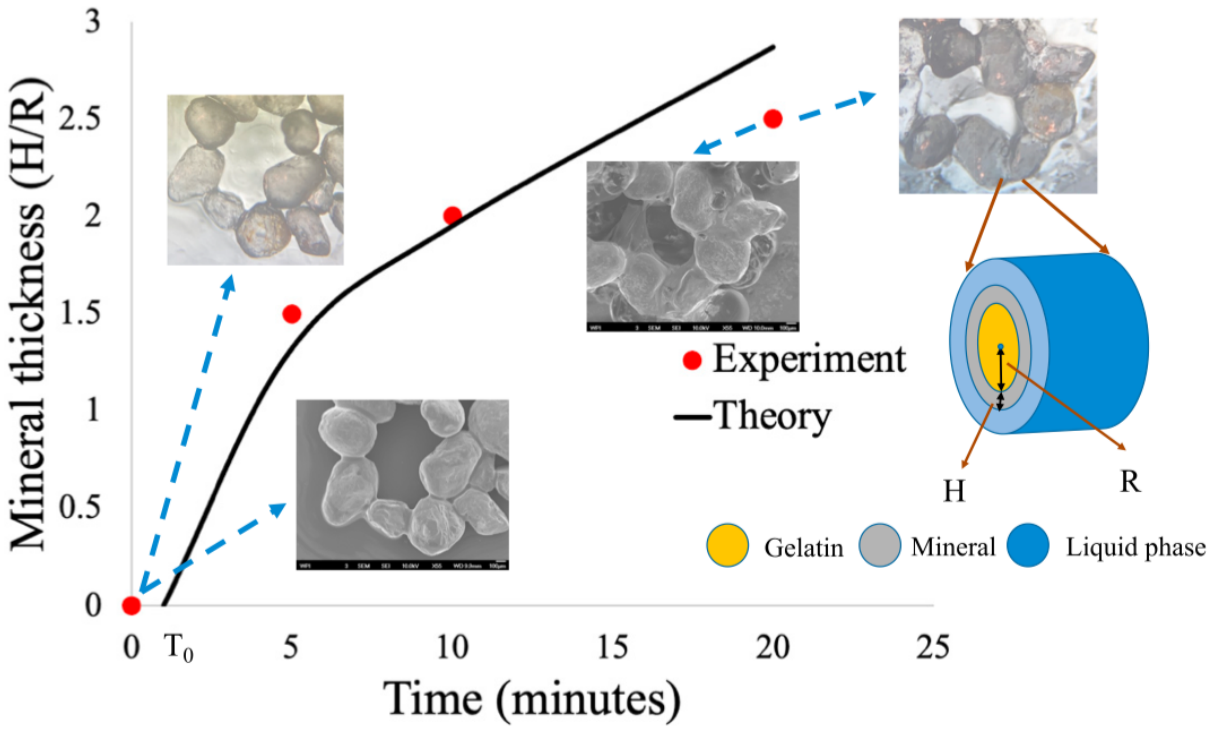

Figure 4-15 Growth of mineral bridges in the structure of ECM. The normalized average thickness of the mineral bridges (H/R) in the structure of ECM is presented as a function of time. H is the thickness of a mineral bridge, and R is the initial average thickness of the gelatin

network for the sand-gelatin system. The solid line represents the numerical calculation from the diffusion model; the dots present the experimental measurements. The schematic on the right side depicts the cross section of a mineral bridge.

4.4.6 Compressive strength of ECM

The mechanical experiments focused on the compressive strength, tensile, and fracture properties of ECM with reference groups. Compressive tests and three-point bending tests were performed to study the mechanical performance of the proposed ECM. Five different groups of sand slurry samples were prepared and termed as follows: ECa (CA + Ca^{2+}), GCa (Gelatin + Ca^{2+}), BGC (Base + Gelatin + Ca^{2+}), BGE (Base + Gelatin + CA + Ca^{2+}), and ECM (CA + Gelatin + Ca^{2+}). It is noted that the above samples all incorporate the calcium source. The compressive strength and elastic moduli are presented in Figure 4. The main function of construction materials such as concrete is to provide compressive strength. The compressive strength of the concrete mixture depends on the properties of the ‘‘aggregate’’ and cement ‘‘mortar matrix.’’ As a potential building material, ECM also possesses its own aggregate and mortar matrix, and its mechanical properties are similarly a function of the strength of sand and mineral bridge. The data in Figure 4A shows that gelatin as scaffold in GCa can increase the compressive strength of the sand slurry material ECa, but comparing GCa with ECM, an average strength of 4.5 MPa is not noticeable. Additionally, the results show that the ECM has the highest compressive strength and elastic modulus. The average compressive strength of the ECM samples is 9 MPa, which is twice as high as the GCa specimens, 4.7 times the ECa specimens, and significantly higher than the base amended specimens of BGC and BGE (Figure 4-17). Moreover, the elastic modulus of ECM is higher than other specimens, showing that the elastic

deformation under the same external force is smaller. From EDS-SEM images in Figure 4-17, we find that the average size of the crystal bridges in the ECM is about 150 mm wide and 50 mm long. Also, the calcite crystals in ECM are distributed more uniformly. Comparing the EDS maps of ECM samples with BGE and BGC samples, a significant amount of calcium was observed on the ECM bridges. Therefore, comparing the structure and mechanical properties of the other three groups, we deduce that the crystal bridges are the principal strengthening and toughening mechanisms in these heterogeneous materials. It is noted that the compressive strength of ECM is more than two times the minimum standard for cement mortar (3.5 MPa) with a density of 1.66 g/cm^3 compared with the cement mortar density of 2.2 g/cm^3 (see Figure 4-18).

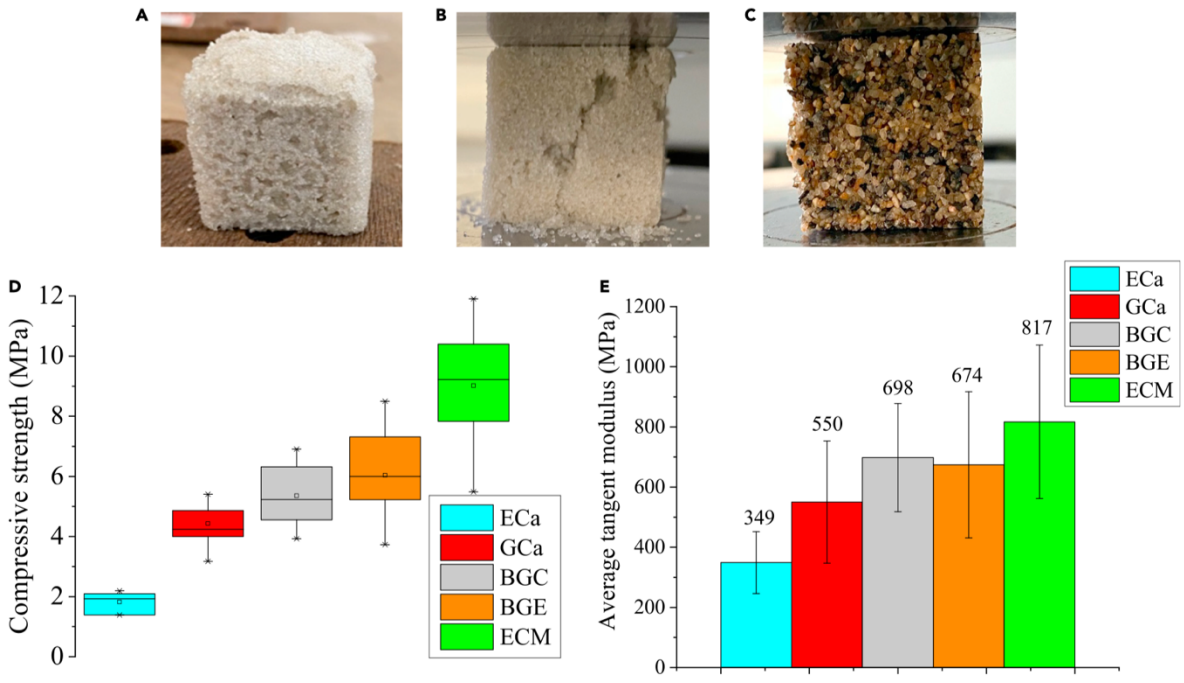

Figure 4-16 Compressive strength and elastic modulus of ECM. (A) A CA sand slurry sample prepared with #No. 50 (the sand retained on a 300-mm sieve) white sand. (B) The sample after the uniaxial compression test. (C–E) (C) A CA sand slurry sample prepared with #No. 30 coarse

sand (retained on a 600-mm sieve). (D) The compressive strength (ECa: M = 1.85, SD =0.29; Statistical significance vs. GCa: GCa: M = 4.50, SD = 0.69; BGC: M = 5.35, SD = 1.08, p = 0.023; BGE: M = 6.03, SD = 1.46, p = 0.0001; ECM: M = 9.02, SD = 1.95, p = 0.00001) and (E) tangent modulus of fine-sand slurry samples prepared with five different aqueous solutions. ECM exhibits the highest compressive strength (~9 MPa) and shows the highest tangent modulus.

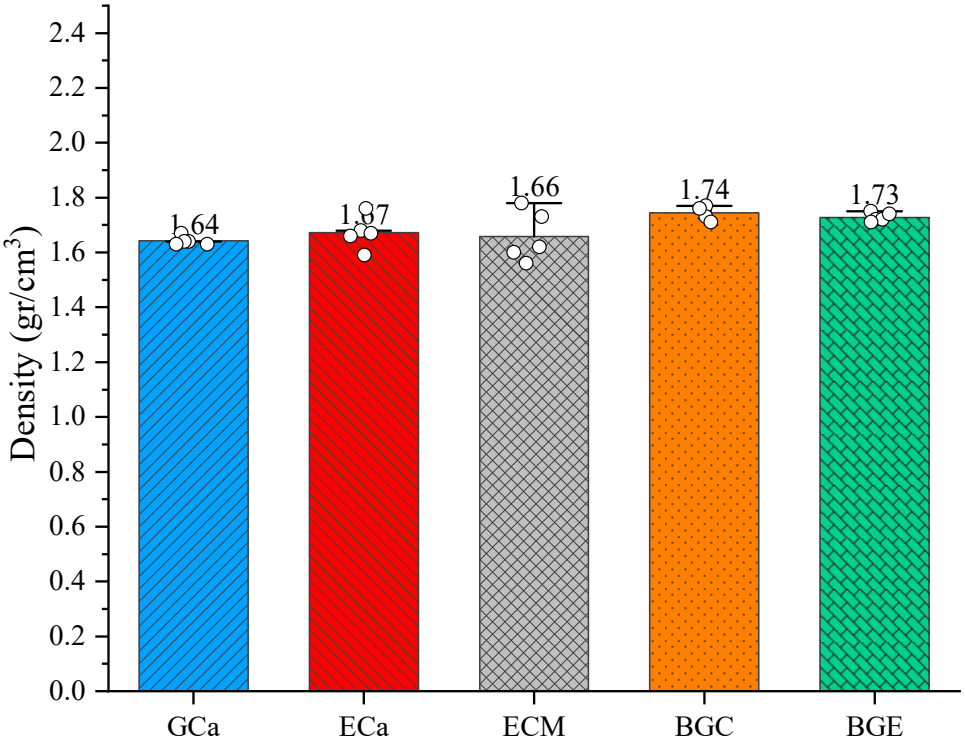

Figure 4-17 The density of the materials presented in this study. The density of ECM is 1.66 gr/cm^3 comparing to the cement mortar density of about 2.2 gr/cm^3.

To further investigate the underlying strengthening mechanisms, the sand slurry cubic samples with coarse aggregates were also fabricated (Figure 4-17C), and their compressive strength is presented in Figure 4-23. The coarse-sand slurry ECM performs at a higher average strength than high-pH BGE samples by about 31% and control gelatin samples GCa by about 17%. CA enzymes play the same role in both fine and coarse-sand samples by increasing the rate of crystal precipitation within a fixed time and, consequently, strengthening the samples. However, the maximum size of the crystal bridges is limited by the amount of calcium, which prevents the increase in strengthening in coarse aggregates above a certain threshold. The maximum size of bridges limits the challenge of bonding large-sand particles, resulting in relatively lower strength for coarse aggregate samples than for fine aggregate samples. Since the size of the crystal bridges in the fine aggregate samples is comparable to the size of the particles, the forces are more evenly distributed in the microstructure of the materials and, hence, higher overall strength and fracture energy. Additionally, the sand slurry samples were checked for pH after the compression experiments. Because CA activity causes a reduction of pH in the solution, we measured the pH of the specimens after the compression tests by soaking in deionized water and measuring the pH of the solution. The results can be found in Figure 4-19. It was observed that the CA enzyme will reduce the pH.

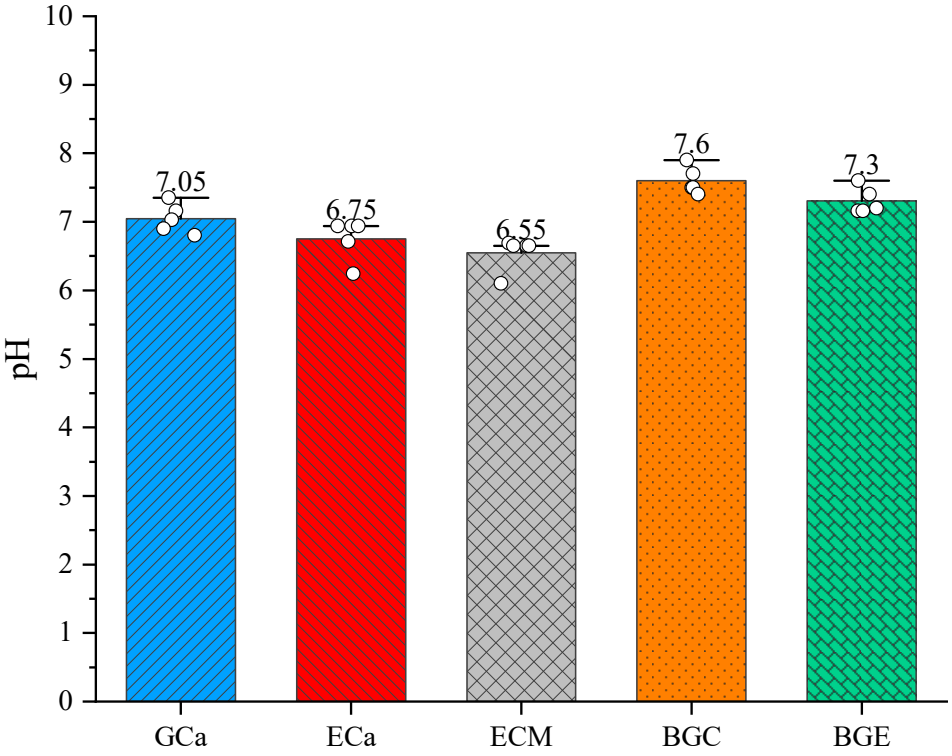

Figure 4-18 The pH values of water baths were measured directly after the compression testing. Every 25 mm cube specimen was soaked in two times mass of DI water. The ECM samples show an average pH of 6.55, which is the lowest pH compared with other samples. (Statistical significance vs. GCa: GCa: M= 7.05, SD=0.22; ECa: M=6.75, SD=0.30, p=0.058; ECM: M=6.55, SD=0.28, p=0.0049; BGC: M=7.60, SD=0.20, p=0.0015; BGE: M=7.30, SD=0.19, p=0.042).

4.4.7 Fracture test of ECM

Fracture energy is an important mechanical property of building materials since the propagation and control of cracks are highly related to the serviceability and durability of materials. The single-edge notch bending (SENB) test of ECM beam samples, shown in Figure 4-20, was conducted and the results of the fracture tests are presented in Figure 4-20B and 4-

20C. Fracture energy and load displacement curves reflect the excellent mechanical properties of ECM. The EDS maps in Figure 4-10 show that the bridges are mainly calcite crystals incorporated within the gelatin scaffold to bridge the sand particles. Fracture surfaces in Figure 3 also show the typical fracture mechanism in ECM by particle debonding and bridging failure. These results indicate that the toughening mechanism is mainly undertaken by mineral bridges. Therefore, an ECM with wider and longer bridges can exhibit excellent tensile properties. The fracture energy results indicate that CA can significantly increase the fracture energy by about 96% compared with GL and by about 75% compared with GCa. The average ultimate load of ECM samples is also higher than that of the GL samples by about 27% and of the GCa samples by about 16%. The fracture and bending tests of coarse-sand slurry ECM are illustrated in Figure S7. The fracture energy of coarse-sand slurry ECM is higher than that of the control GCa by about 23% and higher than that of the high-pH samples (BGC) by about 78%. To our knowledge, there is no other method that can create a structural sand slurry material with similar compressive strength and fracture energy.

In the sand slurry materials, calcite crystal bridges are the critical element in providing compressive strength, which plays the interlocking role in the toughening mechanism. However, the polymer scaffold provides the main toughening system. By comparing the ECM beam fracture specimens with two control GL and GCa groups, the fracture energy and ultimate tensile loads are promoted by CA enzymatic catalysis, while aggregate type and size can also affect these material's strength and fracture energy. However, similar trends are observed in the experiments on coarser aggregate ECM (supplemental information section, Fracture and bending experiments). In the coarse-sand ECM samples, the mineralized gelatin matrix plays the main toughening role.

The control GCa groups show lower fracture energy. Under high-pH conditions, CA enzyme catalysis has a more negligible effect on the fracture energy, especially in coarse-sand slurry samples (Figure 4-20, top). Although more crystals were precipitated, the impact of crystal quantity on the toughness of the coarse-sand ECM may be less than that of other factors. In Figure 4-24, more crystal precipitation does not increase the toughness of the material in the case of high pH. SEM images show that the bridges in the calcium-gelatin matrix of ECM are wider and longer than those of non-CA enzyme samples GCa, which plays an essential role in the toughening mechanism where fracture initiates in the bridges in the high-stress regions. However, since the mortar on the macro-scale is uneven, there may be other mechanisms to strengthen and toughen the specimens. The interfacial fracture toughness between the crystal bridges and the sand surface, which is a function of the surface roughness of the sand particles, can also affect the overall strength and toughness of these materials.

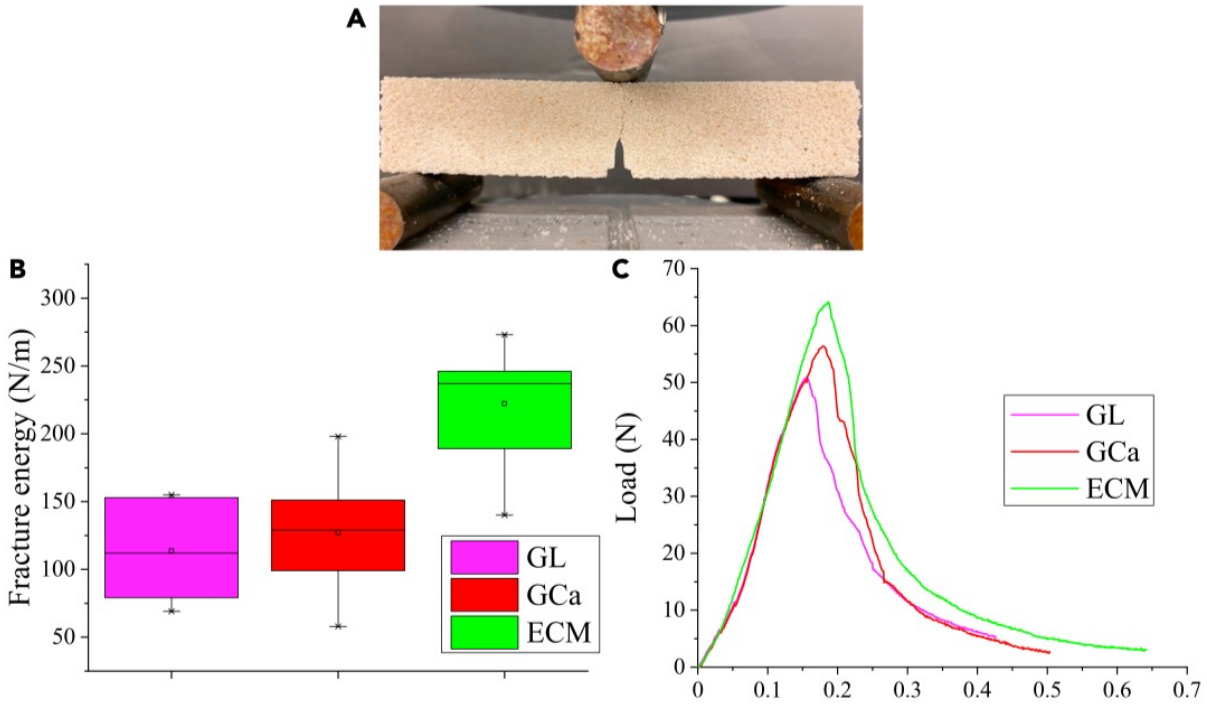

Figure 4-19 Fracture energy of ECM. (A–C) (A) SENB experimental results of (B) the fracture energy (statistical significance versus GL: CL: M = 113.6, SD = 40.2; GCa: M = 127.1, SD = 52.8, p = 0.33; ECM: M = 222.2, SD = 44.2, p = 0.00033), and (C) load-displacement curve of three different groups of sand slurry beam samples: GL, GCa, and ECM. The results indicate that ECM samples have the highest fracture energy and ultimate load.

Although previous research has found that high pH benefits the carbonation [103], the overall performance of ECM samples is superior to that of samples with high pH where adding a base is expected to promote calcium hydroxide in addition to calcite as the precipitant. Calcite primarily forms a cubic structure at room temperature, with stability and stiffness in all directions. Alternatively, calcium hydroxide crystals form a weaker, planar structure at room temperature. These different structures can be seen when the elastic modulus of calcite, ~70 GPa,

is compared with calcium hydroxide, ~48 GPa, respectively. Therefore, incorporating calcium hydroxide crystals in bridges diminishes the integrity of the material regarding compression and tension.

4.4.8 Self-healing properties

We investigated the self-healing ability of the ECM by developing an experimental procedure utilizing the three-point bending test. The fracture strength of the beam specimens for each cycle was measured to evaluate the extent of healing. The fractured samples were placed in a silicon mold in each healing cycle and treated with a trace amount of enzyme + calcium solution on the cracked surface region (Figures 4-21A and 4-21B). Pure CO_2 gas was then introduced on the crack surface for 10 min. The mineral precipitation occurred predominantly near the crack wake of the specimens, as observed by the liquid film on the sample surfaces in Figure 4-21C. Healed samples were then fully dehydrated in an oven and removed from the mold (Figure 4-21D), and three-point bending fracture tests were again conducted. The prescribed steps were repeated for each cycle, and the properties of the healed samples were studied (Figure 4-21, middle). We refer to the mechanical properties of the original sample as ‘‘intact,’’ the first repaired sample as ‘‘first,’’ and the second repaired sample as ‘‘second’’, etc.

The results show that the average ultimate loads are similar in intact and first-cycle samples at about 53 N (Figure 4-21, bottom). Six samples were tested in each group, and initially the average maximum load of the second-cycle samples decreased to 43 N, which is an 18.8% decrease from the first to the second cycle, a 13.9% decrease from the second to the third cycle, and 35.1% decrease from the third to the fourth cycle. After the fourth cycle, the ultimate load tends to be stable at about 23 N, which is reduced from the intact cycle by 52.8%. The results

clearly show that the ECM beam can reconstruct after six-times cycling damage, which shows a potential self-healing property.

The proposed test method clearly demonstrates the healing process of ECM. Healing requires only a small amount of calcium source as the filling material. Please note that healing structural materials with a large defect require the addition of filling materials, as is the case in all other self-healing methods such as MICP and LBM. Furthermore, through the catalysis of CA, the CO_2 in the air is consumed in the self-healing reaction; thus, this process also plays a small role in CO_2 sequestration during healing.

The results in Figure 8 show that the average maximum load decreases from the second healing cycle and declines up to the fourth cycle. From the fourth healing cycle, the average maximum load plateaus to about 23 N, which is one-half of the intact property.

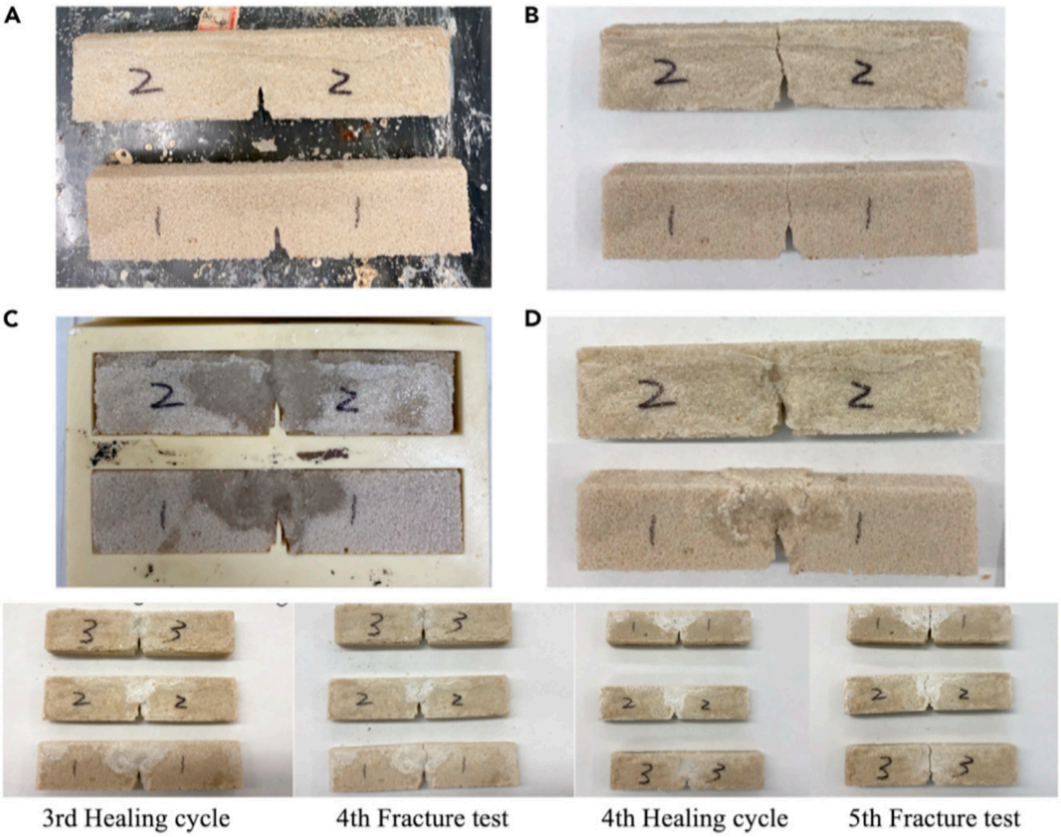

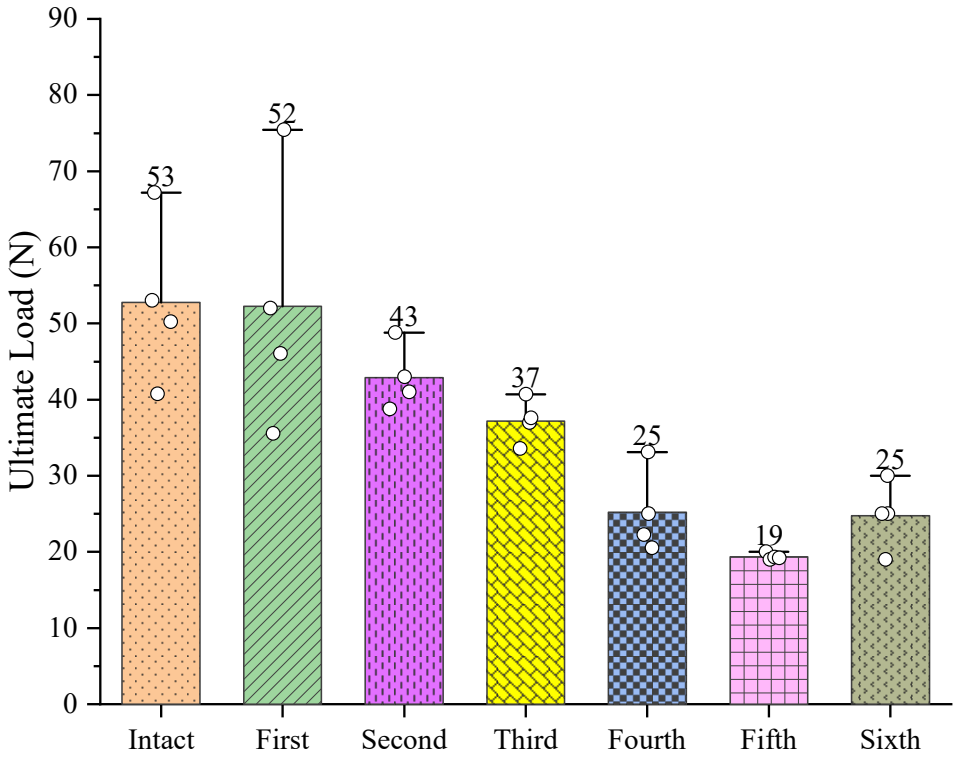

Figure 4-20 Self-healing properties of ECM. (A–D) Single-edge notch sand slurry beams with a constant dimension of the notch (2:5 by depth) were prepared (A: before, and B: after test). The fractured sample was placed in the silicon mold and treated with the calcium-enzyme solution. Ultra pure CO_2 gas was sprayed along the crack region (C). After treatment, the crack was healed (D). The middle row shows the healed samples in the 3rd, 4th and 5th cycles. After desiccation, the white crystals can be viewed near the fractured region. The bar graph shows the ultimate load in each healing cycle.

4.4.9 Mechanism of Self-Healing

Figure 4-22 shows that the reconstructed self-healed structure of crystal gelatin on the substrate perpendicular to the crack surfaces has established effective crystal bridges. The SEM analysis of the samples shows that the major fracture mechanism is the failure of mineral

bridges. In the self-healing process, the bridges are reestablished after the application of CO_2 (Figure 4-22).

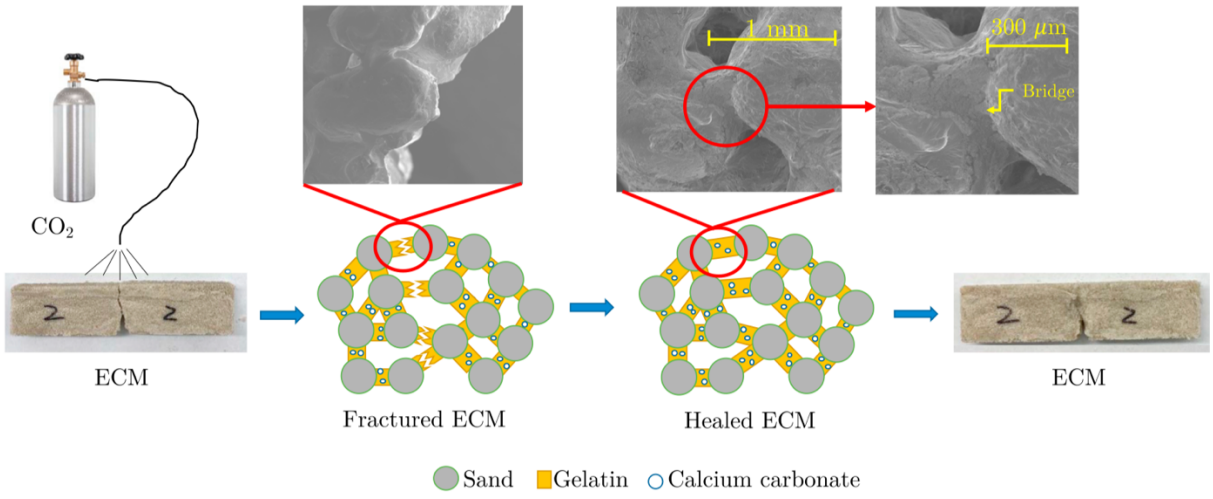

Figure 4-21 Mechanisms of self-healing in ECM. After the fracture, upon the application of CO_2, CA's enzymatic catalysis will reestablish the broken mineral bridges using calcium and CO_2 and reconstruct the bridging network that holds the materials' microstructure together.

We believe that the entire structural system on the fractured surface was not fully destroyed after the first fracture and that the original gelatin-calcium carbonate crystals remained on the surface of the exposed sand grains. From the second healing cycle, the gelatin on the surface of the sand is further dissolved by the aqueous solution, changing the structural integrity at the fractured surface. The reason for a stable maximum load after the fourth healing cycle is that the sand particles in the top layer on the fracture surface are exposed without gelatin, and then, those sand particles bridge directly to the calcite crystals. It must be noted that the titration solution will only permeate from one side to the bottom, which causes the gelatin to concentrate in the lower layer and in turn leads to the creation of non-uniform crystal bridge structures as the number of healing cycles increases. The results in Figure 4-17 show that the dehydrated gelatin

scaffold significantly contributes to the compressive strength of ECM, and so its deterioration weakens the strength of the specimens as the number of healing cycles increases. Moreover, gelatin aging could also occur during multiple healing cycles. In terms of crack length, there seems to be no healing limitation, as medium-scale samples (~1.0 in width) were tried in this study. However, the two sides of the samples need to be placed close to each other for the crystals to grow to heal the sample. This limitation shows that there is a crack width limit in the proposed healing mechanism (less than about 1 mm).

4.4.10 Compressive strength of coarse sand ECM

Uniaxial compressive experiments were performed following the ASTM [104] on ECM specimens with coarse sand (NO. 30, the sand retained on a 600 μm sieve as alternative sand mixing in the materials), since this possessed the highest compressive strength compared to intact and high pH specimens in the fine sand formulation. The average strength of coarse sand ECM is 4.2 MPa, which is lower than fine sand ECM in Figure 4-23. The primary reason for these differences is that compressive strength in these samples is predominantly influenced by larger sand aggregate strength, size, and distribution than the size of crystal bridges.

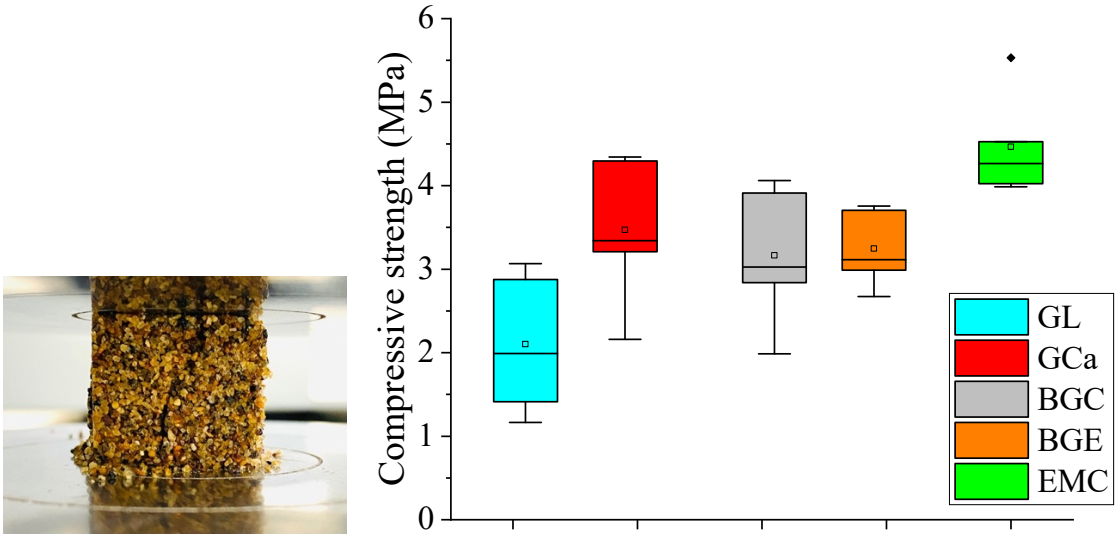

Figure 4-22 Compressive strength of coarse sand slurry samples. ECM has highest average compressive strength 4.2 MPa among all the presented materials.

4.4.11 Fracture test of coarse sand ECM

The results of the three-point fracture experiments are presented in Figure 4-24. The fracture experiments used the method in ASTM standard [105]. A cured silicone mold with a sharp crack was prepared and used for sample preparation. A four-part solution of 10 μL CA enzyme, tris base, 2M calcium chloride dihydrate and DI water was prepared. It was then thoroughly mixed for two minutes and bubbling CO_2 gas for 10 minutes. The solution was then titrated on the coarse sand samples and settled for half hour until fully infiltrated into the sand. The samples were then placed in the $100°C$ oven for 24 hours and demolded afterwards. Fracture toughness were then calculated following the fracture experiments. The results show that the coarse sand ECM sample has the highest average fracture energy of about 48 N/m.

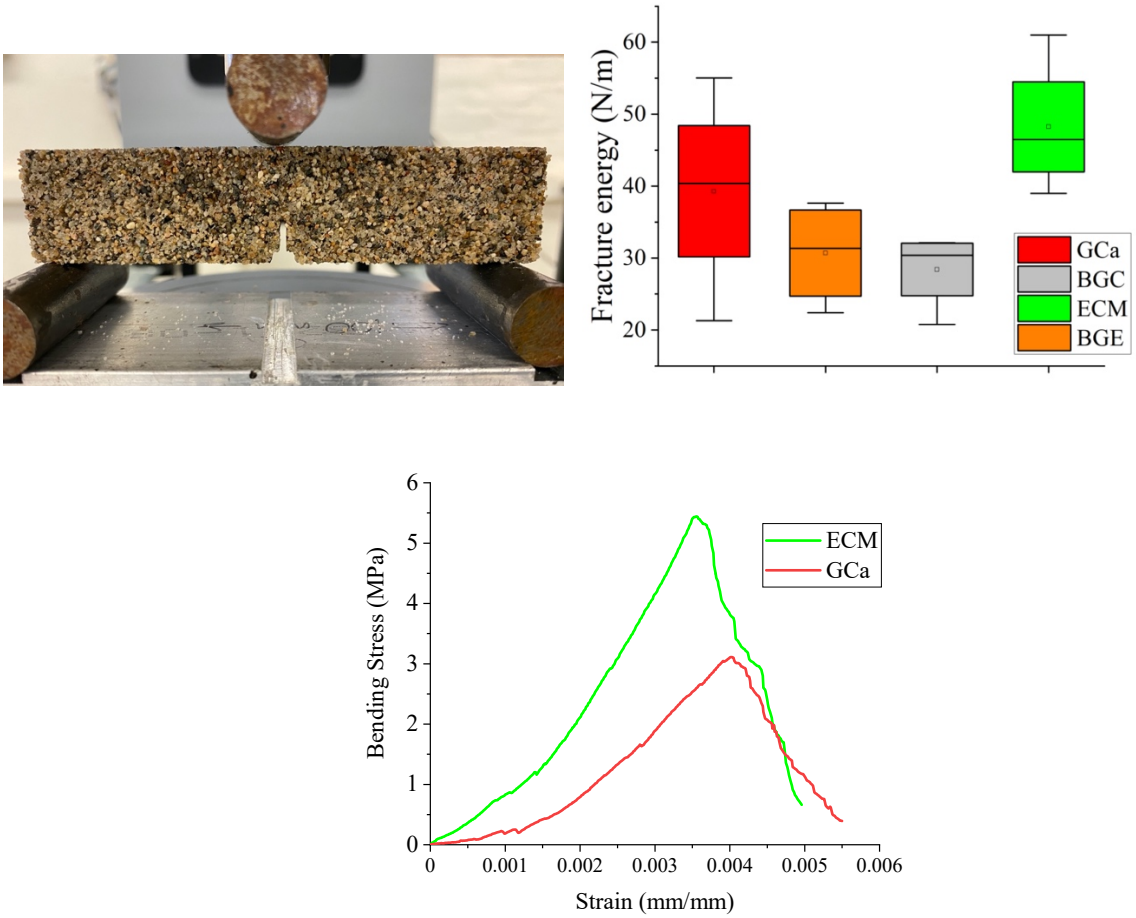

Figure 4-23 (Top) Results of the fracture energy experiments for coarse sand slurry beam. (Bottom) Stress-strain plots corresponding to coarse sand beam bending test.

4.4.12 Reinforced ECM

To enhance the physical properties of gelatin, researchers have previously applied many crosslinking agents such as glutaraldehyde, genipin, and microbial transglutaminase [106-109]. Here, glutaraldehyde was chosen as the ECM-crosslinking agent, since it is widely used because of its accessibility, low cost, and high efficiency of collagenous material stabilization [110]. Very low concentrations of glutaraldehyde (1% by gelatin weight) are sufficient to obtain a 100% degree of crosslinking and a 20-fold increase in Young's modulus with respect to uncrosslinked

gelatin film. The crosslinking of gelatin with glutaraldehyde involves the reaction of the free amide groups of the lysine or hydroxylysine in the polypeptide chain with the aldehyde group of glutaraldehyde [111] As the degree of crosslinking increases, the thermal and mechanical properties of gelatin can also increase. Tannin can also be added to improve the mechanical, thermal, and moisture absorption of the gelatin-based adhesives [112, 113] and can increase the bond strength (tensile) by 16%. Here, we also compared the compressive strength results of ECM and glutaraldehyde with ECM and tannin. The details of the experimental procedure of glutaraldehyde- and tannin-reinforced ECM are presented in the section 4.3.8. Figure 4-25 displays the compressive strength of glutaraldehyde-modified ECM at around 11.5 MPa, which is 28% higher than that of the ECM. Meanwhile, tannin modification (27% by gelatin weight) of ECM samples failed to reinforce the ECM structure. Although glutaraldehyde is an irritant, thousands of successful bioprosthetic implants have demonstrated that glutaraldehyde crosslinking is clinically acceptable [114, 115], reducing its cytotoxicity when used at very low concentrations.

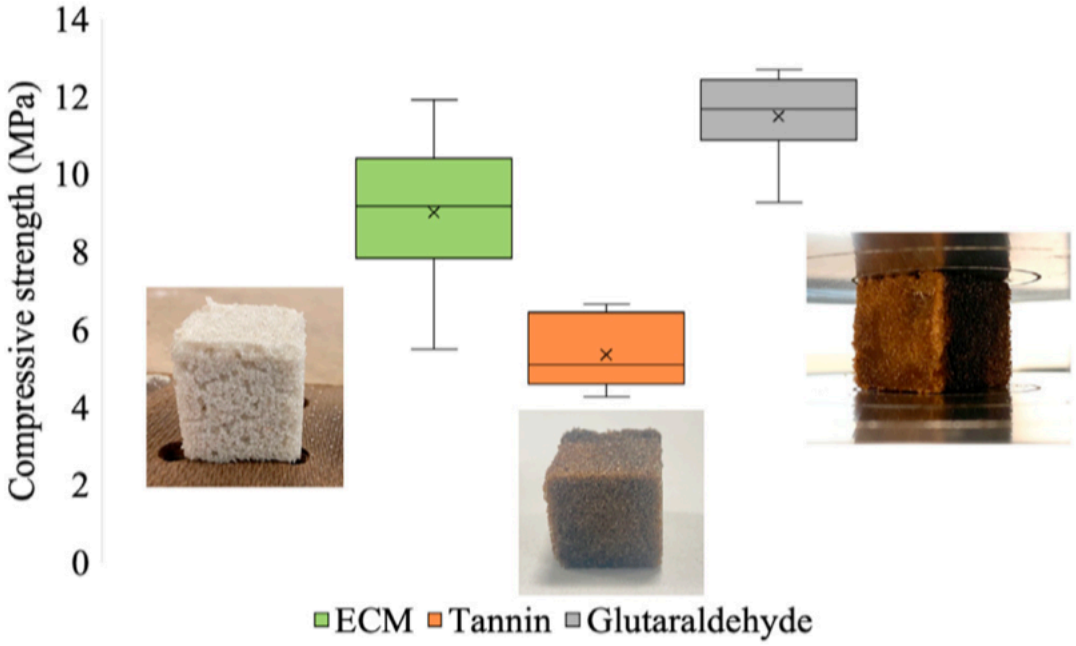

Figure 4-24 Cross-linking agent-modified ECM The compressive strength of glutaraldehyde-modified ECM and tannin-modified ECM is presented. Setting the compressive strength of ECM as the control group (statistical significance versus control: ECM: n = 14, M = 9.02, SD = 1.95; glutaraldehyde-modified ECM: n = 7, M = 12.1, SD = 1.19, p = 0.003; and tannin-modified ECM: n = 5, M = 5.36, SD = 1.07, p = 0.0005). Glutaraldehyde-modified ECM samples exhibit a 12-MPa strength on average.

4.4.13 Proper life cycle assessment of ECM

The main component in the structure of ECM after sand, is calcium carbonate, $CaCO_3$. The process of $CaCO_3$ crystal precipitation consumes CO_2. Referring to Equations 3-1 and 3-2, there is no gas emission from the whole reaction. CO_2 is the only compound consumed continuously from the environment, and $CaCO_3$ is the only solid product. Hence, it is reasonable to assume the process has negative emission. The lack of emission due to the production of other ECM components are as follows: Carbonic anhydrase, which is added in trace amounts, is isolated from bovine erythrocytes through a process which does not generate carbon dioxide and requires little energy [116]. Calcium can be obtained from natural brines as a by-product from synthetic soda ash production [117]. Another method produces calcium from hydrochloric acid and limestone. The process will generate hydrogen that can be directly burned or generated by fuel cells to obtain water, which can be achieved by true zero carbon emission without polluting the environment. Gelatin is extracted by hydrolysis of biological material in a process that is essentially zero-emission [118].

4.4.14 Scaling-up the production of ECM as building material

ECM production has a wide range of possible environmental conditions and requires only simple manufacturing processes. Its components can be easily mixed together. The availability of components is not expected to limit ECM production, as the major component - fine and coarse sand - is abundant worldwide. A source of calcium is necessary for ECM production and can be obtained from natural brines as a by-product of synthetic soda ash production or from hydrochloric acid and limestone. Therefore, the calcium source is not expected to significantly limit ECM production. Trace amounts of carbonic anhydrase are required for ECM production, which can be mass-produced by isolating it from the blood of bovine or other species or from bacterial sources in large vats similar to beer production. As CA is an enzyme, it remains in the material and generates calcium carbonate crystals if CO_2 and calcium are present [119].

4.4.15 Interface Adhesion analysis

We first attached a monodisperse of 5-μm particles on the sample holder. sufficiently far from the surface with negligible adhesion effects. The maximum (pull-off) force measured using this technique for the 5-μm calcite particles in monodisperse systems is of order 10^{-7} N, see Figure 4-25. The energy associated with detaching the 5-μm particle from the substrate is characterized as the total area between the zero-deflection line and the force–displacement curve, see Figure 4-26. Based on the Derjaguin–Muller–Toporov (DMT) model [120], which applies to stiff materials with weak long-range adhesion forces and small cantilever tip radius, the adhesion energy was therefore calculated from:

$$\gamma = F_{DMT}/2\pi R, \qquad 4\text{-}12$$

where, F_{DMT} is the adhesion force from the AFM experiment and R is the combined reduced radius of the tip and calcite particles, which is presented as $R = \frac{R_1 R_2}{(R_1 + R_2)}$, R_1 is the radius of silica bead and the R_2 is the average radius of calcite particles.

The Hertzian analysis is a commonly used method for studying the adhesion behavior of atomic force microscopy (AFM) probes with the surface of a sample. This analysis is necessary because the adhesion force between particles is often non-linear and complex, making it difficult to interpret the data obtained from AFM experiments. Hertzian analysis of contact area was calculated respectively between the sphere and a flat surface, sphere and sphere see Figure 4-25. Stresses formed by the contact of two radii can cause exceptionally high surface stresses. The Hertzian Contact stress equations are commonly utilized to determine the maximum amount of stress that can be generated. Subsequently, these stresses are analyzed in study of the nano-to-micro scale contact. Following by Equation 4-13, which gives the equation for calculating the radius of the contact area produced by the deformation of the two spheres from force F, where R_1, E_1, v_1 is the radius, elastic modulus, and passion ratio of the top sphere. We only consider the van der Waals force between calcium carbonate and silica, see Figure 4-4, the Hertzian contact area is computed to be approximately 667 nm^3, please noted the v_1 = 0.17; v_2 = 0.3; E_1= 73100 N/mm^2 and E_2= 88197 N/mm^2, and the theoretical adhesion is calculated based on the Van der Waals forces (13.9 nN*nm) between macroscopic objects, see equation 4-14, where A is the Hamaker coefficient of $CaCO_3$ from literature [121]. R1 and R2 is the radii of two spherical bodies and z is the center-to-center distance. The area of unit molecule of calcium carbonate can be calculated by unit cell, which is around 0.28 nm^3[122]. Base on the Hertzian contact area, the total theoretical adhesion can be calculated around 32 nN. If assume the contact area is a flat surface, the R_2 in equation 4-13 can be considered infinite for contact sphere against the flat

surface. Hertzian contact area was computed around 772 nm^3 and the theoretical adhesion is around 36 nN which is in a good agreement with the experimental results, at approximately 27 nN.

$$a = \sqrt[3]{\frac{3 \cdot F}{8} \cdot \frac{\frac{1-v_1^2}{E_1} + \frac{1-v_2^2}{E_2}}{\frac{1}{2 \cdot R_1} + \frac{1}{2 \cdot R_2}}} \quad \text{4-13}$$

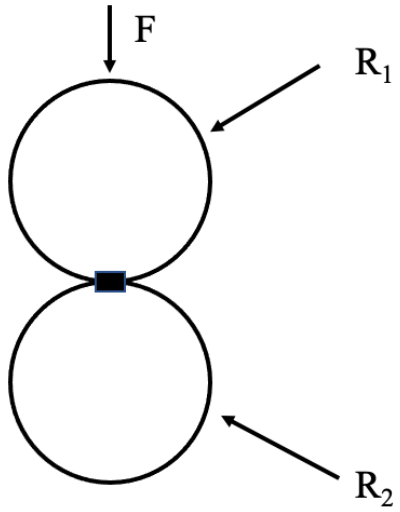

Figure 4-25 schematic diagram of spherical contact between silica and crystal.

$$F_{\mathrm{VdW}}(z) = -\frac{A}{6} \frac{64 R_1^3 R_2^3 z}{[z^2 - (R_1 + R_2)^2]^2 [z^2 - (R_1 - R_2)^2]^2} \quad \text{4-14}$$

A real mineral crystal that grows successfully from the substrate always involves the binding reaction between the functional group of substrate and mineral at the molecular level. The generation of a covalent bond or hydrogen bond between two interfaces can be considered as the type of crystal growth. Surface modification plays a crucial role in the interfacial bonding

behavior of materials. In the absence of surface modification, the attachment of calcium carbonate crystals to the sand and scaffold surface may rely primarily on physical interlocking mechanisms, although the potential for additional chemical reactions cannot be ruled out. Further research is required to elucidate the crystal growing mechanisms underlying the initiation of the nucleation site. Understanding the existing surface mechanisms is essential to enhance the strength and durability of materials. Figure 4-27 shows the cross section interface between calcite crystal and sand after FIB cutting. A 20 nm width of the gap is exposed between calcite and sand, which is considered created by the high energy of ion beam cutting. Part of the calcite crystals grows from the sand particle surface nucleation sites instead of deposition can be explained for three reasons: 1) the EDS map clearly shows the distinct different components on both sides of the gap. The top area is calcite, and the bottom side is silica, see Figure 4-27 d. 2) Calcite typically occurs in a variety of shapes, including rhombohedra, scalenohedral and prisms. However, the gap between crystals and sand is tended to be a straight line. We found out the gap fits perfectly on the edge of the sand surface and this phenomenon statistically occurs between most calcite crystals and sand particles. 3) Figure 4-27 displays a comparison between crystals deposit (left) and growing (right), the gap created by deposition is from 500-1000 nm much larger than the gap from growing condition ~20 nm. A 20 nm width of the separation is exposed between calcite and sand, which is considered a thermal expansion and differential stress created by the high energy of ion beam cutting. The calcite particles with flat-bottomed contacts with the silica substrate. This could result from the recrystallization of a particle pressed down on the surface by surface tension and Van der Waals forces, leading to dissolution at contact points and reprecipitation in places away from the contact point where the calcite is unstrained and not in a higher-energy state of deformation. The higher contact area due to the recrystallization leads to a

higher interface strength between calcite and sand. Please noted that van der Waals forces could be the major mechanism between calcium and sand surface and the surface roughness can diminish the force by several orders of magnitude, which will fully verify by AFM in the future. The next stage will also study the interaction mechanism between sand-scaffold, calcite-scaffold.

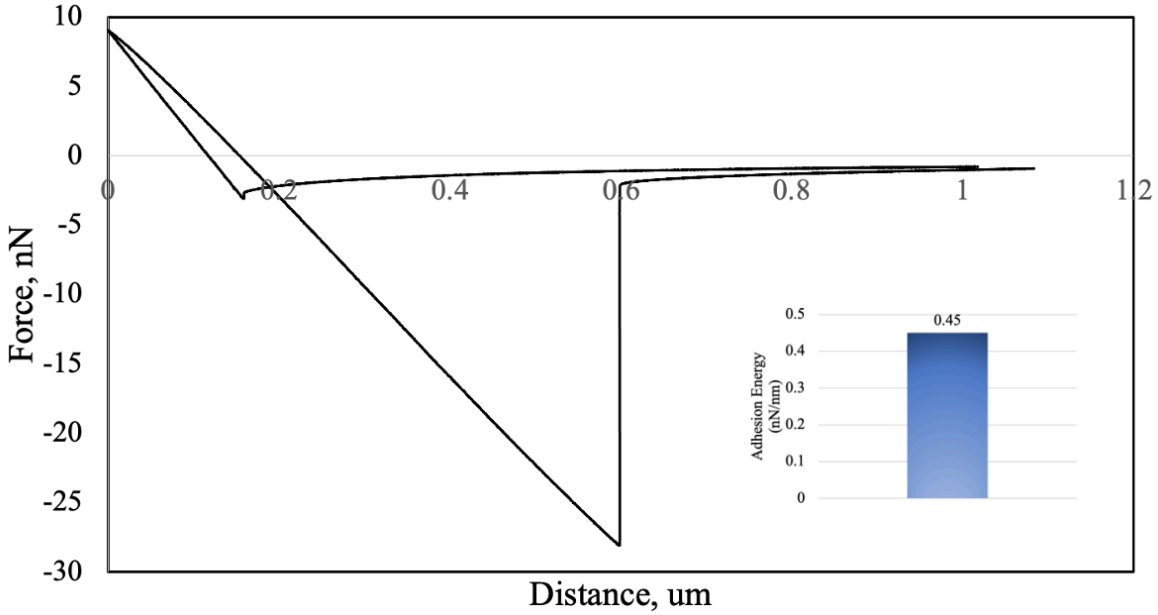

Figure 4-26 The adhesion between silica and polydisperse calcium carbonate crystals was measured with AFM using single force mode technique. The force displacement curve of attached silica particles cantilever tip approaching the substrate with calcium carbonate particles, and the adhesion energy was calculated by the Derjaguin–Muller–Toporov (DMT) model.

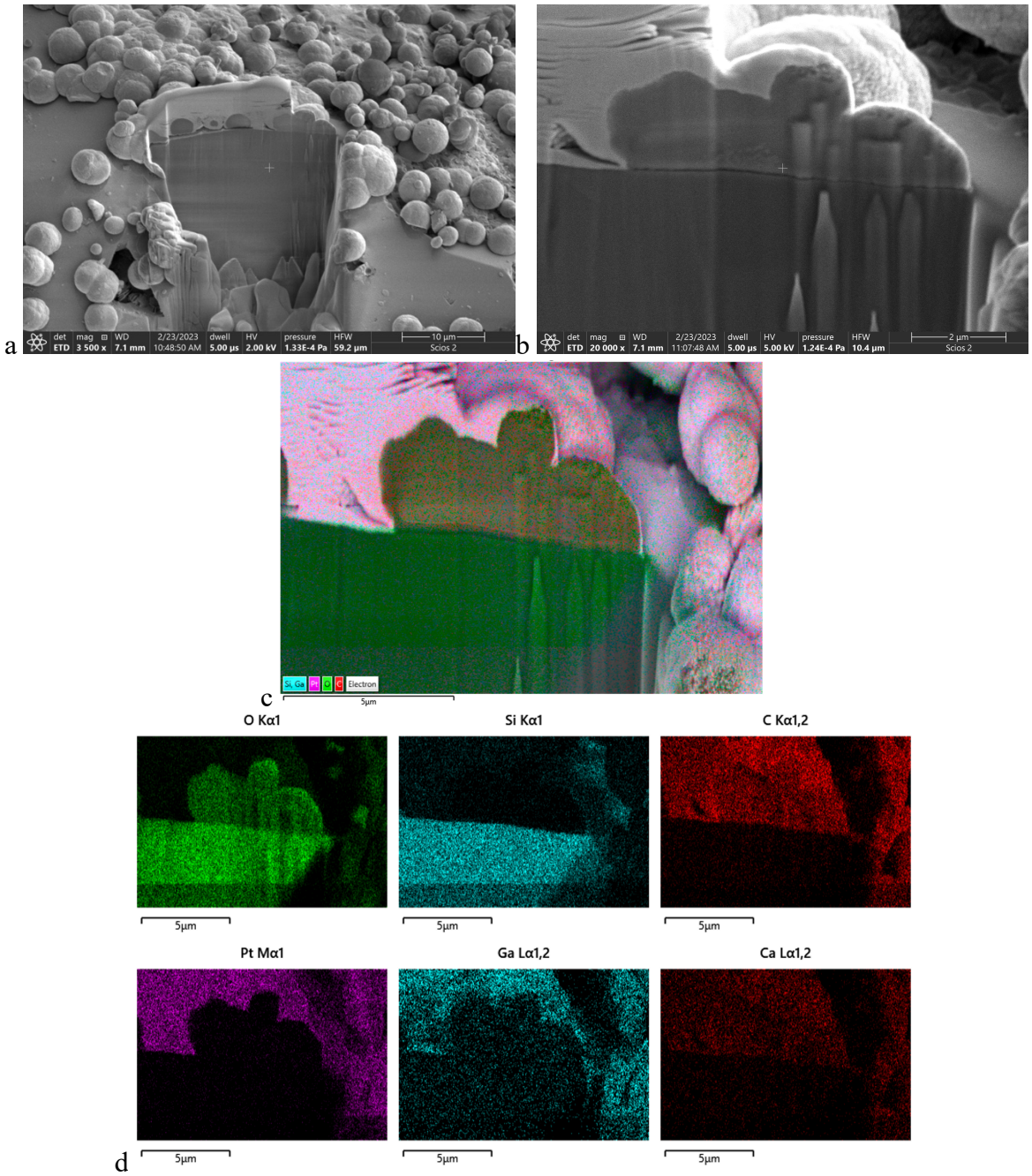

Figure 4-27 FIB-SEM images of sand-calcite interface cross-section within ECM sample. a) The cross section was exposed after Focused-ion-beam (FIB) milling and a layer of protective platinum (Pt) covered on the top of the crystals surface. b) The closer view of backscattered electrons (BSE) image showing the single calcium carboante crystal grows from the silica

surface. c-d) The energy dispersive spectroscopy (EDS) mapping showing the microstructure and elements on the interface between calcite and sand.

4.3.16 Water resistant agent coating on ECM

Coating a hydrophobic layer agent on the ECM surface can significantly increase the durability of ECM. The ECM cubes were coated with contact cement adhesive and air dry for 24 hours. Immersing the coated ECM in water at room temperature for a week, the coated ECM still performs a similar strength. Using silicon gel to coat ECM is hard to achieve the same water resistance with contact cement adhesive. The silicone gel is more viscous and is difficult to cover every void on the ECM surface. The contact cement adhesive seems a promising method to increase the durability of ECM under high humidity, however, when the coating layer is destroyed or cracked will expose ECM to air again, especially if the interior surface is exposed would create a difficult in recoating.

Figure 4-28 Fully dehydrated ECM samples were coated with WELDWOOD Original Contact Cement (yellow) and GE Advanced Silicone (white).

4.4.17 Clay type ECM

The enzymatic method was proposed to apply on red clay to evaluate the compressive strength. The red clay is added in the 1-inch cubic silicon mold and piped 7 mL CA enzyme calcium solution throughout the clay (the solution preparation is described in 4.3.1 and 4.3.2 . Spraying CO_2 gas on the sample surface with a constant rate for 15 minutes. Stabilized sample for 30 minutes and cured in the 80 C oven for 24 hours. The method of type 2 sample is mixing red clay with CA enzyme calcium solution directly for 2 minutes and then poured into the 1-inch silicone mold. The CO_2 gas was sprayed on the surface for 15 minutes. The compressive strength of Enzymatic type 1 clay samples shows significant different from clay samples without enzymatic method by an average 3 MPa. And the type 1 sample preparation both show a higher compressive strength than type since the former density of materials is higher and water molecules bridge most of the clay particle by capillary force and electric force instead of calcite physically anchoring force before dehydration.

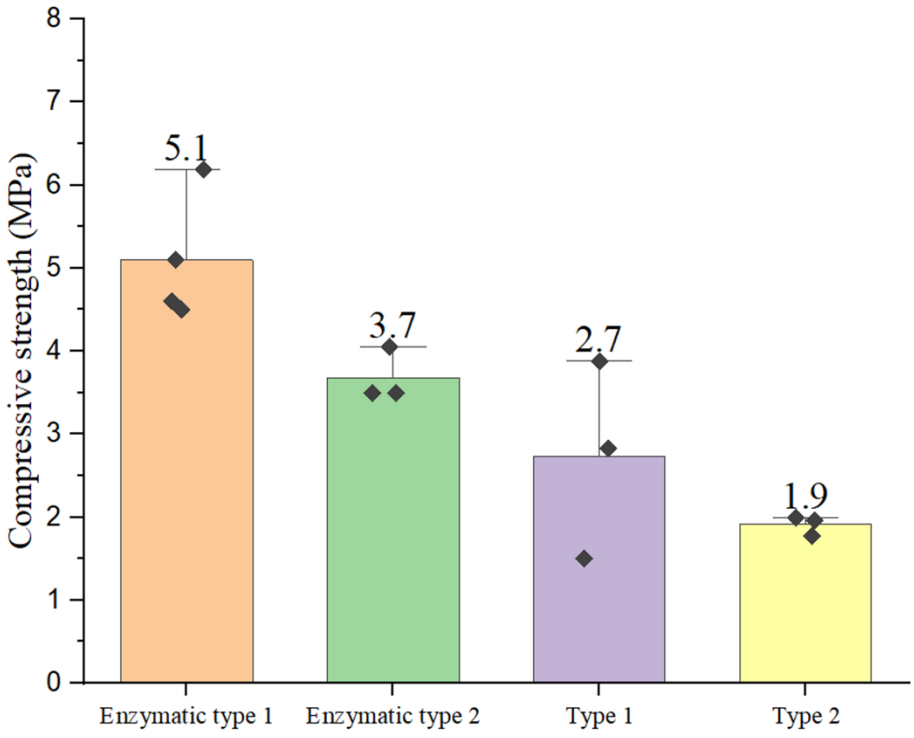

Figure 4-29 Top, the overview of 1 inch clay type ECM block. Bottom, the compressive strength of different clay samples. Enzymatic type 1: CA enzyme and calcium solution added to the clay ~ 5.1 MPa. Enzymatic type 2: CA enzyme and calcium solution mixed with clay ~ 3.7 MPa. Type 1: water added to the clay ~ 2.7 MPa. Type 2: clay mixed with water ~ 1.9 MPa.

4.5 Summary and Conclusion

This study introduces a new paradigm in developing a negative-emission construction material with self-healing capability using sand, calcium, gelatin, and a trace amount of CA, named ECM. We have shown that ECM possesses outstanding mechanical properties as a construction material, with compressive strength (~12 MPa) higher than any other available method and is more than twice as high as the minimum acceptable strength for cement mortar, and which provides a pathway to repair or even replace Portland cement concrete in the future. Experiments investigating the contribution of CA enzyme catalysis, high pH condition, and gelatin, along with studies focusing on underlying crystal growth, all show that wider and longer mineral bridges are incorporated into the microstructure of ECM compared with materials without enzyme and/or base to give a strong and tough construction material. We also show that ECM is a living material capable of self-healing for six cycles of fracture.

We have shown that the enzymatic mineralization method has great potential for the creation of negative-emission construction material and can be a viable method for carbon sequestration. ECM can be rapidly manufactured with an environmentally friendly procedure that makes it possible to be a substitute for current building materials.

4.6 Future work

This promising technology is still at the initial stage, optimizing the catalytic efficiency of enzymes, the property of scaffolds, and the mechanics of crystal structure should be considered for future work. ECM can be produced under a wide range of environmental conditions with only simple manufacturing requirements. Components can be directly added together and mixed. ECM production is not expected to be limited by the availability of its components. The major component of ECM is fine and coarse sand which is available throughout the world. ECM

requires a source of calcium which can be provided by a calcium source that can be obtained from natural brines as a by-product of synthetic soda ash production. It can also be produced from hydrochloric acid and limestone. Thus, ECM production would not be significantly limited by calcium source. Finally, ECM production requires trace amounts of carbonic anhydrase. Because CA is an enzyme, it is not consumed in the reaction but remains in the material to generate calcium carbonate crystals if CO_2 and calcium are present. CA can be mass-produced by isolation from the blood of bovine or other species or from bacterial sources in large vat analogous to beer production [114].

4.6.1 The kinetics of $CaCO_3$ precipitation through CA catalysis

The kinetics of spontaneous precipitation of $CaCO_3$ from enzymatic solution is suggested investigated by recording pH as a function of time. Raman spectroscopy should be applied as the real-time in situ tool to track the calcite forming kinetic from the nuclei. In the presence of CA, the induction time for $CaCO_3$ nucleation should be decreased, but does not affect $CaCO_3$ polymorphism. The surface free energy should be determined based on the classical nucleation theory in the future. The equation is provided in the equation 4-12, where the R is represented the rate of nucleation, N_S is the number of nucleation sites, j is the rate at which molecules attach to the nucleus, Z is the Zeldovich factor, $\Delta G^*$is the free energy cost of the nucleus at the top of nucleation barrier, $k_B$is the Boltzmann constant and T is the absolute temperature. To study this topic, we should focus on the degree of heterogeneous nucleation change with the concentration of CA.

$$R = N_S Z j exp\left(-\frac{\Delta G^*}{k_B T}\right) \quad 4\text{-}12$$

Chapter 5

Chapter information: Shuai Wang, Suzanne Scarlata, Nima Rahbar, Curing and self-healing of enzymatic construction materials using nanoparticles, Cell Reports Physical Science, Volume 3, Issue 9, 2022, 101039, ISSN 2666-3864, https://doi.org/10.1016/j.xcrp.2022.101039.

5 Advanced Enzymatic Construction Material (ECM-n)

5.1 Abstract

Preparation of construction materials on site may offer advantages in transportation and storage. However, a major limitation of on-site preparation of some materials is the need for heat and oven desiccation for adequate curing. Here, we describe a method that allows rapid curing under ambient conditions through the addition of 0.1% iron oxide nanoparticles to a carbon-negative enzymatic construction material (ECM) to make ECM-n. Specifically, we show that a low-power laser (3W at 808 nm) can cure ECM-n to an optimal mechanical strength in 12 h, which can be compared to the 14-day period needed for in situ air drying. In addition, the incorporation of nanoparticles allows rapid self-healing of large-scale flaws and that incandescent light can be used if lasers are not available. This method establishes an on-site manufacturing capability for ECM-n and other construction materials and supports thermal controllability of the local structure in low-temperature regions.

Keywords: structural materials; construction materials; laser heating; curing; nanoparticles; self-healing; enzymatic; durability

5.2 Introduction

Global carbon emissions have grown rapidly since the 21st century and have become one of the main contributors to the greenhouse effect, leading to the rapidly fluctuating weather patterns that accompany global warming. Concrete is the most used material on the planet, and its manufacturing accounts for 8% of human-made global carbon emissions [123, 124]. It has been reported that each kilogram of concrete production releases 0.65–0.92 kg carbon dioxide based on a cement plant with modern technology and equipment [125, 126]. For these reasons, we have recently developed a concrete substitute that sequesters rather than generates CO_2. This sand-based material, coined enzymatic construction material (ECM) contains an enzyme called carbonic anhydrase (CA), which catalyzes carbonation and accelerates calcium carbonate precipitation in a process that consumes CO_2. The enzyme generates large quantities of crystals that bridge with natural sand, resulting in a solid material with outstanding compressive strength [127]—three times higher than the minimum acceptable for cement mortar [128] and other biological building materials [129, 130]. Also, the self-healing ability of ECM was shown in our studies where the material was fractured and healed six times. This ability to self-heal makes ECM practical and durable in environments where the material is subjected to freeze-thaw cycles.

Traditional concrete curing properly requires an adequate amount of moisture for continued hydration and 28 days to achieve mechanical strength [131, 132]. Compared with concrete, ECM obtains maximum compressive strength in 24 h by oven heating or >1 week under natural desiccation. However, to reduce the time cost, the application of an oven certainly makes the on-site construction challenging. Here, we show that adding a trace amount of iron oxide nanoparticles to ECM generates an improved material called ECM-n that is easily cured

with a low-power laser, or incandescent light (the curing incandescent light experiment set up can be found at support information, Figure 5-15). This method, based on studies of laser-induced nanoparticles application in hyperthermia therapy [133-136] uses the exothermic behavior of iron oxide nanoparticles under external electromagnetic (radiofrequency, microwave, and laser) excitation. Specifically, we show that the ECM-n samples cured for 12 h under a 3W laser (808 nm wavelength) have compressive strength similar to that of ECM. In addition, fabricating large flaws in ECM-n samples showed accelerated repair with laser exposure and the samples regained mechanical strength and properties comparable to original, flawless samples. Our method is supported by studies describing surface temperature profiles during curing and post-curing and the distribution of nanoparticles in ECM-n samples. Complimentary numerical analyses of heat transfer under laser support the experimental results, which reveal the underlying thermogenesis mechanism. While the studies focus on the sand-based ECM-n, our method can be generalized to other materials that would benefit from rapid on-site curing.

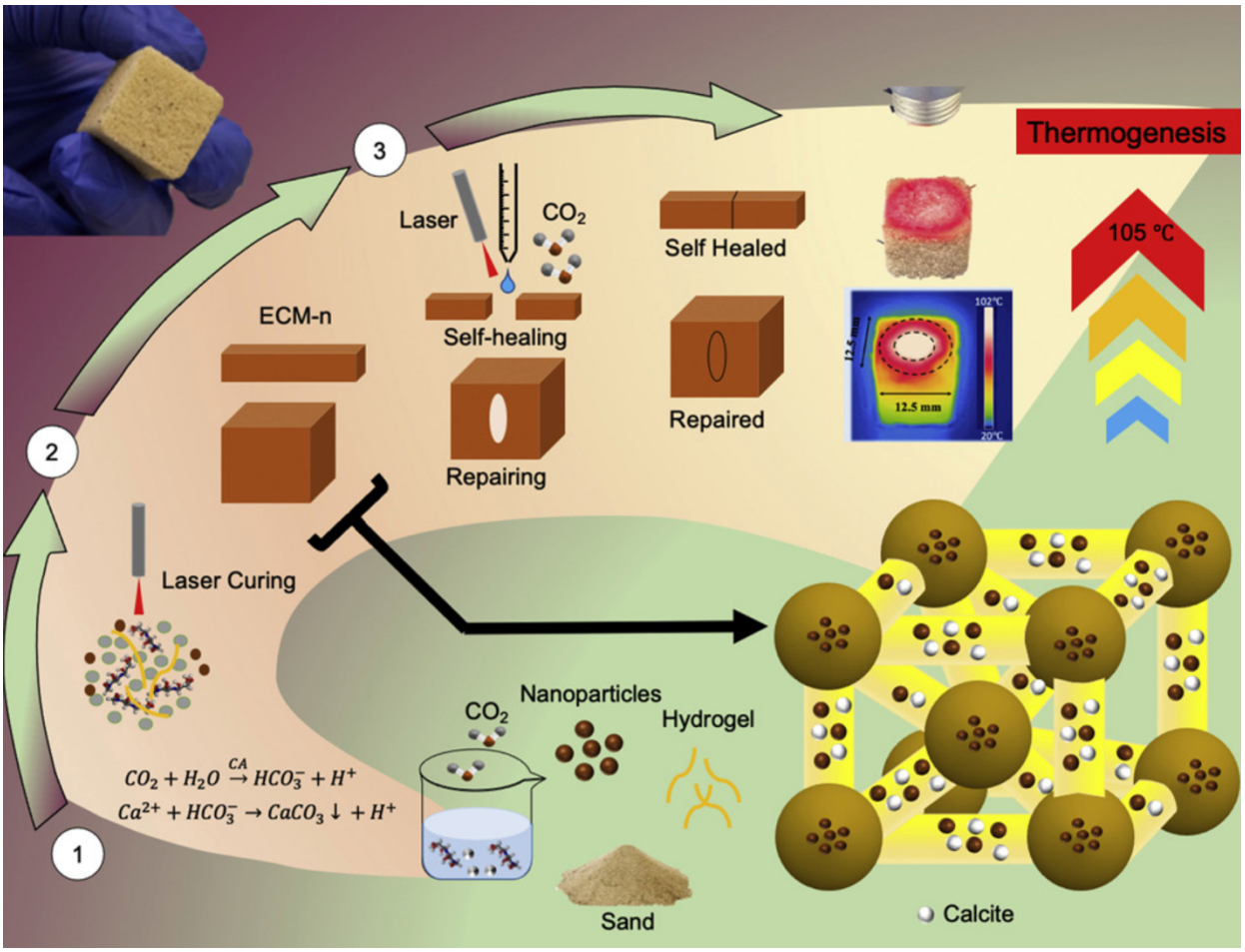

Figure 5-1 Schematic diagram showing the construction process of ECM-n and its curing, self healing and repairing concept by low power laser.

5.3 Materials and methods

The ECM-n was fabricated in the top-to-down approach, as was the ECM for the entire study. The iron oxide nanoparticles (Fe_2O_3, gamma, high purity, ≥99.5%, 20 nm) were purchased from US Research Nanomaterials (Houston, TX, USA). It was selected because of (1) its ultra-high thermal conductivity and (2) the size of the nanoparticles could easily fit in the void within the ECM structure. The Photon 3W Dental Diode Laser (Zolar Technology and Manufacturing, Mississauga, ON, Canada) was chosen in this study, which emits an infrared laser light

beam (λ = 808 nm). The FLIR One iOS Pro-Grade Thermal Camera was used to measure the temperature of the heated surfaces of the samples.

5.3.1 Medium solution preparation

CA at 10 μL at a 100-μM concentration was stored in $-20°C$ until use in the experiment. A 0.1-M Tris solution was added to 200 mL of deionized (DI) water, and 10 μL of CA was added to the beaker to create the enzyme buffer solution. A 2-M $CaCl_2$ solution in 200 mL of DI water were well mixed on the stirred plate for 2 min and cooled down to $30°C$ because of the exothermic reaction between calcium chloride and water. The enzyme buffer and $CaCl_2$ solution were combined in an Erlenmeyer flask to mix for additional 2 min. CO_2 gas was aerated into the flask at the rate of five bubbles per second. The foggy solution can be observed within 5 min, when the calcite crystals were catalyzed and formed small particles in the solution. The experiment ended by stopping the flow of CO_2 gas at the 15th minute.

5.3.2 ECM-n fabrication

For the preparation of ECM-n, a 10% (g/mL) gelatin by solution matrix was mixed thoroughly with number 50 (the sand retained on a 300-μm sieve) white sand and filled the 12.5-mm 3-dimensional (3D) printed silicon cubic mold. Iron oxide nanoparticles (0.1% by sand weight) were added to the enzyme-calcite solution (0.27 mL/g, solution volume/sand weight) by using an ultrasonic bath for 1 min and then quickly mixing for 30 s manually. The ultrasonication ensured that the nanoparticles were distributed homogenously in the mineral solution. Afterward, the solution was poured over the sand slurry matrix and vibrated for 2 min before laser curing. This procedure was used for obtaining a further distribution of nanoparticles

in the sand slurry system, where the viscosity of the hydrogel avoids the agglomeration of nanoparticles.

5.3.3 Laser-induced curing of ECM-n

The laser diode corresponds to a heating power of 3W. The laser beam was transmitted through a fiberoptic cable to the tip of a cylindrical probe before propagating into the sample. The distance between the tip of the probe and the sample surface was set at 2 cm to achieve a laser spot size of 1 cm on the samples. The temperatures of the heated surfaces of samples were recorded with an infrared camera (FLIR One Pro). Subsequently, the 12.5-mm cubic sample was heated and dehydrated in the silicon mold for 12 h. The cuboid samples (38 mm in length, 8.3 mm in depth, 4.1 mm in width, and 1.1 mm in notch length) were fabricated in the same method. Due to the limited size of the laser beam, the cuboid sample was spotted at three different locations (left, center, and right) for 5 h at each point to achieve a fully dehydrated specimen.

5.3.4 Heat Released Analysis During the Initial Curing

Isothermal Titration Calorimetry (ITC) can measure the thermal power (heat production rate) produced by the hydration reactions of cementitious materials. [137, 138] Additionally, ITC tracks the rate of the overall reaction of the material and visualizes the behavior of the hydration in a way that a simple set time or a compressive strength test does not. The timing and shape of the heat flow curve obtained by calorimetry indicate the relative performance of concrete and potential adverse interactions between materials used in the mixes [139].

5.3.5 Laser Heating ECM-n In Low and Room Temperatures

All the physical and thermal properties of the ECM-n sample were extracted from experimental data to be used in the FEM. The geometry of the ECM-n was modeled with standard 8 node linear heat transfer elements in three dimensions, which is shown in Figure S3a. To develop multi-functional properties of ECM, we investigated the laser thermal mechanism and heating process in ECM-n, and simulated the temperature gradient, assuming the material properties are not temperature-dependent since there is no phase change during the heating process. Figures S3c&d present the highest temperature profile located under the laser beam as a function of time, which agree with the experimental observations in Figures 3a-c.

5.3.6 Laser-induced self-healing of cuboid samples

The single-edge notch cuboid sample was fractured into two parts. The parts were assembled and placed into the original mold. A 1-mL (5 μL enzyme, concentration: 2.9 mg/mL) of calcium enzyme solution was added to the crack region. Ultra-pure CO_2 was introduced on the surface for 15 min to precipitate the calcite crystals and form a prototype of the bridges. The sample was then settled for another 15 min, allowing the mineralization solution to penetrate naturally into the interior of the structure. The 3W laser was set up 2 cm above the sample and conducted on the crack for 6 h; then, the sample was able to be taken out of the mold.

5.3.7 Repairing procedure for ECM-n

ECM-n were fabricated and cured in a 3D print silicone mold with an elliptical and circular shape notch. After heating with the 3W laser for 12 h, the sample was taken out of the mold and transferred to a cubic silicon mold. The notch was filled with well-mixed sand-gelatin

components, and the sample was then vibrated for 30 s A 200-μL calcium-carbonic anhydrate mixed solution with nanoparticles was added on the notched surface and then aerated by CO_2 for 15 min. This process should be slow enough to ensure that the solution penetrates to the bottom and does not affect the surrounding structures. A 3W laser was induced on the sample from the same distance on the repaired surface for 12 h and was finally taken out of the mold.

5.3.8 Mineralogical assessment of precipitates

The crystal and nanoparticles in ECM-n samples were segregated from the gelatin and sand matrix for assessment of the mineral phase in ECM-n after laser inducing for 12 h. Dried crystals and nanoparticle mixtures were ground with the mortar and smear mounted on a sample holder for fingerprint XRD. A Siemens D500 X-ray diffractometer analyzed the samples from to 70° 2θ using Cu K-α X-ray radiation with a step size of 0.02° and a dwell time of 2 s per step. Mineral phases were collected using a data collector. The laser-cured ECM-n was evaluated using JEOL JSM-7000F Analytical SEM Samples were first sputter coated with gold powder. EDS was used to assess the nanoparticle distribution in the ECM-n matrix.

5.3.9 Raman spectroscopy

A hybrid system (XploRA, HORIBA, Montpellier, France) was used to obtain optical images and Raman spectra ranging from 100–1200 cm^{-1}. The experiment was used with a diode laser (λ = 785 nm), and the filter was set up at 10% and 100× objectives. The acquisition time and accumulation were defined as 5 and 20, respectively.

Raman spectroscopy can provide qualitative analysis of sample phases and morphology, crystallinity, and molecular interactions. The peak profiles are generally defined by three

parameters: peak intensity, width, and position. The peak intensity is affected by object concentration and orientation. The peak width is related to crystallinity and homogeneity, and the peak position is associated with the components [140]. The carbonate phase (calcite) and gamma Fe_2O_3 comprise major portions of the material and are relatively easily identified through a phase ($\sim$1086 cm^{-1}) and Fe_2O_3 band ($\sim$225 cm^{-1}) since both are strong Raman scatterers.

5.3.10 Thermal modeling of laser heating

To further demonstrate the thermogenesis ability of the ECM-n, the computational laser heating was modeled using the finite element method (FEM) and the software package COMSOL Multiphysics 6.5 (COMSOL, Burlington, MA). The details of the thermomechanical modeling can be found in the supplemental experimental procedures, Table 5-1, and Figure 5-2.

Table 5-1 Nomenclature

Power, P	3 W
Laser beam radius, r	6 mm
ECM-n Thermal conductivity, k	2.7 W/ (Iron oxide, m·K)
Density, rho	1660 kg/m³ (Matter)
Heat capacity at constant pressure, Cp	840 J/(kg·K) (sand)
Hear transfer (convention) coefficient, h	25 W/(m^{2}K) (air)
Laser absorption coefficient	0.988 (Maria)
External temperature, T_{ext}	300 K
Surface emissivity, ε	0.95
Ambient temperature, T_{amb}	300 K

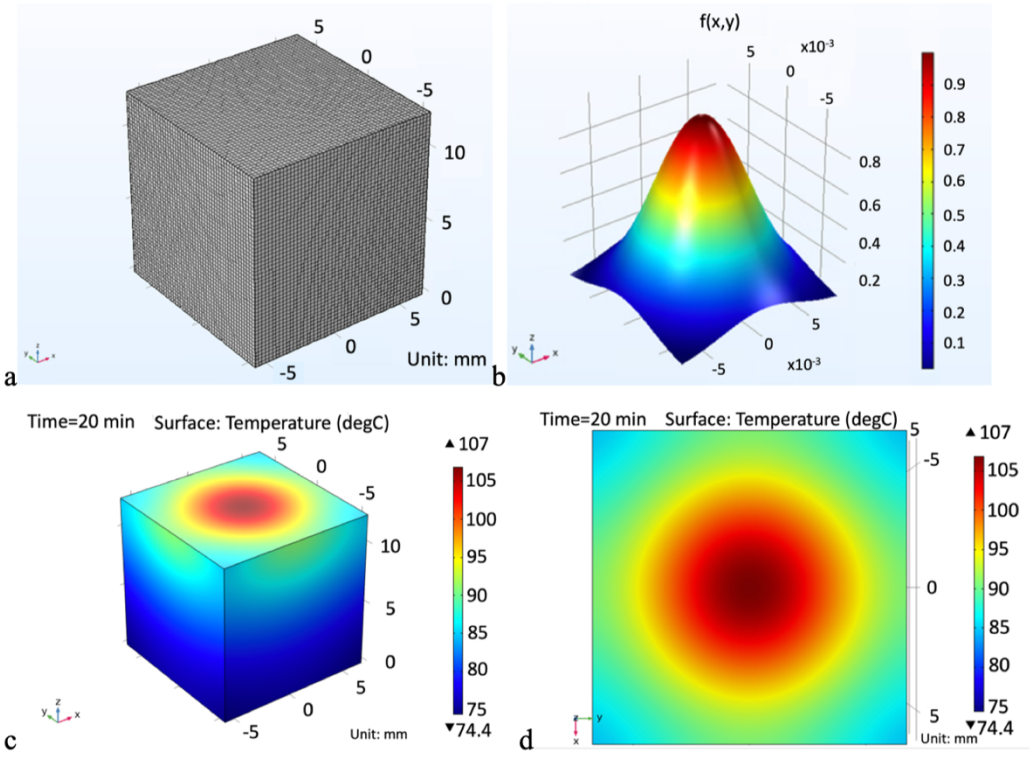

Figure 5-2 The thermomechanical modeling of ECM-n. The predicted three-dimensional temperature contour and the comparison of maximum temperature between experimental data and proposed prediction for ECM-n samples with different laser power. The heat transfer

computation was carried out for three different powers. a) The FEM mesh of ECM-n. b) Gaussian profile of order 1. c & d) The 3D and top views of the ECM-n showing the temperature contour at 20 minutes with a 3W laser illumination.

All the physical and thermal properties of the ECM-n sample were extracted from experimental data to be used in the FEM. The geometry of the ECM-n was modeled with standard 8 node linear heat transfer elements in three dimensions, which is shown in Figure 5-2a. To develop multi-functional properties of ECM, we investigated the laser thermal mechanism and heating process in ECM-n, and simulated the temperature gradient, assuming the material properties are not temperature-dependent since there is no phase change during the heating process. Figures 5-2c&d present the highest temperature profile located under the laser beam as a function of time, which agree with the experimental observations in Figures 5-2a-c.

5.4 Results and Discussion

5.4.1 Laser-induced curing of ECM-n

The composition of ECM (i.e., sand, gelatin, carbonic anhydrase) is extensively described in our previous publication. To verify the effect of nanoparticles on ECM curing rate, the 12.5-mm cubic ECM-n (ECM with 0.1% iron oxide nanoparticles) and ECM were fabricated using the same method and subjected to the same power laser. Both specimens were cured under a 3W laser (808 nm wavelength) for 12 h to obtain a specific degree of dehydration through mass loss evaluation (Figure 5-5A). As shown Figure 5-5B, the maximum surface temperature of ECM-n reaches 110°C in 12 h to obtain full dehydration, which shows a stable mass after 9 h. In contrast, the maximum surface temperature of ECM increases to only 62°C and maintains the mass loss condition. The surface temperature of ECM-n and ECM within the first curing hour

was recorded in Figure 5-3A–1D. Figure 5-3A shows the early curing configuration of a cubic 12.5 mm ECM-n in a silicon mold where the sample was placed under a 3W continuous wave laser (808 nm) at a 2-cm distance for 60 min, while the surface temperatures at the top and side were recorded by a thermal camera for 70 min. We find that the maximum surface temperature of the ECM-n sample increases from 26°C to 81.5°C (sample: n = 5, median: med = 81.5, SD = 3) (Figure 5-3B and 5-3C). In contrast, the temperature of all ECM samples without nanoparticles never rises above 60°C (n = 5, med = 53, SD = 5.7). The temperature distribution is non-uniform, with the maximum temperatures occurring within the center of the laser beam. From the temperature curves in Figure 5-3D, the heating rate of ECM-n is ∼2-fold higher in the first 20 min, the cooling rates of both were similar, reaching room temperature in 5 and 2 min, respectively, and giving a cooling rate of 11°C/min (n = 5, SD = 0.82) for ECM-n and 15°C/min for ECM (n = 5, SD = 1.63). These data indicate that the addition of nanoparticles does not significantly increase the specific heat capacity of ECM. Due to the low specific heat of nanoparticles, the nanoparticles accelerated curing by photothermal effect.

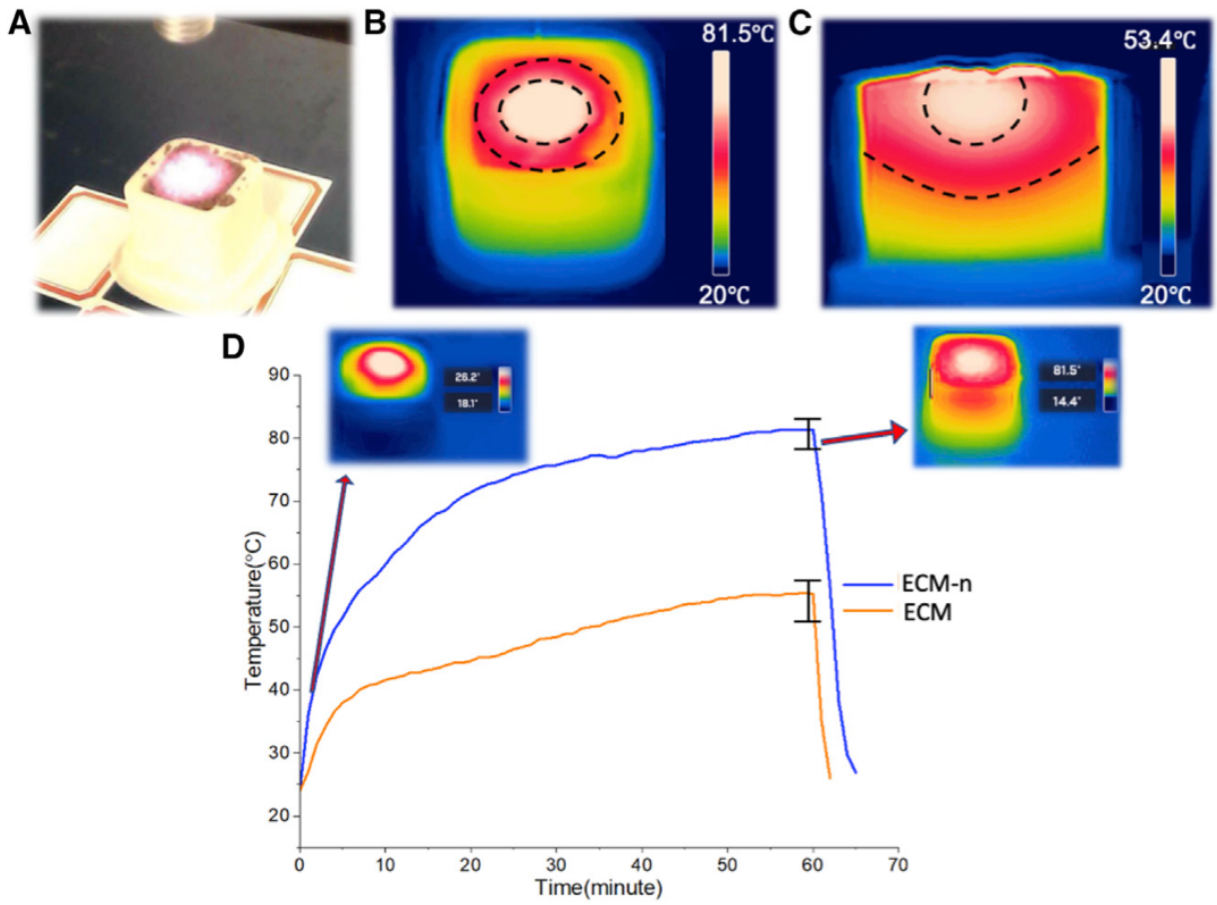

Figure 5-3 The laser induces ECM-n curing. (A) The picture of the experimental setup. (B) Top view of the temperature variation of ECM-n. The maximum temperature rises to 81.5 C at 60 min (n = 5, med = 81.5, SD = 3). (C) The side view of the temperature contours in ECM-n. (D) The temperature as a function of curing time at the center of a 0.1% nanoparticle-modified ECM-n 12.5 mm cubic sample surface under 3W laser induction compared with ECM without nanoparticles. The data of ECM and ECM-n were taken from a median group of 5 independent samples (n = 5).

5.4.2 Heat release analysis

To quantify the early curing kinetics of ECM-n, we used isothermal calorimetry (ITC) to understand the relationship between time and heat flow of ECM-n. In Figure 5-4, we compare heat flow in ECM-n samples at 25℃ and 60℃. One heat flow peak was detected at two different temperatures in 30 min and both peaks appeared immediately after injecting the enzyme calcite solution; the peak at 60℃ is more distinct than the peak at 25℃. The intensity of the peak increased with the temperature, indicating that the elevated temperature significantly enhances the degree of dissolution. The higher dissolution of the raw materials at higher temperatures provides more scaffoldings for the following bridging steps, and thus accelerated the early strength development and the final setting of the ECM-n samples.

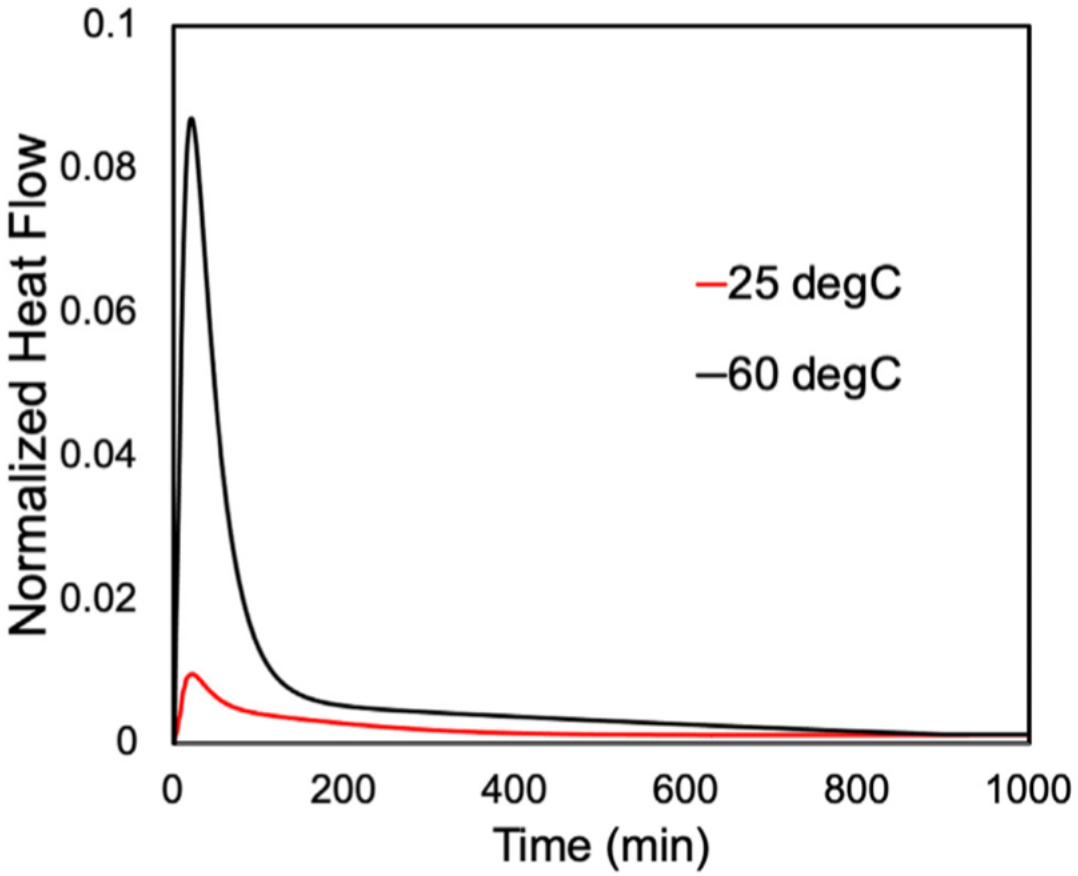

Figure 5-4 The normalized heat flow for the initial curing of ECM-n at 25 ℃ and 60 ℃ The behavior of the ECM-n heat flow after injecting an enzyme-calcite solution under 2 different temperatures. Both peaks can be identified within 6 min and then tend to plateau.

5.4.3 Mass loss and temperature over curing time between ECM-n and ECM

Both specimens were cured under a 3W laser (808 nm wavelength) for 12 h to obtain a specific degree of dehydration through mass loss evaluation (Figure 5-5 A). As shown in Figure 5-5B, the maximum surface temperature of ECM-n reaches 110℃ in 12 h to obtain full dehydration, which shows a stable mass after 9 h. In contrast, the maximum surface temperature of ECM increases to only 62℃ and maintains the mass loss condition.

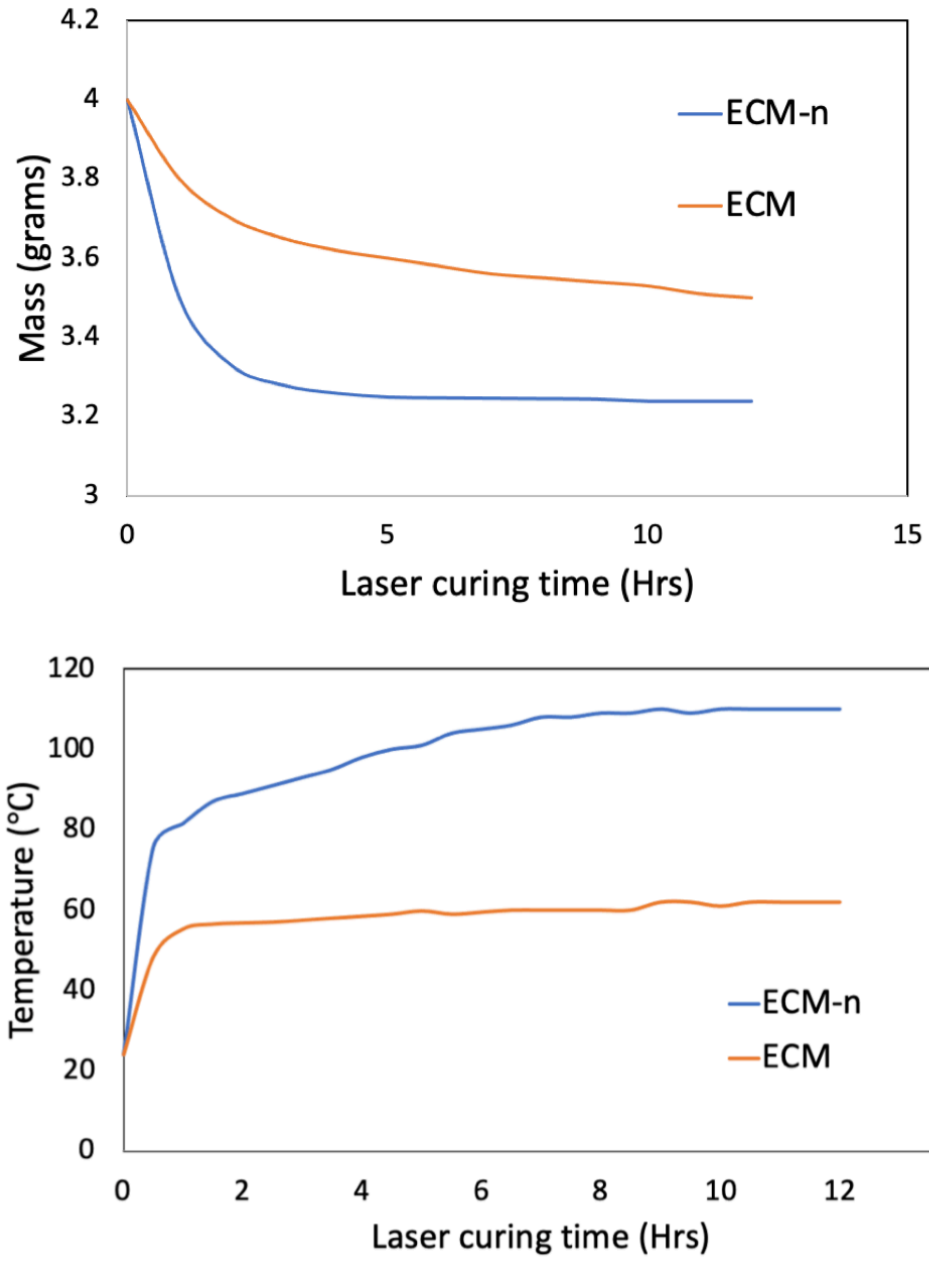

Figure 5-5 The comparison of mass loss and temperature over curing time between ECM-n and ECM a) Variation of the sample's mass over time for ECM-n cured by 3W laser at room condition versus ECM. The data of ECM and ECM-n was taken from a median group of five independent samples (n = 5). b) The temperature as a function of fully cured time at the center of

12.5 mm ECM-n sample surface under 3W laser induction compared with EICM without nanoparticles. The data were presented by median with a sample size of 3.

5.4.4 Thermogenesis of ECM-n in varies temperatures

The application of laser heating was also explored on cured ECM-n. Figures 5-6A–5-6C demonstrate the photothermal effect on cured ECM-n at ambient temperature induced by a 3W continuous wave laser. Figure 5-6A shows the experimental setup. Figures 5-6B and 5-6C show the top and side views of the contours of temperature for an ECM-n sample subjected to laser heating for about 1 h, respectively. For a sample distance of 2 cm from the laser, the peak temperature is concentrated in the center of the sample surface and spreads radially outward into the surrounding surface region. The results indicated that the maximum temperature of the ECM-n surface increases to 102℃ at room temperature. The influence of heat convection on the side can be observed in Figure 5-6C. The temperature profile shows a curve in the form of layers, with the lowest temperature at the furthest position from the heat source.

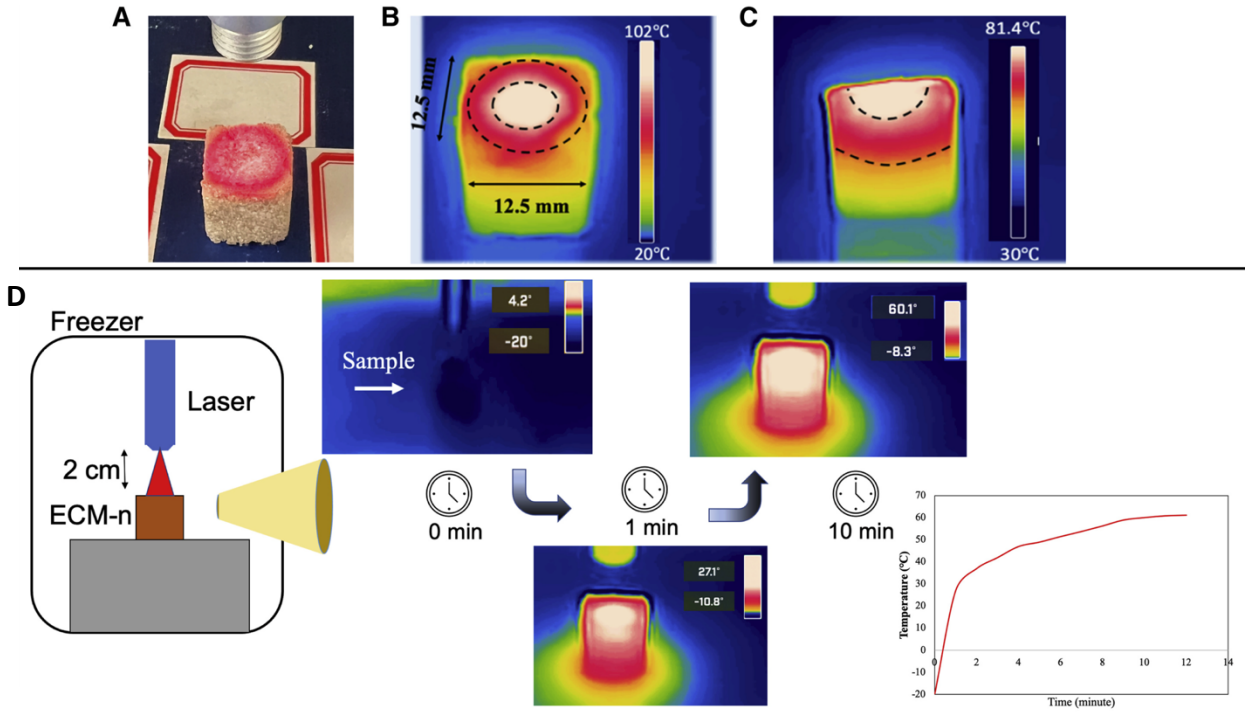

Figure 5-6 The infrared thermal images of cured ECM-n thermal effect at different temperatures (A) The laser heating experiment was set up at ambient temperature for ECM-n. (B) The spatial view of the ECM-n at 1-h laser irradiation. (C) The side view of the sample at 1 h of laser irradiation. (D) The process of laser heating of ECM-n at −20℃ freezer and the top surface temperature of the sample was raised to 60℃ in 10 min.

The photothermal effect of cured ECM-n was also explored at low temperatures. The time sequence of the experiment is presented in Figure 5-6D. The sample was stored in a −20℃ freezer to obtain a homogeneous temperature on the surface. The schematic on the left shows the experimental setup. The sample was then illuminated in a freezer by the 3W laser. A thermal camera was exploited to record the temperature of the sample surface under illumination for 10 min. At the center of the top face of the sample, the temperature increased from −20℃ to a

maximum of 60℃ in 10 min. The above findings provide a new path for ECM to be used as a thermally controllable construction material.

5.4.5 Simulation results of ECM-n

In the process of heating the ECM-n by laser, heat transfer will happen through three main mechanisms: conduction, convection, and radiation. The static laser beam follows Fourier heat conduction law [141]. The heat distribution within the ECM-n is then determined by the following transient heat transfer equation:

$$\rho C_p \frac{\partial T}{\partial t} = \nabla \cdot (k\nabla \mathrm{T}) + \alpha Q \quad (5\text{-}1)$$

where ρ is the density equal to 1,660 kg/m³, C_p is the heat capacity of sand equal to 840 J/kg · k, T is the temperature, t is the time, and the thermal conductivity of iron oxide is denoted as k, which is equal to 2.7 W/m · k [142] A thermal conductivity parameter was used to represent the iron oxide in this ECM-n model. This is done for two reasons: (1) During the dehydration process, the gelatin undergoes a phase change from a gel to a crystalline state, which complicates the modeling process, and (2) the iron oxide possesses a higher thermal conductivity than sand and gelatin, which significantly affect the temperature of the system. The absorption coefficient, α, depends on the object material and the interaction between the object material and the wavelength (808) of the laser, where most models use a constant absorption coefficient by neglecting the influence of incident angle and temperature [142]. To simplify, the absorption coefficient was assumed to be 1 in this study, and Q (W/m^3) is the laser heat source term. The boundary conditions for Equation 5-1 at the side of ECM-n are heat transfer by convection, and

at the top surface is radiation. The convection (Newton's law of cooling) in the laser heating process is expressed by

$$q_{con} = h\,(T_{ext} - T) = -\hat{n} \cdot -(k\nabla T) \tag{5-2}$$

The radiant heat flow rate of the object can be computed based on the empirical formula of Boltzmann's law by

$$q_{rad} = \varepsilon\sigma(T_{amb}^4 - T^4) \tag{5-3}$$

Heat convection always is transferred by gas or liquid media. In this study, the air is the major media in the convection. For simplicity, the heat convection coefficient is considered to be uniformly distributed and equal for all surfaces of the boundary, where h, the natural air heat convection coefficient, is 25 W/$m^2 \cdot k$ [144]. ε, the emissivity of sand is estimated to be 0.95 [141]. σ is the Stefan-Boltzmann constant, and $\hat{n}$ is the direction vector. T_{ext} and T_{amb} are the medium air and room temperatures, respectively, where both are assumed to be 300 K.

For a continuous wave laser mode, the fundamental mode of the Gaussian beam is generally preferred [146, 147], and the Gaussian heat source is provided accordingly. The rate of heat generation by the Gaussian profile of a transverse model optical intensity of order n can be given by

$$Q(x,y) = \rho f * f(x,y) \tag{5-4}$$

Here, the laser power intensity (W/m^2) can be expressed by

$$pf = \frac{P}{\pi * r^2} \tag{5-5}$$

and the Gaussian laser term is

$$f(x,y) = \exp\left[-2\left(\frac{x^2+y^2}{r^2}\right)^n\right] \tag{5-6}$$

where the laser beam was defocused to a processing radius of 6 mm. The Gaussian laser intensity profile of order 1 was implemented in Figure 5-3B. The reliability of the simulation was assessed

in comparison with the experimental data, according to the heat transfer theory, and the temperature stabilized to a relatively steady state at 10 min under continuous heat energy input, which is in agreement with the experimental results at different laser power. Both temperature profiles of the experiment and simulation are raised to 51, 78, and 105°C at 1-, 2-, and 3W laser, respectively. Figure 5-7 presents the maximum temperature as a function of time for an ECM-n sample at three different laser powers. It can be observed that the simulation results are slightly less than the corresponding experimental results, and the normalized temperature profiles are proportional to the laser power.

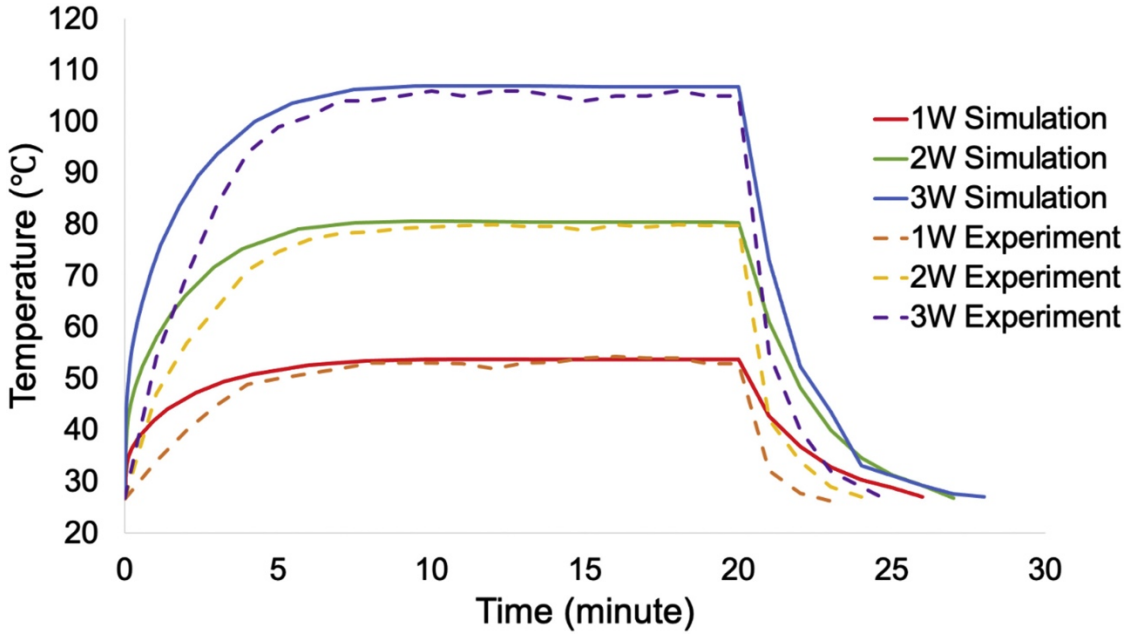

Figure 5-7 The comparison of experiment and simulation in laser heating ECM-n. Temperature changes along the time and laser power for the ECM-n in 30 min. The laser was removed for 20 min and the materials started to cool to the ambient temperature. The results from experiments and the predictions show reasonable agreement.

5.4.6 Self-healing assessment under laser curing

The self-healing ability of ECM had been extensively assessed in our previous publications.5 This potential feature was also demonstrated with a similar set of experiments with nanoparticle-modified ECM (ECM-n), which is shown in Figure 5-8. We find that the ECM-n cuboid sample autonomously self-healed with laser heating without an external force or additional treatment. When fractures occur, the scaffold bridges are exposed on the fracture faces, which implies that the mineral bridges are the weak link in the microstructure of ECM.

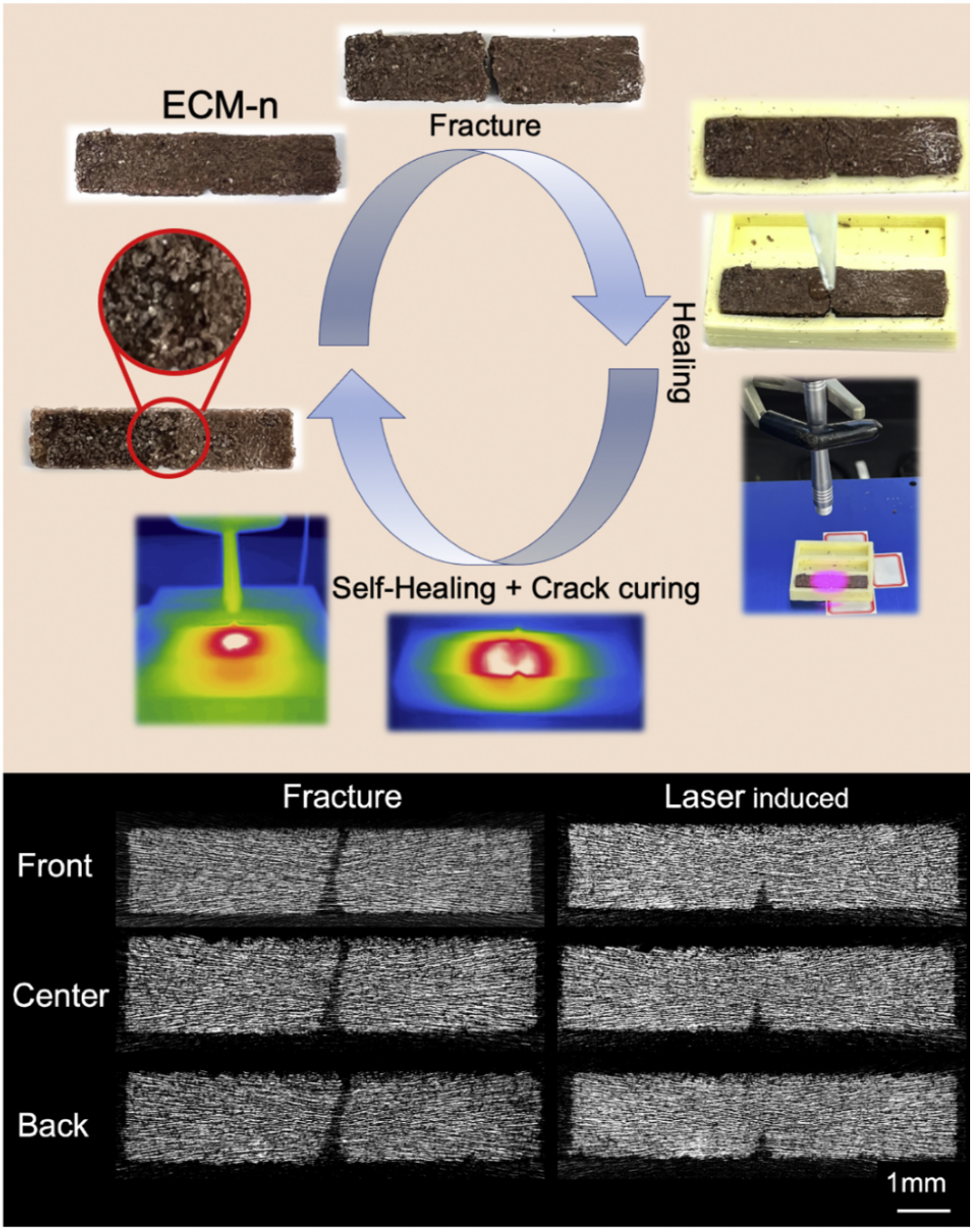

Figure 5-8 The schematic illustration of the self-healing capability of ECM-n beam via laser-induced heating. (A) A trace amount of calcium-enzyme solution was added to the fractured area. Then, ultra-pure CO_2 was aerated on the surface for 15 min. The 3W laser was conducted in the same location over 4 h. The heterogeneous shape of the high-temperature region (white color) develops into a circle gradually. (B) μ-CT scanned images of fracture and laser healing ECM-n beam at the front, center, and back layers.

The fractured sample was assembled in a silicon mold, and then the CO_2 gas was sprayed continuously on the fracture region. In the healing process, the precipitated $CaCO_3$ crystals were expected to gradually grow on the scaffold [148] and eventually bridge the fracture interface during laser heating. It was noted that the additional carbonic anhydrase was added with the calcium solution in the crack area; this is due to the decreasing enzyme activity during laser photo illumination. The fracture cuboid ECM-n sample was treated with calcium solution with a trace amount of enzyme (5 μL, 2.9 mg/mL) compared with the sample without enzyme treatment in the calcium source agent, which presented more crystals on the repaired crack after laser curing (Figure 5-9). The macroscale characterizations of the self-healing process can also be observed from the temperature profile of the sample. The temperature profile contour changes during the healing process, as expected because the nanoparticles are carried by a fluid medium and diffused until the sample is desiccated. The 4.1 × 3.5 mm fracture surfaces were fully repaired after 4 h of laser treatment. The resulting ECM-n has the same self-healing capability as ECM and provides a potential application for outstanding material durability. We also used microcomputed tomography (μ-CT) scanning to characterize and diagnose the internal and external microstructures of cracks within the ECM-n matrix (Figure 5-9B). The μ-CT scanning images clearly show the crack path disappearing in three display layers (front, center, and back), indicating that the internal crack has self-healed as predicted by laser photo illumination.

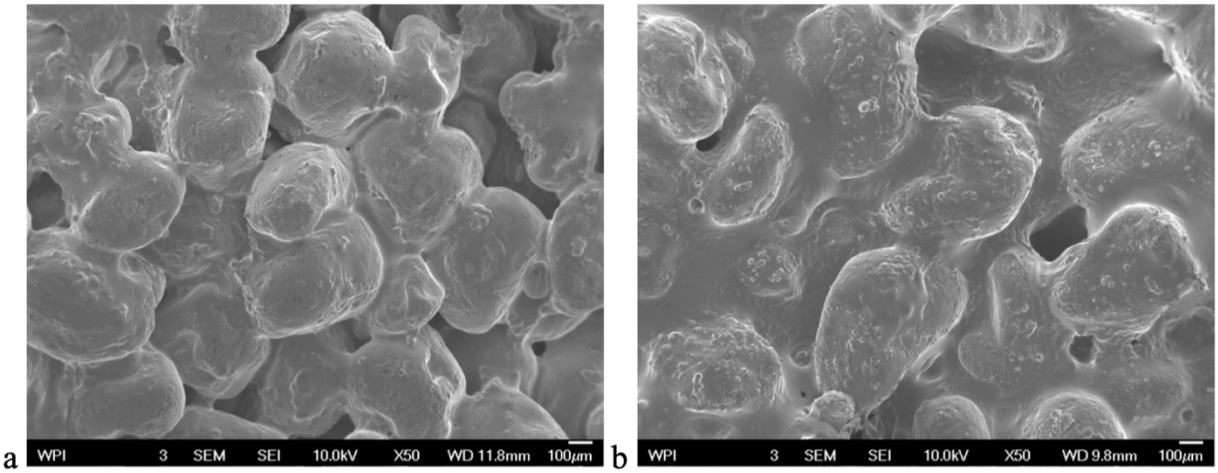

Figure 5-9 The comparison of the self-healed ECM-n samples under the presence of carbonic anhydrase a) Fracture sample was healed by calcium solution and CO_2 without enzyme. b) Fracture sample was healed by calcium solution and CO_2 with the enzyme.

5.4.7 ECM-n morphology and crystallinity characterizations

The optical and scanning electron microscopy (SEM) images of the morphology of ECM and ECM-n in multiscale were presented in Figure 5-10A–5-10I, showing a variation in calcite crystals size at ~10 μm. Detailed morphological characterization indicates that the laser-treated surfaces and the structure of ECM-n are similar to ECM without nanoparticles and cured in an oven. Calcite crystal distribution and the dimension of the hydrogel scaffold were not affected by the laser curing. The ordered structures were well assembled in ECM-n and ECM to efficiently shield the crack propagation. Although the sand particles and calcite crystals were assembled randomly within the polymeric scaffold, the overall view is similar to a body-centered cubic (BCC) crystal. In the plane view, the sand particles in both samples are connected with bridges in at least four directions. Due to the characterization of BCC structural type, sand slurry materials show a high ductility during the bending test, and with a high strain at 0.0032 compared with a

normal weight concrete in the range from 0.002 to 0.003. As a result, the local application of the photothermal effect by iron oxide nanoparticles exhibits a mild effect in ECM-n, showing the high extent of stability and mechanical strength in sand slurry materials structure.

The nanoparticle distribution in ECM-n was also investigated by energy dispersion spectroscopy (EDS), optical microscopy, and Raman spectroscopy, as shown in Figure 5-10B, 5-10H, and 5-12, respectively. The EDS and optical images clearly show the nanoparticles distributed on each of the sand particles, correlating to a spherical temperature profile. The slight aggregation of nanoparticles occurring on the surface is due to the lack of surfactants during nanoparticle preparation. The surfactant coating consists of a variety of ester-based materials that depend on environmental factors at varying levels of chemical complexity; thus, only physical treatment was applied to the nanoparticles by the ultrasonic method to avoid a negative impact on the medium.

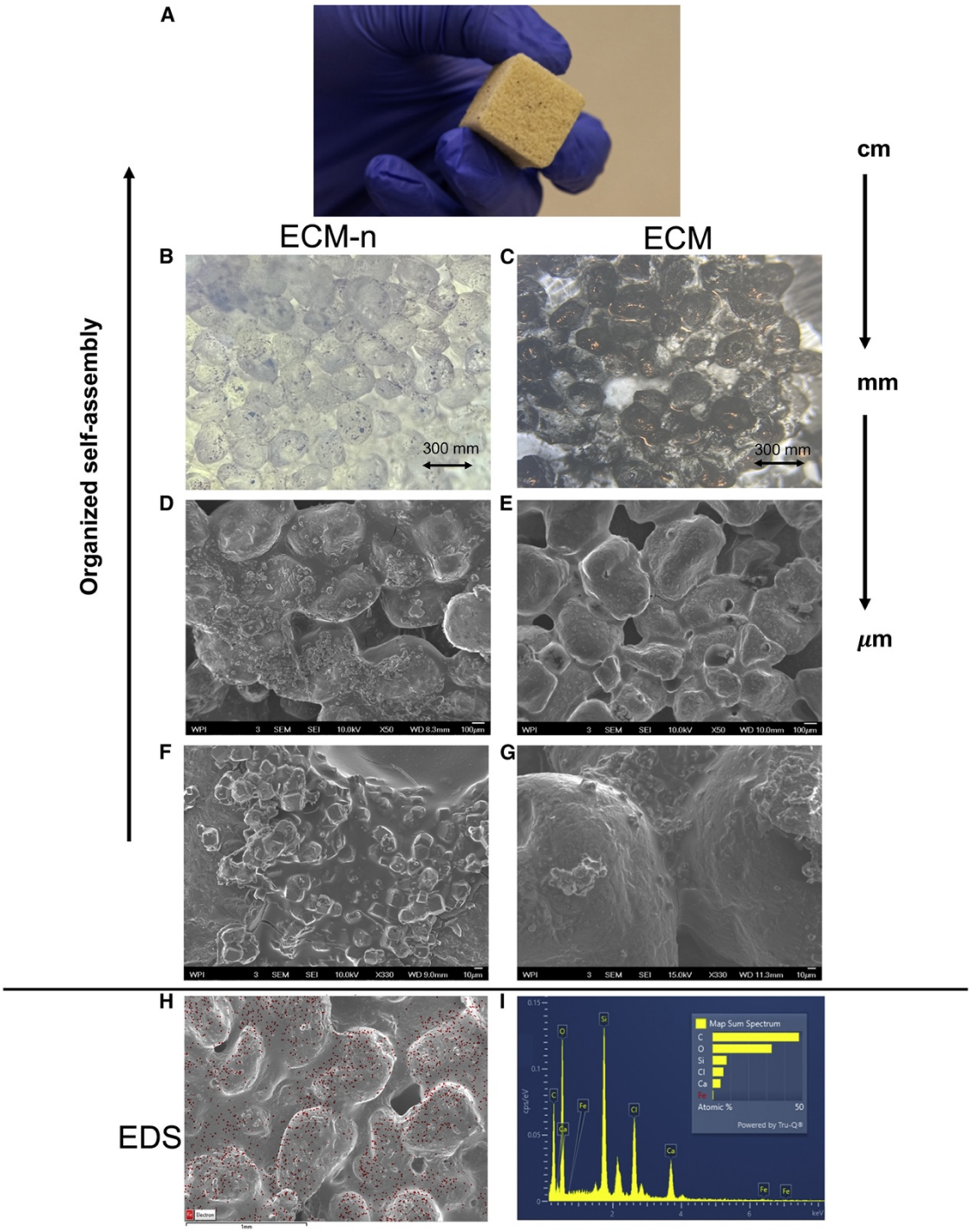

Figure 5-10 Comparing the multiscale microstructure and mineralization of ECM-n (left) and ECM (right). (A) The real size of ECM-n in the hand. (B–E) SEM and optical images of laser-cured ECM-n and oven-cured ECM showing that the scaffold bridges and calcite crystals are distributed uniformly. (F and G) Higher magnification SEM images of scaffold bridges formed

by laser curing (F) and oven curing (G). (H and I) (H) EDS mapping images of the nanoparticle distribution in the matrix and (I) the major chemical compositions.

We sought to understand whether the crystallinity and morphology of crystals generated by enzyme catalysis were influenced by laser illumination. Our previous study has proven that the enzyme product is calcite through Fourier transform infrared spectroscopy (FTIR) and powder X-ray diffraction (pXRD). The typical pXRD patterns in Figure 5-11 show the presence of precipitated calcium carbonate on ECM-n after laser curing, where a diffraction peak is observed at $2\theta = 29.6°$, which agrees with the reference spectrum for calcite. The result verifies the crystallinity of the enzyme product as calcite. The morphology is supported by the SEM images in Figure 5-10.

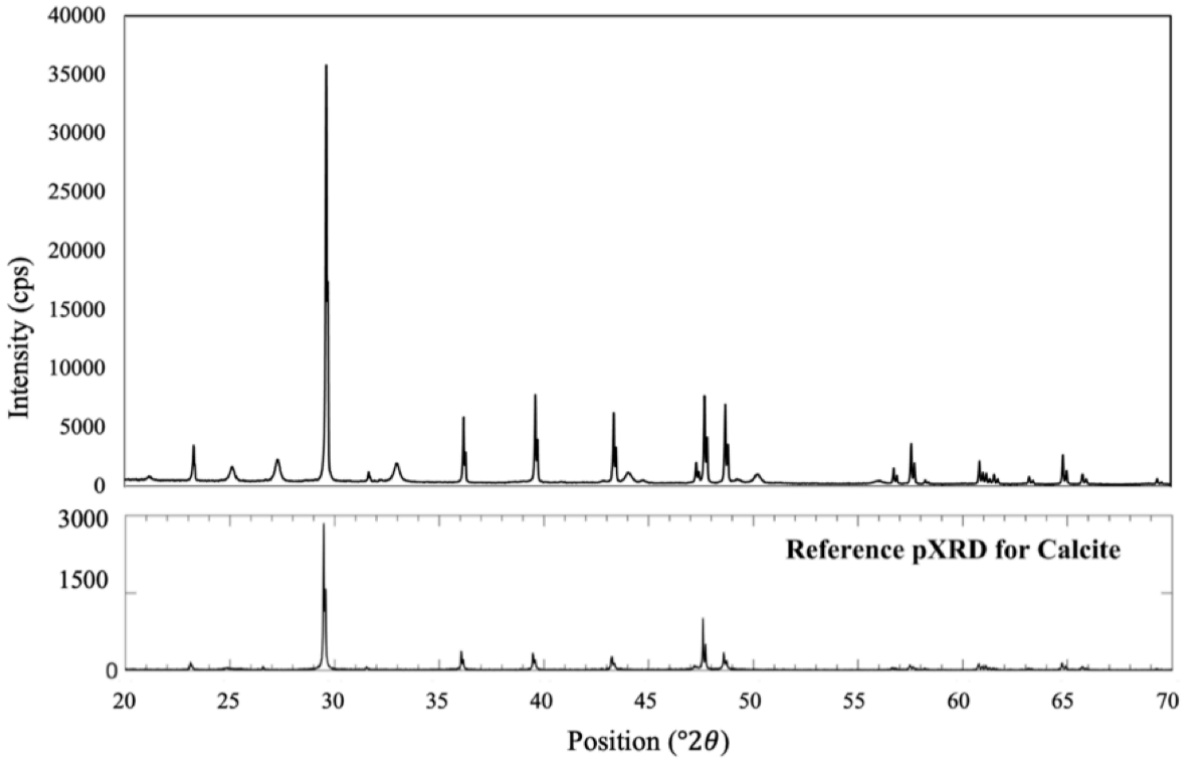

Figure 5-11 Powder X-ray diffraction (pXRD) analysis of the enzyme-generated calcium carbonate in presence of laser induction, with comparison to the reference spectrum for calcite This comparison confirms the crystallinity of the product after laser curing resulting from the enzyme repair method.

5.4.8 Raman spectroscopy results

To further identify the distribution of nanoparticles as well as the precipitated crystals, four different locations on the sample surface were spotted by Raman spectroscopy. Raman spectroscopy is a nondestructive analytical technique based on changes in the scattering of low-energy light off material and can be used directly on the whole sample. Figure 5-12 displays the locations on the ECM-n surface that correspond to calcite and gamma Fe_2O_3. The spectra were processed and plotted proportionally by fitting the Gaussian function. The Raman characteristic peak of calcium carbonate is relatively narrow, indicating a high extent of crystallization, and the intensity of the peak is higher, indicating a higher content of calcite crystals and iron oxide nanoparticles in this region of the sample surface. The above results show that the nanoparticle distribution in the ECM-n achieves the desired effect.

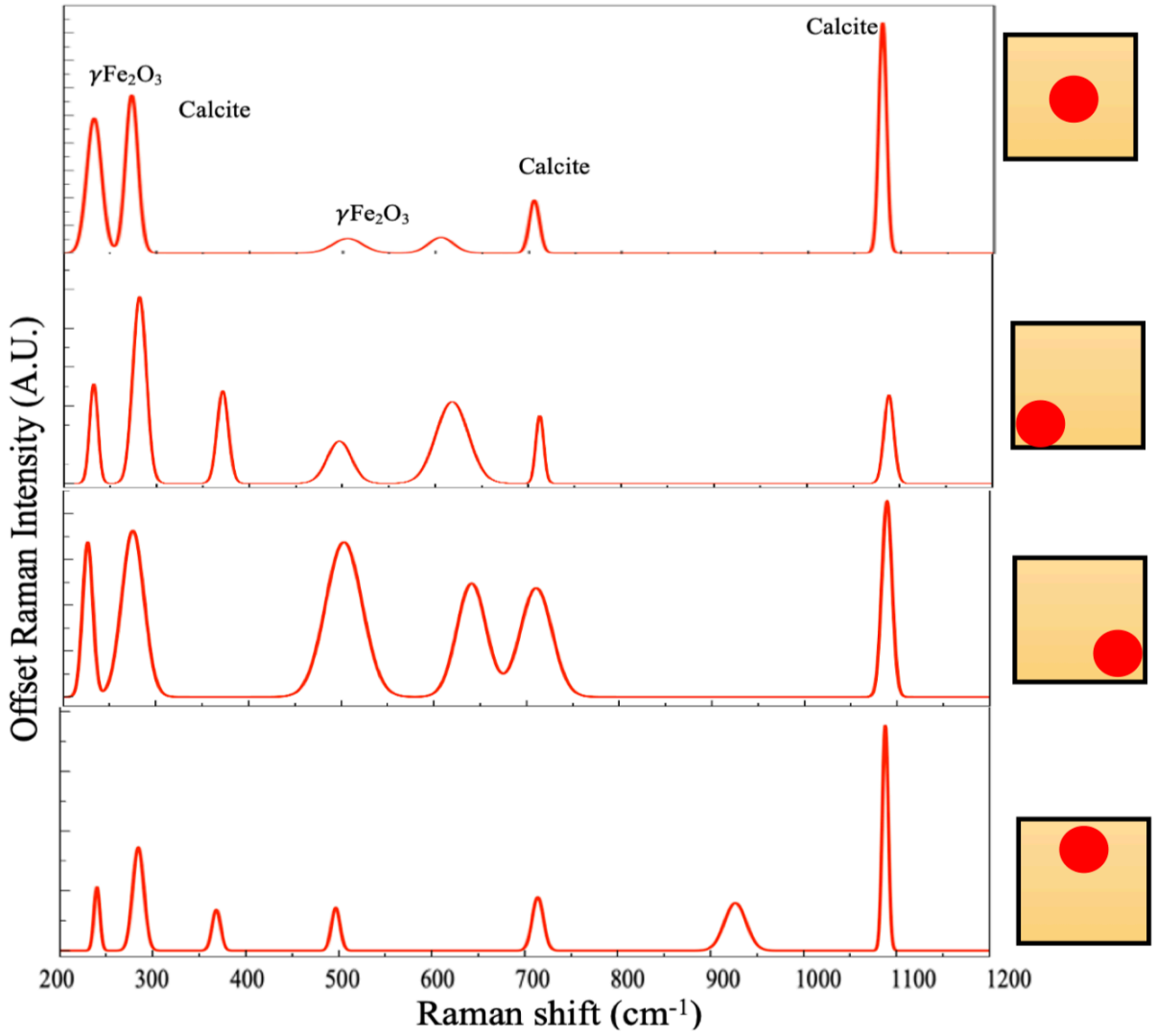

Figure 5-12 The normalized Raman spectra of four different spots on the cured ECM-n surface. The peak analysis was processed and plotted by fitting the Gaussian function. The calcite and γFe_2O_3 positions were annotated in the diagram.

5.4.9 Mechanical properties of repaired ECM-n

Designing high-performance construction building materials with excellent compressive strength is a long-standing engineering problem. Our previous studies had investigated the self-healing ability and tensile strength of ECM by oven desiccation, while the compressive strength

after repairing still needs to be verified. Here, we investigate the repair of large-scale notches while applying laser. To study the repair performance of the proposed mechanism on laser-induced curing of ECM and ECM-n, cubic-shaped specimens were fabricated for compressive testing, with two types of circular and elliptical flaws. The control and flawed samples are shown in Figure 5-13. It is noted that the ECM-n samples were cured by laser and the flawless ECM samples were cured in the oven. The laser-induced repairing experiment is shown in Figure 5-13A. The normalized values of compressive strengths compared to the control are presented in Figure 5-13B. The ECM-n samples, with a vertically oriented elliptical flaw that is 6 mm tall and 1.5 mm wide and extends through the cubic sample through the entire 12.5-mm depth, represent a macroscale crack that exhibits 74% of the strength of the undamaged control specimens. The samples with a circular flaw of 2 mm diameter and extending through the entire depth of the cube sample of 12.5 mm show 70% of the strength of the undamaged control specimens.

The compressive strength results show that cube-shaped samples with built-in flaws can regain their original compressive strength by adding the calcium enzyme mixed solution to the original sand gelatin matrix. The material was then bubbled with ultra-pure carbon dioxide for 10 min. This is followed by the application of the laser for curing for 12 h. The samples with the largest size of the repaired flaws (6 mm in vertical direction) still exhibit the capability of the proposed method in the repair of the ECM-n specimens. It must be noted that both repaired flaw shape samples slightly outperform the control samples with respect to the average compressive strength. The compatibility of the existing matrix with the additional sand-gelatin repair agent is excellent, and the repair process also allows additional curing of the original matrix, leading to an overall stiffer structure.

Comparing the results, the variation in the strength of the elliptical flaw and repaired elliptical flaw ECM-n samples is relatively high. This difference is mainly due to the geometric offset of the elliptical flaw during the sample preparation in the silicone mold. It is noted that the samples with prefabricated elliptical and circular flaw fail by crack initiation at the flaw and growth resulting from dilatation due to Poisson's effect. The p value of flawed ECM-n samples is <0.05, which leads to significant changes in the performance of the structure, while the p value of repaired elliptical and circular flaw ECM-n is within statistical error (>0.05). Therefore, ECM-n with flaws maintains mechanical stability after repair by the laser.

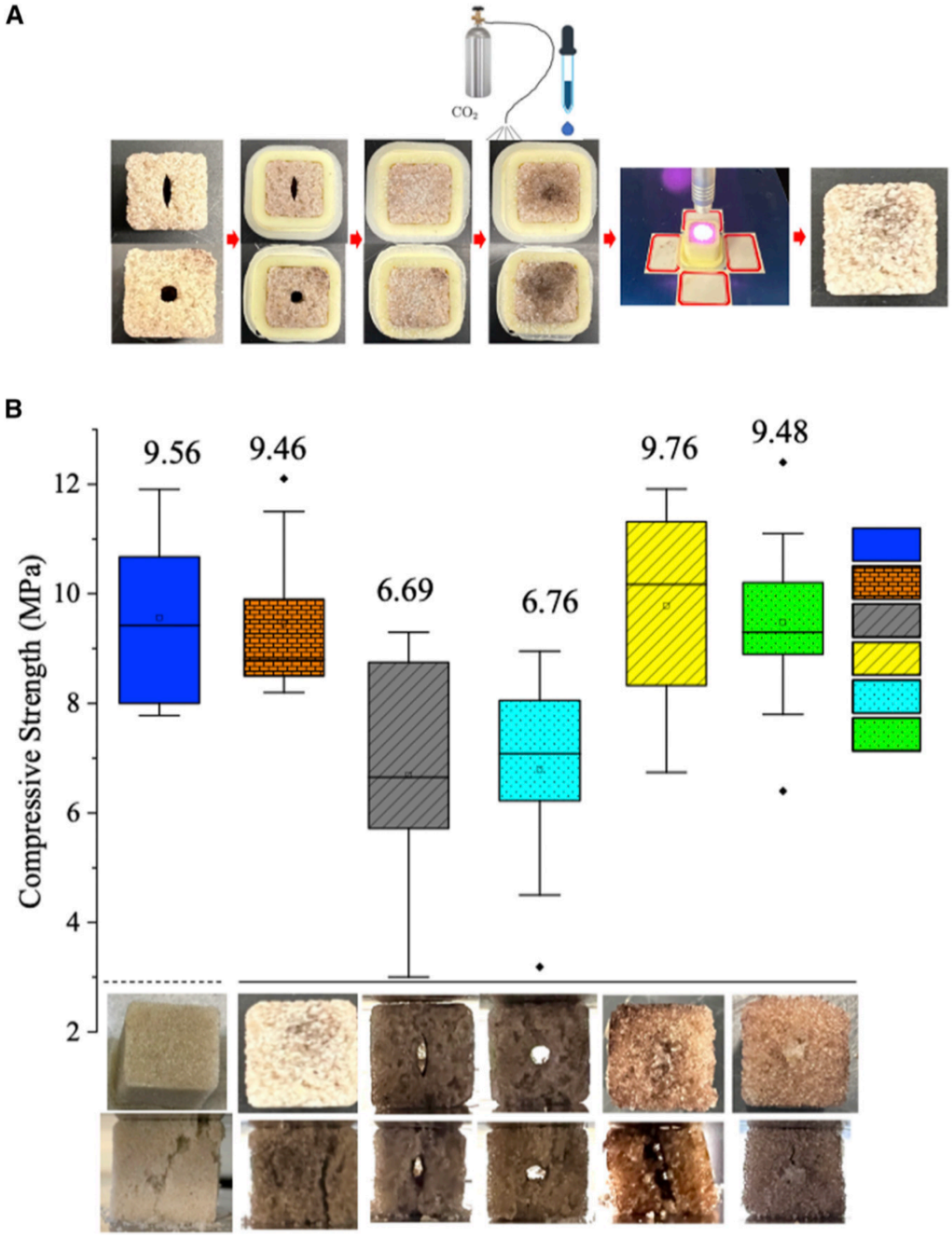

Figure 5-13 The compressive strength of laser-repaired ECM-n with different flaws ECM-n samples with different flaw shapes were repaired and compared with oven-cured ECM. (A and B) (A) The laser repairing paradigm of ECM-n: the mean results are shown above each dataset, and a typical sample is shown at the bottom in (B). The compressive strength of ECM, in order

from left to right are oven-cured ECM (n = 12, blue, med = 9.56, SD = 1.49), laser-cured ECM-n (n = 10, brown, med = 9.45, SD = 1.44), elliptical flaw ECM-n (n = 10, gray, med = 6.69, SD = 1.92, p = 0.003), circular flaw ECM-n (n = 10, yellow, med = 6.76, SD = 1.79, p = 0.004), repaired elliptical flaw ECM-n (n = 10, light blue, med = 9.76, SD = 1.86, p = 0.43), and repaired circular flaw ECM-n (n = 10, green, med = 9.47, SD = 1.75, p = 0.48).

5.4.10 Embodied energy and CO_2 of ECM/ECM-n

To visualize the impact of ECM/ECM-n on sustainable environmental protection and various types of construction materials, we compare the embodied energy versus the embodied CO_2 and specific strength versus the embodied CO_2 associated with different construction materials (Figures 5-14A, and 5-14B). Except for ECM/ECM-n, embodied energy, embodied CO_2, and specific strength data were selected from the inventory published by Hammond and Jones and Ashby [149, 150]. The Ashby diagram of embodied energy versus embodied strength shows that ECM/ECM-n consumes CO_2 as seen by negative values compared to other construction materials. This is because the formation of the ECM/ECM-n requires the consumption of carbon dioxide. Furthermore, the ECM/ECM-n presents relatively low energy consumption.

The boundaries that were considered in this study are cradle to gate. Thus, the transportation consuming energy and manufacturing processes of ECM/ECM-n were recognized similarly to concrete in this report. The negative CO_2 emissions and low-energy embodiment of ECM/ECM-n are because most of the components can be obtained directly in nature or by simple secondary processing. The enzyme, carbonic anhydrase, which is added in trace amounts, is isolated from bovine erythrocytes or other natural sources [151], which does not generate

carbon dioxide, and requires little energy. The calcium can be obtained from natural brines as a by-product of synthetic soda ash production [152]. Another low-carbon method is to produce calcium from hydrochloric acid and limestone. The process will generate hydrogen that can be directly burned or generated by fuel cells to obtain water, which can be achieved by true zero carbon emissions without polluting the environment. The gelatin is extracted by hydrolysis of biological material in a process that is essentially zero emissions [153]. In our paradigm, only 0.1% (by sand weight) nanoparticles were applied in the medium, and many researchers have proven that the nanoparticles are a clean product that can capture and use CO_2 from the air [154, 155, 156] The specific mechanical properties of ECM/ECM-n were also compared with other construction materials in Figure 5-14B. Cracking is assumed to be the initiation of concrete failure. The specific strength of ECM/ECM-n was comparable to the lightweight concrete (LWC) and the minimum of the commercial concrete. There is no negative impact of nanoparticles between ECM and ECM-n, which result in the same mechanical properties as discussed in the section 5.4.9.

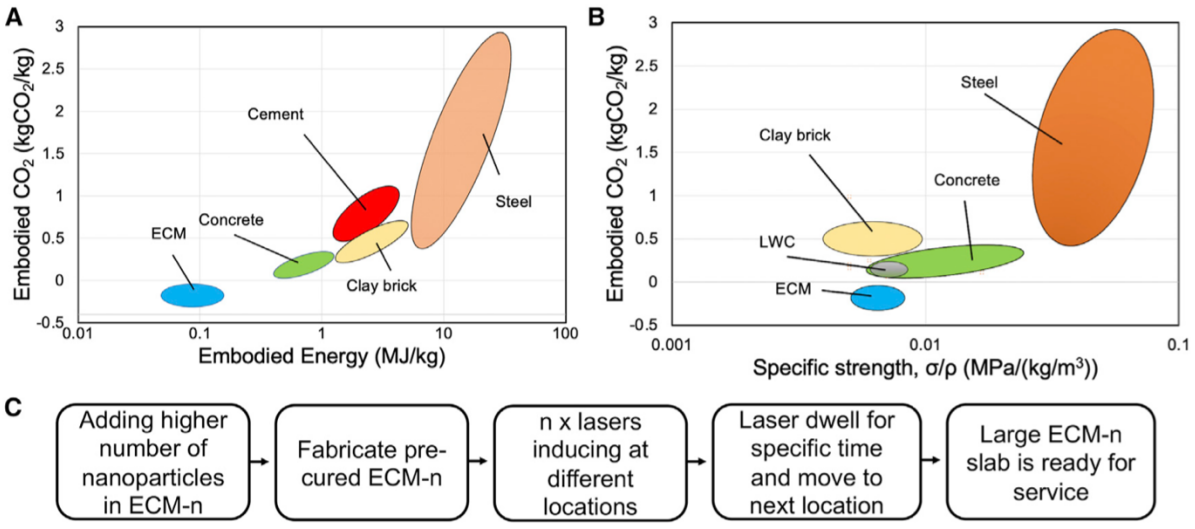

Figure 5-14 Ashby diagram and scaling up ECM-n procedures Carbon footprint and mechanical properties of ECM/ECM-n compared to different construction materials. (A) Ashby diagram of embodied CO_2 versus embodied energy data for reference materials was extracted from the inventory published by Hammond and Jones [149]. (B) Ashby diagram of specific strength versus embodied CO_2 for comparison with related construction materials. (C) The basic procedures of fabricating ECM-n on construction site.

5.4.11 Alternative light source

Adding a trace amount of iron oxide nanoparticles to ECM generates an improved material called ECM-n that is easily cured with a low-power laser, or incandescent light (the curing incandescent light experiment set up can be found at support information, Figure 5-15).

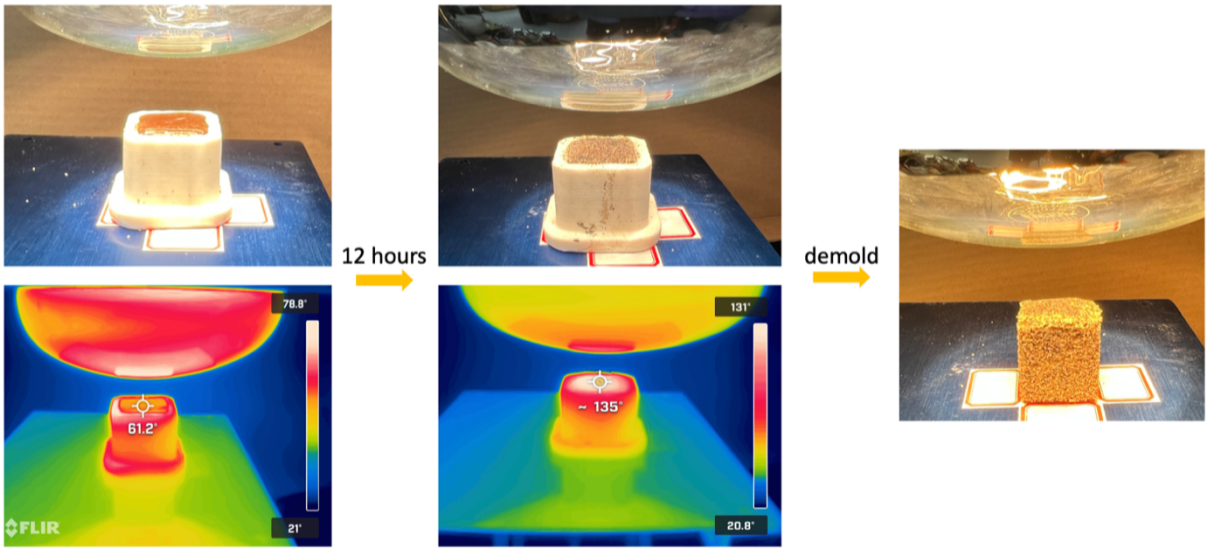

Figure 5-15 The experiment of incandescent light curing ECM-n sample. The ECM-n sample was cured in 12 hours at the ambient condition.

5.4.12 Other trials on the curing acceleration

To investigate an alternative method expediting ECM curing, we proposed adding highly electron conductive constituent (carbon black) in the ECM. Sample clamped between two conductive graphite foils connected to a DC voltage generator (Agilent DC power supply), see Figure 5-16. However, the electrolysis of gelatin and water under high voltage (10V) can be observed. Ammonia can be smelled because the amino groups in the gelatin are electrolyzed into ammonia and released. The ECM can not form in solid without water and gelatin.

Figure 5-16 The experiment set up of carbon black modified ECM.

5.5 Summary and Conclusion

In this study, we established a curing protocol with the use of a trace amount (0.1% by mass) of nanoparticles and a low-power laser that we applied to the recently created ECM. The presence of nanoparticles and laser-induced curing preserved the integrity of ECM, including compressive strength and self-healing capability. A multiphysics model is provided for the future optimization of new functionalities of ECM-n production as emerging green technology applications, ranging from radiant heating to carbon sequestration techniques. Given the global

environmental impact of the production of cement-based materials, the development and implementation of such novel functionalities are expected to foster the sustainable development of both the construction sector and our built infrastructure at large. This method may provide a step toward thermally controllable self-healing construction material.

5.6 Future work

5.6.1 Scaling up method

Scaling up the concept of ECM-n from the lab to the construction site can be achieved in a few years. These materials can entirely replace LWC and masonry blocks in all of their applications. In particular, the ECM-n can rapidly be constructed for the temporary base, secondary structure, and pipe in extreme weather. Here, a guiding flowchart is provided as a reference (Figure 5-14B). From the above results, the effective area of ECM-n is proportional to the number of nanoparticles and the power of the laser. Therefore, in on-site construction, a higher number of nanoparticles and higher-power laser are suggested to apply on the ECM-n to guarantee the desired effects. For example, to fabricate a 10 × 10 ft ECM-n slab, pre-cured ECM-n can be prepared on the foundation, and then 10 industrial laser machines can be induced at different spots (we assume the effective area is 0.5 × 0.5 ft). A trial experiment can be carried out in the field to develop a relationship between required depth and laser-inducing time. Designing the laser dwell at each spot for a specific time to achieve full curing (3W laser induces 4 h for a 12.5-mm depth) before moving to the next spot. The total time should be ~160 h without considering the ambient humidity and natural drying rate, but this will decrease exponentially with an increase in the number of nanoparticles added. However, achieving the

balance between time effectiveness and power cost is the key to this process. Upon ECM-n slab completion, the potential for heat transfer applications (especially in winter) is unlimited.

References

[1] Camarasa, C., Mata, É., Navarro, J.P.J. (2022). A global comparison of building decarbonization scenarios by 2050 towards 1.5–2 °C targets. Nat Commun 13, 3077.

[2] Energy efficiency for buildings, The Renewable Energy Institute.

[3] Editorials. (2021). Concrete needs to lose its colossal carbon footprint. 597, 593-594.

[4] Concrete CO2 Fact Sheet. (2012). National Ready Mixed Concrete Association. Silver Spring. MD. 2012.

[5] Kamennaya, N.A., Ajo-Franklin, C.M., Northen, T., Jansson, C. (2012). Cyanobacteria as Biocatalysts for Carbonate Mineralization. *Minerals*. *2*, 338-364.

[6] Booth, P., Jankovic, L. (2022). Front. Built Environ. Novel biodesign enhancements to at-risk traditional building materials, 03.

[7] Devi, V.K.A., Shyam, R., Palaniappan, A., Jaiswal, AK., Oh, TH., Nathanael, AJ. (2021). Self-Healing Hydrogels: Preparation, Mechanism and Advancement in Biomedical Applications. Polymers (Basel). 13, 21,3782.

[8] David, W., Green, Besim, Ben-Nissan., Kyung, Sik, Yoon., Bruce, Milthorpe., Han-Sung, Jung., (2017). Natural and Synthetic Coral Biomineralization for Human Bone Revitalization, Trends in Biotechnology. 35, 1,43-54.

[9] Rabia, O., M, Mohsin., A, Mohsin., B, Sajid., X, Huang., M, Guo., Y, Zhuang., J, Huang. (2022). Engineered Bacteria-Based Living Materials for Biotherapeutic Applications. Front. Bioeng. Biotechnol.

[10] Global warming of 1.5°C, Intergovernmental Panel on Climate Change (IPCC) Sixth Assessment report. (2021). Intergovernmental Panel on Climate Change.

[11] Provisional State of the Global Climate in 2022. (2022). World Meteorological Organization.

[12] Overview of greenhouse gases, United States Environmental Protection Agency.

[13] Bossio, D.A., Cook-Patton, S.C., Ellis, P.W. (2020). The role of soil carbon in natural climate solutions. Nat Sustain. 3, 391–398

[14] Sameer, H., Weber, V., Mostert, C., Bringezu, S., Fehling, E., Wetzel, A. (2019). Environmental Assessment of Ultra-High-Performance Concrete Using Carbon. Material, and Water Footprint. Materials. 12, 851.

[15] Scott, A., Oze, C., Shah, V. (2021). Transformation of abundant magnesium silicate minerals for enhanced CO2 sequestration. Commun Earth Environ 2, 25.

[16] Borowski, Piotr F., I, Patuk., E.R. Bandala. (2022). Innovative Industrial Use of Bamboo as Key “Green” Material" Sustainability. 14, 1955.

[17] Abomohra, A.E., Jin, W., Tu, R., Han, S., Eid, M., Eladel, Hamed. (2016). Microalgal biomass production as a sustainable feedstock for biodiesel: Current status and perspectives, Renewable and Sustainable Energy Reviews. 64, 596-606.

[18] Gupta, S., Kua, H.W., Low, C.Y. (2018). Use of biochar as carbon sequestering additive in cement mortar, Cement and Concrete Composites. 87, 110-129.

[19] Arehart, J.H., Hart, J., Pomponi, Francesco., D'Amico., B. (2021). Carbon sequestration and storage in the built environment. Sustainable Production and Consumption. 27,1047-1063.

[20] Samarin, A. (1999, May). Wastes in concrete: converting liabilities into assets. In Creating with Concrete: Opening and Leader Papers of the Proceedings of the

International Congress Held at the University of Dundee, Scotland, UK on 6-10 September 1999 (pp. 131-151). Thomas Telford Publishing.
[21] Le Quéré, C., Andrew, R. M., Friedlingstein, P., Sitch, S., Hauck, J., Pongratz, J., ... & Zheng, B. (2018). Global carbon budget 2018. Earth System Science Data, 10(4), 2141-2194.
[22] Chen, D., & Mahadevan, S. (2008). Chloride-induced reinforcement corrosion and concrete cracking simulation. *Cement and Concrete Composites*, *30*(3), 227-238.
[23] Lahmann, D., Edvardsen, C., Kessler, S. (2023). Autogenous self-healing of concrete: Experimental design and test methods, A review. *Engineering Reports*, *5*(1), 12565.
[24] Termkhajornkit, P., Nawa, T., Yamashiro, Y., Saito, T. (2009). Self-healing ability of fly ash–cement systems. *Cement and concrete composites*, *31*(3), 195-203.
[25] Elhakam, A., & Awad, E. (2012). Influence of self-healing, mixing method and adding silica fume on mechanical properties of recycled aggregates concrete. *Construction and Building Materials*, *35*, 421-427.
[26] Huang, H., Ye, G., & Damidot, D. (2014). Effect of blast furnace slag on self-healing of microcracks in cementitious materials. *Cement and concrete research*, *60*, 68-82.
[27] Chen, H. J., Peng, C. F., Tang, C. W., & Chen, Y. T. (2019). Self-healing concrete by biological substrate. *Materials*, *12*(24), 4099.
[28] Bang, S. S., Galinat, J. K., & Ramakrishnan, V. (2001). Calcite precipitation induced by polyurethane-immobilized Bacillus pasteurii. *Enzyme and microbial technology*, *28*(4-5), 404-409.
[29] Sarda, D., Choonia, H. S., Sarode, D. D., & Lele, S. S. (2009). Biocalcification by Bacillus pasteurii urease: a novel application. *Journal of Industrial Microbiology and Biotechnology*, *36*(8), 1111-1115.
[30] Jena, S., Basa, B., & Panda, K. C. (2021). Effect of Bacillus Cohnii bacteria on the properties of concrete. In *Recent Developments in Sustainable Infrastructure: Select Proceedings of ICRDSI 2019* (pp. 597-606). Springer Singapore.
[31] Grabiec, A. M., Klama, J., Zawal, D., & Krupa, D. (2012). Modification of recycled concrete aggregate by calcium carbonate biodeposition. *Construction and Building Materials*, *34*, 145-150.
[32] Fischer, G., & Li, V. C. (2002). Influence of matrix ductility on tension-stiffening behavior of steel reinforced engineered cementitious composites (ECC). *Structural Journal*, *99*(1), 104-111.
[33] Fischer, G., & Li, V. C. (2003). Deformation behavior of fiber-reinforced polymer reinforced engineered cementitious composite (ECC) flexural members under reversed cyclic loading conditions. *Structural Journal*, *100*(1), 25-35.
[34] Maalej, M., & Li, V. C. (1994). Flexural/tensile-strength ratio in engineered cementitious composites. *Journal of Materials in Civil Engineering*, *6*(4), 513-528.
[35] McBee, R. M., Lucht, M., Mukhitov, N., Richardson, M., Srinivasan, T., Meng, D., ... & Wang, H. H. (2022). Engineering living and regenerative fungal–bacterial biocomposite structures. *Nature Materials*, *21*(4), 471-478.
[36] An, B., Wang, Y., Huang, Y., Wang, X., Liu, Y., Xun, D., ... & Zhong, C. (2022). Engineered Living Materials For Sustainability. *Chemical Reviews*.
[37] Anbu, P., Kang, C. H., Shin, Y. J., & So, J. S. (2016). Formations of calcium carbonate minerals by bacteria and its multiple applications. *Springerplus*, *5*, 1-26.

[38] Phillips, A. J., Gerlach, R., Lauchnor, E., Mitchell, A. C., Cunningham, A. B., & Spangler, L. (2013). Engineered applications of ureolytic biomineralization: a review. *Biofouling*, *29*(6), 715-733.
[39] Heveran, C. M., Williams, S. L., Qiu, J., Artier, J., Hubler, M. H., Cook, S. M., ... & Srubar, W. V. (2020). Biomineralization and successive regeneration of engineered living building materials. *Matter*, *2*(2), 481-494.
[40] Boys, A. J., Zhou, H., Harrod, J. B., McCorry, M. C., Estroff, L. A., & Bonassar, L. J. (2019). Top-down fabrication of spatially controlled mineral-gradient scaffolds for interfacial tissue engineering. *ACS biomaterials science & engineering*, *5*(6), 2988-2997.
[41] Pondelak, A., Škapin, A. S., Knez, N., Knez, F., & Pazlar, T. (2021). Improving the flame retardancy of wood using an eco-friendly mineralisation process. *Green Chemistry*, *23*(3), 1130-1135.
[42] Alsubari, S., Zuhri, M. Y. M., Sapuan, S. M., Ishak, M. R., Ilyas, R. A., & Asyraf, M. R. M. (2021). Potential of natural fiber reinforced polymer composites in sandwich structures: A review on its mechanical properties. *Polymers*, *13*(3), 423.
[43] Espinosa, H. D., Rim, J. E., Barthelat, F., & Buehler, M. J. (2009). Merger of structure and material in nacre and bone–Perspectives on de novo biomimetic materials. *Progress in Materials Science*, *54*(8), 1059-1100.
[44] Rao, A., Divoux, T., Owens, C. E., & Hart, A. J. (2022). Printable, castable, nanocrystalline cellulose-epoxy composites exhibiting hierarchical nacre-like toughening. *Cellulose*, *29*(4), 2387-2398.
[45] Guvendiren, M., Molde, J., Soares, R. M., & Kohn, J. (2016). Designing biomaterials for 3D printing. ACS biomaterials science & engineering, 2(10), 1679-1693.
[46] Guo, Z., Han, J., Xu, Y., Lu, Y., Shi, C., Ge, L., ... & Li, J. (2019). The mineralization characteristics of organic carbon and particle composition analysis in reconstructed soil with different proportions of soft rock and sand. *PeerJ*, *7*, e
[47] Gilbert, P. U., Bergmann, K. D., Boekelheide, N., Tambutté, S., Mass, T., Marin, F., ... & Knoll, A. H. (2022). Biomineralization: Integrating mechanism and evolutionary history. *Science advances*, *8*(10), eabl9653.
[48] Seepma, S. Y., Ruiz-Hernandez, S. E., Nehrke, G., Soetaert, K., Philipse, A. P., Kuipers, B. W., & Wolthers, M. (2021). Controlling CaCO3 Particle Size with {Ca2+}:{CO32–} Ratios in Aqueous Environments. *Crystal Growth & Design*, *21*(3), 1576-1590.
[49] Gower, L. B. (2008). Biomimetic model systems for investigating the amorphous precursor pathway and its role in biomineralization. Chemical reviews, 108(11), 4551-4627.
[50] Chen, Y., Feng, Y., Deveaux, J. G., Masoud, M. A., Chandra, F. S., Chen, H., ... & Feng, L. (2019). Biomineralization forming process and bio-inspired nanomaterials for biomedical application: a review. *Minerals*, *9*(2), 68.
[51] Ambrosini, A., Rayer, M., Monier, B., & Suzanne, M. (2019). Mechanical function of the nucleus in force generation during epithelial morphogenesis. *Developmental cell*, *50*(2), 197-211.
[52] Anwar, J., Khan, S., & Lindfors, L. (2015). Secondary crystal nucleation: nuclei breeding factory uncovered. *Angewandte Chemie International Edition*, *54*(49), 14681-14684.
[53] Yousuf, M., & Frawley, P. J. (2018). Experimental evaluation of fluid shear stress impact on secondary nucleation in a solution crystallization of paracetamol. Crystal Growth & Design, 18(11), 6843-6852.

[54] Pelling, A.E., Sehati, S., Gralla, EB., Valentine, J.S., Gimzewski, J.K. (2004). Local nanomechanical motion of the cell wall of Saccharomyces cerevisiae. Science. 305, 1147–50.
[55] Charras, G. T., & Horton, M. A. (2002). Single cell mechanotransduction and its modulation analyzed by atomic force microscope indentation. *Biophysical journal*, *82*(6), 2970-2981.
[56] Zeman, F., & Lackner, K. (2008). The reduced emission oxygen Kiln. *Lenfest Center for Sustainable Energy, Earth Institute at Colombia University, New York, NY*.
[57] Miller, S. A., & Moore, F. C. (2020). Climate and health damages from global concrete production. *Nature Climate Change*, *10*(5), 439-443.
[58] Monteiro, P. J., Miller, S. A., & Horvath, A. (2017). Towards sustainable concrete. *Nature materials*, *16*(7), 698-699.
[59] Allen, R. T. L., & Edwards, S. C. (1992). Repairs to cracked concrete. In *The Repair of Concrete Structures* (pp. 56-66). CRC Press.
[60] Grantham, M. G. (Ed.). (2011). *Concrete repair: A practical guide*. CRC Press.
[61] Rahbar, N., Scarlata, S. F., & Rosewitz, J. A. (2020). *U.S. Patent No. 10,647,617*. Washington, DC: U.S. Patent and Trademark Office.
[62] Carter, M. J. (1972). CARBONIC ANHYDRASE: ISOENZYMES. PROPERTIES. DISTRIBUTION. AND FUNCTIONAL SIGNIFICANCE. *Biological Reviews*, *47*(4), 465-513.
[63] Li, W., Liu, L., Chen, W., Yu, L., Li, W., & Yu, H. (2010). Calcium carbonate precipitation and crystal morphology induced by microbial carbonic anhydrase and other biological factors. *Process Biochemistry*, *45*(6), 1017-1021.
[64] Yong, J. K., Stevens, G. W., Caruso, F., & Kentish, S. E. (2015). The use of carbonic anhydrase to accelerate carbon dioxide capture processes. Journal of Chemical Technology & Biotechnology, 90(1), 3-10.
[65] Larachi, F. (2010). Kinetic model for the reversible hydration of carbon dioxide catalyzed by human carbonic anhydrase II. Industrial & engineering chemistry research, 49(19), 9095-9104.
[66] Fu, Y., Jiang, Y. B., Dunphy, D., Xiong, H., Coker, E., Chou, S. S., ... & Brinker, C. J. (2018). Ultra-thin enzymatic liquid membrane for CO2 separation and capture. *Nature communications*, *9*(1), 990.
[67] Tarko, L., & Supuran, C. T. (2013). QSAR studies of sulfamate and sulfamide inhibitors targeting human carbonic anhydrase isozymes I, II, IX and XII. *Bioorganic & medicinal chemistry*, *21*(6), 1404-1409.
[68] ASTM, C. (2002). Standard test method for compressive strength of hydraulic cement mortars (Using 2-in. or [50-mm] cube specimens). *American Society for Testing and Material*.
[69] ASTM C1202-19. Electrical Indication of Concrete's Ability to Resist Chloride Ion Penetration.
[70] Yoon, S., Oh, S. G., Ha, J., & Monteiro, P. M. (2012). The effects of surface treatments on rapid chloride permeability tests. *Materials Chemistry and Physics*, *135*(2-3), 699-708.
[71] A. International (2017) C496/C496M-17 Standard Test Method for Splitting Tensile Strength of Cylindrical Concrete Specimens.

[72] Jafferji, H., Sakulich, A. R., & Schiffman, J. D. (2016). Preliminary study on mitigating steel reinforcement corrosion with bioactive agent. *Cement and Concrete Composites*, *69*, 9-17.
[73] Jonkers, H. M., Thijssen, A., Muyzer, G., Copuroglu, O., & Schlangen, E. (2010). Application of bacteria as self-healing agent for the development of sustainable concrete. *Ecological engineering*, *36*(2), 230-235.
[74] ASTM C33/C33M-18 Standard Specification for Concrete Aggregates
[75] ASTM C496/C496M—17 Standard Test Method for Splitting Tensile Strength of Cylindrical Concrete Specimens
[76] Hendrik Van Oss, G. (2007). Mineral Commodity Summaries. *Prepared for the US Geological Survey*.
[77] Miller, S. A., & Moore, F. C. (2020). Climate and health damages from global concrete production. *Nature Climate Change*, *10*(5), 439-443.
[78] Tittelboom, K.V., Belie, N.D., Muynck, W.D., and Verstraete, W. (2010). Use of bacteria to repair cracks in concrete. Cement Concr. Res. 1, 40.
[79] Qian, C., Chen, H., Ren, L., and Luo, M. (2015). Self-healing of early age cracks in cement- based materials by mineralization of carbonic anhydrase microorganism. Front. Microbiol. 6, 1225.
[80] Rosewitz, J.A., Wang, S., Scarlata, S.F., and Rahbar, N. (2021). An enzymatic self-healing cementitious material. Appl. Mat. Today 23, 101035.
[81] Carter, M.J. (1972). Carbonic anhydrase: isoenzymes, properties, distribution, and functional significance. Biol. Rev. 47, 465.
[82] Power, I.M., Harrison, A.L., and Dipple, G.M. (2018). Accelerating mineral carbonation using carbonic anhydrase. Environ. Sci. Technol. 5, 50.
[83] Rahbar, N., Scarlata, S.F., and Rosewitz, J.A. (2018). Method for enzymatic repair of cementitious surfaces (U.S.P.A. Publication).
[84] De Belie, N., Gruyaert, E., Al-Tabbaa, A., Antonaci, P., Baera, C., Bajare, D., Darquennes, A., Davies, R., Ferrara, L., Jefferson, T., et al. (2018). A review of self-healing concrete for damage management of structures. Adv. Mater. Interfaces 5, 1800074.
[85] Heveran, C.M., Williams, S.L., Qiu, J., Artier, J., Hubler, M.H., Cook, S.M., Cameron, J.C., and Srubar, W.V. (2020). Biomineralization and successive regeneration of engineered living building materials. Matter 2, 481.
[86] Moon, D.H., Eu, J., Lee, W., Kim, Y.E., Park, K.T., Ko, Y.N., Jeong, S.K., and Youn, M.H. (2020). Comparison of reactions with different calcium sources for CaCO3 production using carbonic anhydrase. Greenh. Gas Sci. Technol. 10, 898.
[87] Tegethoff, F.W., Rohleder, J., Kroker, E. (2001). Calcium carbonate: from the Cretaceous period into the 21st century, Springer Science & Business Media.
[88] Porter, D.A., Easterling, K.E. (2009) Phase transformations in metals and alloys (revised reprint). CRC Press.
[89] Balluffi, R.W., Allen, S., Carter, W.C. (2005) Kinetics of materials, John Wiley & Sons.
[90] Xin, A., Su, Y., Feng, S., Yan, M., Yu, K., Feng, Z., Lee, K.H., Sun, L., Wang, Q. (2021). Growing Living Composites with Ordered Microstructures and Exceptional Mechanical Properties. Adv. Mater 33, 2006946.
[91] N. Yao and A. Epstein, "Surface nanofabrication using focused ion beam," Microscopy: Science, Technology, Applications and Education, pp. 2190–2199, 2010.

[92] Hu, L. U. O., Ran, J. I. N. G., Cui, Y. M., Wang, H. L., & Wang, R. M. (2010). Improvement of fabrication precision of focused ion beam by introducing simultaneous electron beam. Progress in Natural Science: Materials International, 20, 111-115.
[93] Rogers, D.M., Jiao, D., Pratt, L.R., and Rempe, S.B. (2012). Structural models and molecular thermodynamics of hydration of ions and small molecules. Annu. Rep. Comput. Chem. 8, 71–127.
[94] Hammes, F., Boon, N., Villiers, J., Verstraete, W., and Siciliano, S.D. (2003). Strain-specific ureolytic microbial calcium carbonate precipitation. Appl. Environ. Microbiol. 69, 4901.
[95] Gebauer, D., Volkel, A., and Colfen, H. (2008). Stable prenucleation calcium carbonate clusters. Science 322, 1819.
[96] Khalifah, R.G. (1971). The carbon dioxide hydration activity of carbonic anhydrase. I. Stop-flow kinetic studies on the native human isoenzymes B and C. J. Biol. Chem. 246, 2561– 2573.
[97] Steiner, H., Jonsson, B.H., and Lindskog, S. (1975). The catalytic mechanism of carbonic anhydrase: hydrogen isotope effects on the kinetic parameters of the human C isoenzyme. Eur. J. Biothem. 59, 253–259.
[98] Wilson, M.B., and Vorderbruggen, M.A. (2017). Compositions and methods for cementing a wellbore using microbes or enzymes (Baker Hughes Invorporated).
[99] Hess, K.M., and Srubar, W.V. (2015). Mechanical characterization of gelatin-flax natural-fiber composites for construction. J. Renew. Mater. 3, 175.
[100] Armbruster, T., Danisi, R.M. (2016). Highlights in mineralogical crystallography.
[101] Porter, D.A., and Easterling, K.E. (2009). Phase transformations in metals and alloys (revised reprint) (CRC Press), p. 87.
[102] Xin, A., Su, Y., Feng, S., Yan, M., Yu, K., Feng, Z., Lee, K.H., Sun, L., and Wang, Q. (2021). Growing living composites with ordered microstructures and exceptional mechanical properties. Adv. Mater. 33, 2006946.
[103] Korchef, A., and Touaibi, M. (2020). Effect of pH and temperature on calcium carbonate precipitation by CO2 removal from iron-rich water. Water. Envir. J. 34, 331–341.
[104] ASTM C109/C109M-16a Standard Test Method For Compressive Strength Of Hydraulic Cement Mortars
[105] ASTM E1820-18 Standard Test Method for Measurement of Fracture Toughness
[106] Farris, S., Song, J., and Huang, Q. (2010). Alternative reaction mechanism for the cross-linking of gelatin with glutaraldehyde. J. Agric. Food Chem. 58, 998.
[107] Yang, G., Xiao, Z., Long, H., Ma, K., Zhang, J., Ren, X., and Zhang, J. (2018). Assessment of the characteristics and biocompatibility of gelatin sponge scaffolds prepared by various crosslinking methods. Sci. Rep. 25, 1616.
[108] Nadeem, D., Kiamehr, M., Yang, M.X., and Su, B. (2013). Fabrication and in vitro evaluation of a sponge-like bioactive-glass/gelatin composite scaffold for bone tissue engineering. Mater. Sci. Eng. C Mater. Biol. Appl. 33, 2669.
[109] Yung, C.W., Wu, L.Q., Tullman, J.A., Payne, G.F., Bentley, W.E., and Barbari, T.A. (2007). Transglutaminase crosslinked gelatin as a tissue engineering scaffold. J. Biomed. Mater. Res. A 83, 1039.
[110] Bigi, A., Cojazzi, G., Panzavolta, S., Rubini, K., and Roveri, N. (2001). Mechanical and thermal properties of gelatin films at different degrees of glutaraldehyde crosslinking. Biomaterials 8, 763.

[111] Olde Damink, L. H. H., Dijkstra, P. J., Van Luyn, M. J. A., Van Wachem, P. B., Nieuwenhuis, P., & Feijen, J. (1995). Glutaraldehyde as a crosslinking agent for collagen-based biomaterials. *Journal of materials science: materials in medicine*, *6*, 460-472.
[112] Dorr, D.N., Frazier, S.D., Hess, K.M., Traeger, L.S., and Srubar, W.V., III (2015). Bond Strength of biodegradable gelatin-based wood adhesives. J. Renew. Mater. 3, 195.
[113] Zhang, X., Do, M.D., Casey, P., Sulistio, A., Qiao, G.G., Lundin, L., Lillford, P., and Kosaraju, S. (2010). Chemical modification of gelatin by a natural phenolic cross-linker, tannic acid. J. Agric. Food Chem. 11, 58.
[114] Manji, R.A., Zhu, L.F., Nijjar, N.K., Rayner, D.C., Korbutt, G.S., Churchill, T.A., Rajotte, R.V., Koshal, A., and Ross, D.B. (2006). Bioactive polymeric materials and electrical stimulation strategies for musculoskeletal tissue repair and regeneration. Circulation 114, 318.
[115] Grabenwoger, M., Sider, J., Fitzal, F., Zelenka, C., Windberger, U., Grimm, M., Moritz, A., Bock, P., and olner, E.W. (1996). Impact of glutaraldehyde on calcification of pericardial bioprosthetic heart valve material. Ann. Thorac. Surg. 62, 772.
[116] Ores, J.D.C., Sala, L., Cerveira, G.P., Kalil, S.J. (2012). Purification of carbonic anhydrase from bovine erythrocytes and its application in the enzymic capture of carbon dioxide. Chemosphere. 2. 88
[117] Huijgen, W.J.J., Comans, R.N.J. (2003). *Carbon dioxide sequestration by mineral carbonation: Literature Review*. Report ECN C, 03, 016
[118] Kumar, D., Chandra, M.V., Elavarasan, K., Shamasundar, B.A. (2017). *Structural properties of gelatin extracted from croaker fish (Johnius sp) skin waste*. Inter J of Food Pro. 20, 3
[119] Hwang, I.H., Razzak, M.A., Ryu, B.R., Lee, D.W., Lee, J.H., Kumari, M. (2019) Method of mass-producing carbonic anhydrase in plant, United States Patent Application 20200354726.
[120] D. Maugis, J. Colloid Interface Sci. 150, 243 1992.
[121] Lefevre, G., & Jolivet, A. (2009, June). Calculation of Hamaker constants applied to the deposition of metallic oxide particles at high temperature. In Proceedings of international conference on heat exchanger fouling and cleaning (Vol. 8, pp. 120-24).
[122] Stashans, A., Chamba, G., & Pinto, H. (2008). Electronic structure, chemical bonding, and geometry of pure and Sr-doped CaCO3. Journal of computational chemistry, 29(3), 343-349.
[123] Miller, S. A., & Moore, F. C. (2020). Climate and health damages from global concrete production. *Nature Climate Change*, *10*(5), 439-443.
[124] Ellis, L. D., Badel, A. F., Chiang, M. L., Park, R. J. Y., & Chiang, Y. M. (2020). Toward electrochemical synthesis of cement—An electrolyzer-based process for decarbonating CaCO3 while producing useful gas streams. *Proceedings of the National Academy of Sciences*, *117*(23), 12584-12591.
[125] Hoenig, V., Hoppe, H., & Emberger, B. (2007). Carbon capture technology-options and potentials for the cement industry. *PCA R&D Serial*, *3022*, 98.
[126] Deja, J., Uliasz-Bochenczyk, A., & Mokrzycki, E. (2010). CO2 emissions from Polish cement industry. *International Journal of Greenhouse Gas Control*, *4*(4), 583-588.
[127] Wang, S., Scarlata, S. F., & Rahbar, N. (2022). A self-healing enzymatic construction material. *Matter*, *5*(3), 957-974.

[128] Rilem, L. C. (1978). Functional classification of lightweight concrete. *Mater. Struct*, *11*, 281-283.
[129] Li, Y., Wen, K., Li, L., Huang, W., Bu, C., & Amini, F. (2020). Experimental investigation on compression resistance of bio-bricks. *Construction and Building Materials*, *265*, 120751.
[130] Cheng, L., Kobayashi, T., & Shahin, M. A. (2020). Microbially induced calcite precipitation for production of "bio-bricks" treated at partial saturation condition. *Construction and Building Materials*, *231*, 117095.
[131] Haque, M. N., Al-Khaiat, H., & Kayali, O. (2004). Strength and durability of lightweight concrete. *Cement and Concrete Composites*, *26*(4), 307-314.
[132] Al-Jabri, K. S., Hago, A. W., Al-Nuaimi, A. S., & Al-Saidy, A. H. (2005). Concrete blocks for thermal insulation in hot climate. *Cement and Concrete Research*, *35*(8), 1472-1479.
[133] Li, Y., Wang, D., Ping, X., Zhang, Y., Zhang, T., Wang, L., ... & Ma, X. (2022). Local hyperthermia therapy induces browning of white fat and treats obesity. *Cell*, *185*(6), 949-966.
[134] O'Neal, D. P., Hirsch, L. R., Halas, N. J., Payne, J. D., & West, J. L. (2004). Photo-thermal tumor ablation in mice using near infrared-absorbing nanoparticles. *Cancer letters*, *209*(2), 171-176.
[135] Varon, L. A. B., Orlande, H. R. B., & Eliçabe, G. E. (2016). Combined parameter and state estimation in the radio frequency hyperthermia treatment of cancer. *Numerical Heat Transfer, Part A: Applications*, *70*(6), 581-594.
[136] Gas, P., & Miaskowski, A. (2015, September). Specifying the ferrofluid parameters important from the viewpoint of Magnetic Fluid Hyperthermia. In *2015 Selected Problems of Electrical Engineering and Electronics (WZEE)* (pp. 1-6). IEEE.
[137] MacLeod, A. J., Collins, F. G., & Duan, W. (2021). Effects of carbon nanotubes on the early-age hydration kinetics of Portland cement using isothermal calorimetry. *Cement and Concrete Composites*, *119*, 103994.
[138] Panea, I,. Hansenb, W. (2004). Investigation of blended cement hydration by isothermal calorimetry and thermal analysis Author links open overlay panel. Cem. Con. Res, 35, 1155.
[139] Temuujin, J,. Minjigmaa, A,. Rickard, W. (2009). Preparation of metakaolin based geopolymer coatings on metal substrates as thermal barriers. Appl Clay Sci. 46, 265–270.
[140] Toporski, J,. Dieing, T,. Hollricher, O. Confocal Raman Microscopy; Springer Series in Surface Sciences; Springer International Publishing AG: 2018.
[141] Kothandaraman, C. P. (2006). *Fundamentals of heat and mass transfer*. New Age International.
[142] Ramirez, S., Chan, K., Hernandez, R., Recinos, E., Hernandez, E., Salgado, R., ... & Balandin, A. A. (2017). Thermal and magnetic properties of nanostructured densified ferrimagnetic composites with graphene-graphite fillers. *Materials & Design*, *118*, 75-80.
[143] Diep, P., Pannem, S., Sweer, J., Lo, J., Snyder, M., Stueber, G., ... & Roblyer, D. (2015). Three-dimensional printed optical phantoms with customized absorption and scattering properties. *Biomedical optics express*, *6*(11), 4212.
[144] P. Kosky, R. Balmer, W. Keat, G. Wise. Exploring Engineering Book.
[145] VAN WIJK, W. R. (1964). Physics of plant environment. *Soil Science*, *98*(1), 69.

[146] Kundakcioglu, E., Lazoglu, I., & Rawal, S. (2016). Transient thermal modeling of laser-based additive manufacturing for 3D freeform structures. *The International Journal of Advanced Manufacturing Technology*, *85*, 493-501.
[147] Caiazzo, F., & Alfieri, V. (2018). Simulation of laser heating of aluminum and model validation via two-color pyrometer and shape assessment. *Materials*, *11*(9), 1506.
[148] Wang, S., Scarlata, S.F., and Rahbar, N. (2022). A self-healing enzymatic construction material. Matter 5, 957–974. https://doi.org/10.1016/j. matt.2021.12.020.
[149] Hammond, G., Jones, C., Lowrie, E. F., & Tse, P. (2011). Embodied carbon. *The inventory of carbon and energy (ICE). Version (2.0)*.
[150] Ashby, M. F., & CEBON, D. (1993). Materials selection in mechanical design. *Le Journal de Physique IV*, *3*(C7), C7-1.
[151] da Costa Ores, J., Sala, L., Cerveira, G. P., & Kalil, S. J. (2012). Purification of carbonic anhydrase from bovine erythrocytes and its application in the enzymic capture of carbon dioxide. *Chemosphere*, *88*(2), 255-259.
[152] Huijgen, W. J. J., & Comans, R. N. J. (2003). Carbon dioxide sequestration by mineral carbonation. Literature Review.
[153] Kumar, D. P., Chandra, M. V., Elavarasan, K., & Shamasundar, B. A. (2017). Structural properties of gelatin extracted from croaker fish (Johnius sp) skin waste. *International Journal of Food Properties*, *20*(sup3), S2612-S2625.
[154] Popescu, A., & Woods, L. M. (2012). Valleytronics, carrier filtering and thermoelectricity in bismuth: Magnetic field polarization effects. *Advanced Functional Materials*, *22*(18), 3945-3949.
[155] Zheng, Y., Zhang, W., Li, Y., Chen, J., Yu, B., Wang, J., ... & Zhang, J. (2017). Energy related CO2 conversion and utilization: advanced materials/nanomaterials, reaction mechanisms and technologies. *Nano Energy*, *40*, 512-539.
[156] Baltrusaitis, J., Schuttlefield, J., Zeitler, E., & Grassian, V. H. (2011). Carbon dioxide adsorption on oxide nanoparticle surfaces. *Chemical Engineering Journal*, *170*(2-3), 471-481.